

**Analysis of Closed-Orbit Deviations for a first direct Deuteron  
Electric Dipole Moment Measurement at the Cooler  
Synchrotron COSY**

–

**Analyse von Abweichungen der geschlossenen Teilchenbahn für  
eine erste direkte Messung des Elektrischen Dipolmoments von  
Deuteronen im Kühlersynchrotron COSY**

**Master Thesis**

OF

**Vera Schmidt**

from Siegen

submitted to

Faculty for Mathematics, Computer Science and Natural Science

of the RWTH Aachen University

on 29 September 2016

carried out at the

Physics Institute III B

under

Prof. Dr. Andreas Lehrach

## Abstract

This master thesis investigates closed orbit influencing effects focusing on transverse orbit deviations. Using a model of the Cooler Synchrotron COSY at the Forschungszentrum Jülich implemented in the *Methodical Accelerator Design* program, several magnet misalignments are simulated and analyzed. A distinction is made between magnet displacements along the axes and rotations around them. Results are always analyzed for the uncorrected as well as for the orbit after the application of an orbit correction. Furthermore, the effect of displaced beam position monitors is simulated and a constraint resolution of their readout is considered. Besides magnet misalignments also field variations resulting from residual power supply oscillations are quantified for all types of magnets.

The simulation results are compared to the measured closed orbit at COSY to estimate the dominant effects and to quantify the misalignments of the magnets. Results of a survey of COSY, performed in April 2016, are implemented in the simulation model to compare the output with the measured orbit at COSY.

Considering an upgrade of the current orbit correction setup of COSY, a heuristical algorithm is used to estimate the optimal placement of additional beam position monitors and corrector dipoles and to estimate the resulting closed orbit *RMS* reduction.

In dieser Masterarbeit werden Effekte untersucht, die die transversalen Abweichungen der geschlossenen Teilchenbahn im Speicherring und Kühlersynchrotron COSY am Forschungszentrum Jülich beeinflussen. Als zugrunde liegende Software wird das Programm *MAD-X* benutzt. In einem in *MAD-X* implementierten Modell von COSY werden verschiedene Ausrichtungsfehler der Magnete sowie Positionierungs- und Auflösungsfehler der Strahlblagemonitore simuliert und analysiert. Des Weiteren werden Magnetfeldoszillationen für alle Magnettypen untersucht, die durch beschränkte Netzgerätstabilitäten verursacht werden. In den Simulationen wird jeweils die geschlossene Lösung durch die Magnetstruktur berechnet. Hierbei wird zwischen dem Orbit vor und nach einer Orbitkorrektur unterschieden.

Die Simulationsergebnisse werden mit Messungen an COSY verglichen, um die dominanten Einflüsse auf die geschlossene Teilchenbahn zu identifizieren und eine Abschätzung für die Magnetfehlstellungen an COSY zu erlangen. Ergebnisse einer genauen Vermessung der COSY Magnete werden außerdem in das Simulationsmodell implementiert, um die resultierenden Simulationsergebnisse mit Messwerten zu vergleichen.

Im Hinblick auf ein mögliches Upgrade des Orbitkorrektursystems an COSY wird mit Hilfe eines heuristischen Ansatzes eine erste Abschätzung für die Positionierung neuer Strahlblagemonitore und Korrekturdipole erzielt.

# Contents

<b>1</b>	<b>Introduction</b>	<b>1</b>
<b>2</b>	<b>Scientific Motivation</b>	<b>2</b>
2.1	Matter-antimatter asymmetry . . . . .	2
2.2	Precursor experiment at COSY . . . . .	3
<b>3</b>	<b>Cooler Synchrotron COSY</b>	<b>4</b>
<b>4</b>	<b>Beam Dynamics in Periodic Closed Lattices</b>	<b>8</b>
4.1	Charged particles in a magnetic field . . . . .	8
4.1.1	Multipole expansion . . . . .	8
4.1.2	Fundamental elements . . . . .	9
4.2	Coordinate system . . . . .	18
4.3	Equation of motion . . . . .	19
4.4	Transverse motion . . . . .	20
4.4.1	Dispersion . . . . .	22
4.4.2	Chromaticity . . . . .	24
4.5	Orbit correction . . . . .	25
4.5.1	Orbit response matrix . . . . .	26
<b>5</b>	<b>Closed Orbit Influencing Effects</b>	<b>28</b>
5.1	Magnet misalignments . . . . .	28
5.1.1	Quadrupole displacement . . . . .	28
5.1.2	Quadrupole rotation . . . . .	34
5.1.3	Dipole displacement . . . . .	37
5.1.4	Dipole rotation . . . . .	40
5.2	BPM displacement . . . . .	43
5.3	BPM resolution . . . . .	48
5.3.1	Constant resolution of 0.1 mm . . . . .	48
5.3.2	Running BPM resolution . . . . .	50
5.4	Field instabilities . . . . .	54
5.4.1	Dipole field instabilities . . . . .	54
5.4.2	Quadrupole field instabilities . . . . .	57
5.5	Residual power supply oscillations . . . . .	57
5.6	Comparison of simulation and measurement . . . . .	62
5.7	Survey at COSY . . . . .	64
<b>6</b>	<b>Upgrade of the Orbit Correction Setup at COSY</b>	<b>73</b>
<b>7</b>	<b>Conclusion and Outlook</b>	<b>76</b>
<b>A</b>	<b>Upgrade of the orbit correction system</b>	<b>i</b>

List of Figures	iii
List of Tables	v
References	vi
Acknowledgments	viii

# 1 Introduction

The path of a beam through the magnetic structure of a circular accelerator needs to be well known and controlled for high precision experiments. An important aspect of the beam trajectory is its transverse deviation from a specified reference orbit. The so called *closed orbit* [1] in an accelerator ring is a measure of the beam quality as it describes the one-turn periodic closed particle trajectory through the magnetic structure. All beam particles oscillate around this trajectory. In order to understand measured closed orbits at an accelerator, beam distorting effects must be investigated.

At the Cooler Synchrotron and storage ring COSY at the Forschungszentrum Jülich the design of an experiment for a first, direct measurement of the deuteron Electric Dipole Moment (EDM) is implemented. Besides upgrades for the current accelerator setup also orbit studies have to be performed to understand the current closed orbit measurements which presently reaches Root Mean Square (RMS) values of the order of 3 mm. For the future experiment a RMS value of at most  $100\ \mu\text{m}$  is needed to enable a measurement of an EDM of  $5 \cdot 10^{-20}\ \text{e cm}$  [2].

In this master thesis, various imperfection effects influencing the COSY closed orbit are investigated. For simulations the *Methodical Accelerator Design* (MAD) program [3] is used with an implemented model of COSY including dipoles, quadrupoles and higher multipoles. The goal is to determine the most influencing effects on the orbit which then can be reduced in the future to optimize the setup for high precision experiments. Simulations include different misalignments, distinguishing shifts and rotations of the magnets and field oscillations which can be the result of power supply stability limits. Also the resolution of beam position monitors are considered. Besides random misalignments, also the results of a current survey of COSY are used in the simulation model to compare the results with the real measured orbit and to benchmark the simulation model. At the end, a first heuristical ansatz for an improved orbit correction setup at COSY is simulated in order to estimate the smallest achievable closed orbit RMS after an orbit correction.

## 2 Scientific Motivation

### 2.1 Matter-antimatter asymmetry

One of the main challenges in modern-day particle physics is to find an explanation for the observed matter-antimatter asymmetry in the universe [4]. The baryon-to-photon density ratio is a measure of this asymmetry and can be derived from the angular distribution of the cosmic microwave background. Performed experiments result in

$$\eta_{BA} = \frac{n_B - n_{\bar{B}}}{n_\gamma} = (6.047 \pm 0.074) \cdot 10^{-10}, \quad (2.1)$$

where  $\eta_{BA}$  describes the baryon asymmetry and  $n_B$ ,  $n_{\bar{B}}$  and  $n_\gamma$  denote the baryon, anti-baryon and photon densities respectively [5]. The Standard Model of Particle Physics (SM) predictions are about eight orders of magnitude smaller and therefore cannot explain the observations. A possible explanation of the matter-antimatter asymmetry comes from models that include processes resulting in an asymmetric annihilation of matter and antimatter. These models must fulfill the Sakharov conditions [6]:

- **Baryon number violation:** There must be processes of the form  $X \rightarrow Y+B$ , where  $X$  and  $Y$  have a baryon number of zero and  $B$  is a baryon.
- **Thermal non-equilibrium interactions:** Each process is as likely to happen as the inverse process in equilibrium. Therefore there would be no excess of produced baryons in equilibrium.
- **$\mathcal{C}$  and  $\mathcal{CP}$  violation:** The same rate of a reaction and its corresponding conjugate process would compensate the asymmetric production of baryons and anti-baryons.  $\mathcal{C}$  and  $\mathcal{CP}$  violating processes of weak interactions in the SM are too small to explain the observed asymmetry.

The Electric Dipole Moment (EDM) of single particles is a possible candidate for a new source of  $\mathcal{CP}$  violating processes. The EDM violates parity  $\mathcal{P}$  and time reversal invariance  $\mathcal{T}$ . Assuming that the  $\mathcal{CPT}$  theorem holds, a violation of  $\mathcal{T}$  is equivalent to a violation of  $\mathcal{CP}$ . The Standard Model prediction of a nucleon EDM is of the order of  $10^{-31}$  to  $10^{-33}$  e cm [7]. Measuring a different EDM value than these predictions would give evidence of physics beyond the standard model and would lead to a deeper understanding of the universe.

An EDM can be measured by its influence on the motion of the particles' spin. An electric field acting on the EDM in the rest frame tilts the spin according to [8]

$$\frac{d\vec{S}}{dt} = \vec{d} \times \vec{E}^*, \quad (2.2)$$

where  $\vec{E}^*$  denotes the electric field in the rest frame of the particle and  $\vec{d}$  describes the EDM. In order to measure EDMs of charged hadrons, the Jülich Electric Dipole moment Investigations collaboration (JEDI) designs and performs precursor experiments with polarized proton and deuteron beams at COSY.

## 2.2 Precursor experiment at COSY

Aiming at measuring the neutron EDM, many experiments were performed over the last 50 years. Starting with an upper limit of the order of  $10^{-19}$  e cm and ending up in 2006 with a limit of about  $10^{-26}$  e cm [9] some SUSY models [10] could be excluded or their parameter spaces could at least be constrained. Future experiments are planned to reach an upper limit of  $10^{-28}$  e cm.

To prove the existence of hadron EDMs with values beyond the Standard Model predictions, different particles have to be investigated. Up to now, there exists no direct measurement of a proton or a deuteron EDM. An upper limit of  $7.9 \cdot 10^{-25}$  e cm for the proton EDM was only deduced indirectly using  $^{199}\text{Hg}$  atoms [11]. Direct measurements could further improve the limit. Experiments for an electric and magnetic accelerator ring are investigated by the JEDI collaboration at Jülich which allow studies of the deuteron and proton EDM at an upgrade of the storage ring COSY. Current test experiments at COSY use deuterons with a momentum of 970 MeV/c. The intended goal is to reach an upper limit for the deuteron EDM of  $10^{-24}$  e cm using a RF-E/B spin flipper with a transverse electric field [12].

One of the challenges in performing such a high sensitivity experiment is to provide a precise beam, allowing only small deviation of the closed orbit<sup>1</sup> from the ideal path through the magnetic structure of the ring. Field instabilities and magnet misalignments influence the beam as it traverses the element and lead to deviations from this ideal path. They also influence the spin motion and lead to false EDM signals. Simulations have shown that a *RMS* of the transverse closed orbit below  $100 \mu\text{m}$  is required to measure a deuteron EDM of about  $5 \cdot 10^{-20}$  e cm. In this case, the false signal due to magnet misalignments can be distinguished from the real EDM signal. Assuming randomized Gaussian distributed quadrupole shifts, the corresponding required standard deviation is  $10 \mu\text{m}$  [2]. In the process of planing the experiment at COSY it is therefore crucial to understand various beam influencing effects and to find out the main sources for beam deviations. In the future these effects have to be compensated in order to improve the setup.

---

<sup>1</sup>see section 4 for further explanations

### 3 Cooler Synchrotron COSY

The accelerator facility at the Forschungszentrum Jülich mainly consists of an ion source, providing polarized and unpolarized  $H^-$  or  $D^-$  ions, a cyclotron named JULIC and the synchrotron and storage ring COSY. This setup is schematically displayed in Figure 3.1. In the injector cyclotron either  $H^-$  or  $D^-$  ions are accelerated up to 300 MeV/c (600 MeV/c) and are guided to the synchrotron through a 100 m long beam line. Using a stripping injection, protons (deuterons) are created and fed into COSY, where they can be accelerated further up to 3.7 GeV/c using an RF cavity. Per fill up to  $10^{10}$  polarized or up to  $10^{11}$  unpolarized particles can be injected into COSY. The polarization can be measured by the low energy polarimeter before injection or afterwards by the EDDA detector [13].

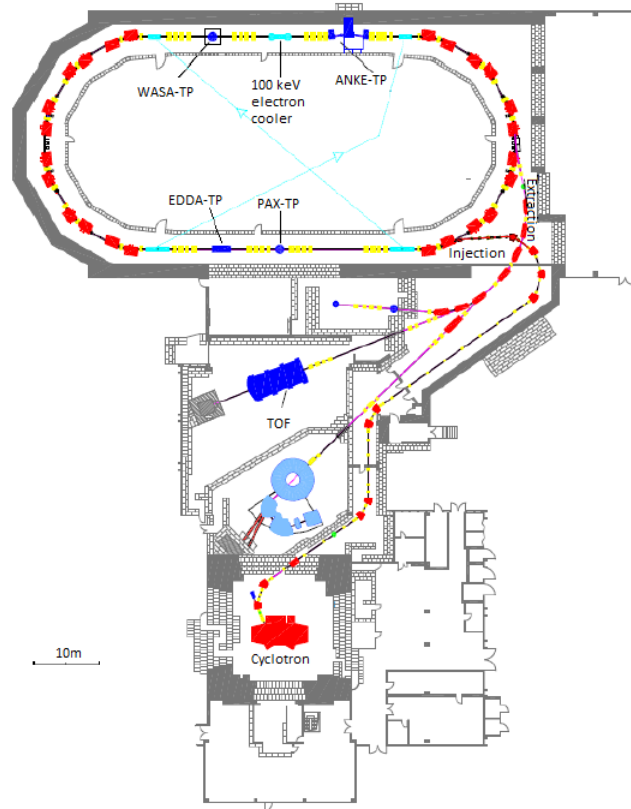


Figure 3.1: Sketch of the accelerator facility at the Forschungszentrum Jülich. At the lower end one can identify the cyclotron where  $H^-$  or  $D^-$  ions are accelerated up to 300 MeV/c (600 MeV/c). The injection beam line connects the cyclotron to the synchrotron and storage ring COSY where energies of 3.7 GeV/c can be reached. Taken from [2].

The ring owes its name to the phase space controlling which is achieved by beam cooling. On the one hand the beam can be cooled by electron cooling, which is used up to momenta of 0.6 GeV/c. Additionally a second electron cooler was installed at COSY in 2013 which enables cooling in the whole energy range of COSY [14]. On the other

hand stochastic cooling is provided for particle momenta above 1.5 GeV/c [13]. COSY has a circumference of about 184 m with two straight sections (each 39.7 m long) and two 180° arc sections (each 52 m long) [15].

Magnets up to second order are installed, i.e. dipoles, quadrupoles and sextupoles. The straight sections contain eight quadrupole families (MQT1-MQT8) each consisting of four quadrupoles. Within one family, the quadrupoles have the same dimensions and are connected to the same power supply. The quadrupoles in the straights are placed in triplets, each either in the configuration DFFD or FDDF<sup>2</sup>. In each straight section there are four of these triplets.

In order to bend the beam, 24 dipoles are distributed in the two arc sections (12 per arc). They all belong to the same family, i.e. are connected to the same power supply. For focusing purposes additional 24 quadrupoles are placed in the arc sections. They are separated into six families (MQU1-MQU6) each containing four magnets.

Another 17 sextupoles, seven in the straight sections and ten positioned in the arcs, are installed. The sextupoles in the arcs are divided into three families (MXS, MXL, MXG). Aiming at minimal dispersion they are used to correct chromaticity in the vertical and horizontal plane [16].

The positioning and the grouping into magnet families at COSY is illustrated in Figure 3.2.

Orbit corrections and measurements are performed using 22 (19) corrector magnets and 30 (29) beam position monitors in the horizontal (vertical) plane. Each corrector magnet is connected to its own power supply to ensure an independent magnet strength setting. The distribution of corrector magnets and beam position monitors at COSY is depicted in Figure 3.3.

---

<sup>2</sup>D = horizontally defocusing, F = horizontally focusing

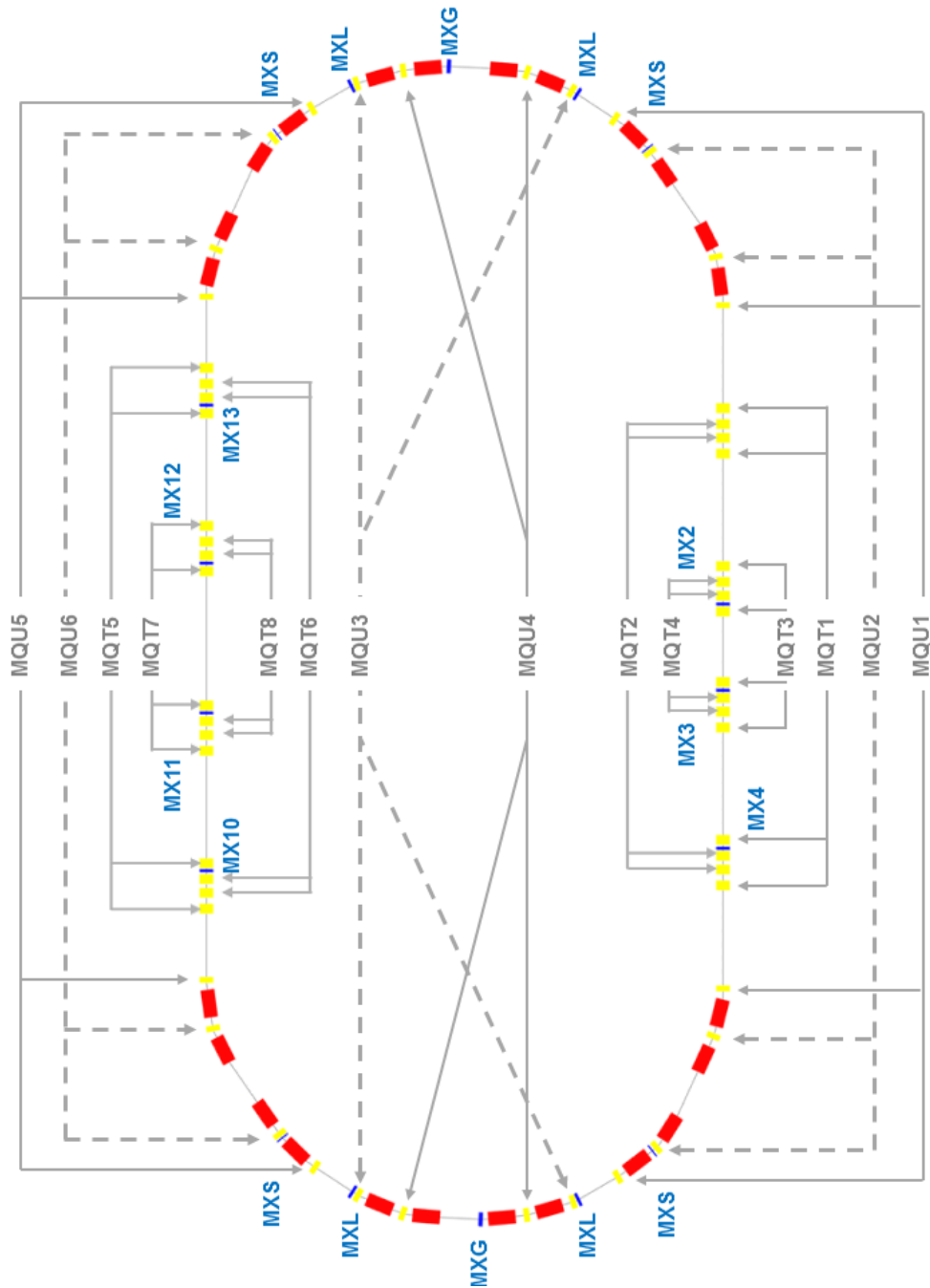


Figure 3.2: Dipoles, quadrupoles and sextupoles families at COSY. The injection takes place at the upper right corner. The dipoles are shown in red. All dipoles are connected to the same power supply. The quadrupoles, depicted in yellow, partially share a power supply and are therefore grouped together into several families, each containing four magnets. The grey arrows illustrate the composition of these quadrupole families. The sextupoles, given in blue, each have a single power supply in the straight sections. In the arcs they are mirror symmetrically grouped into magnet families with the names MXS, MXL and MXG.

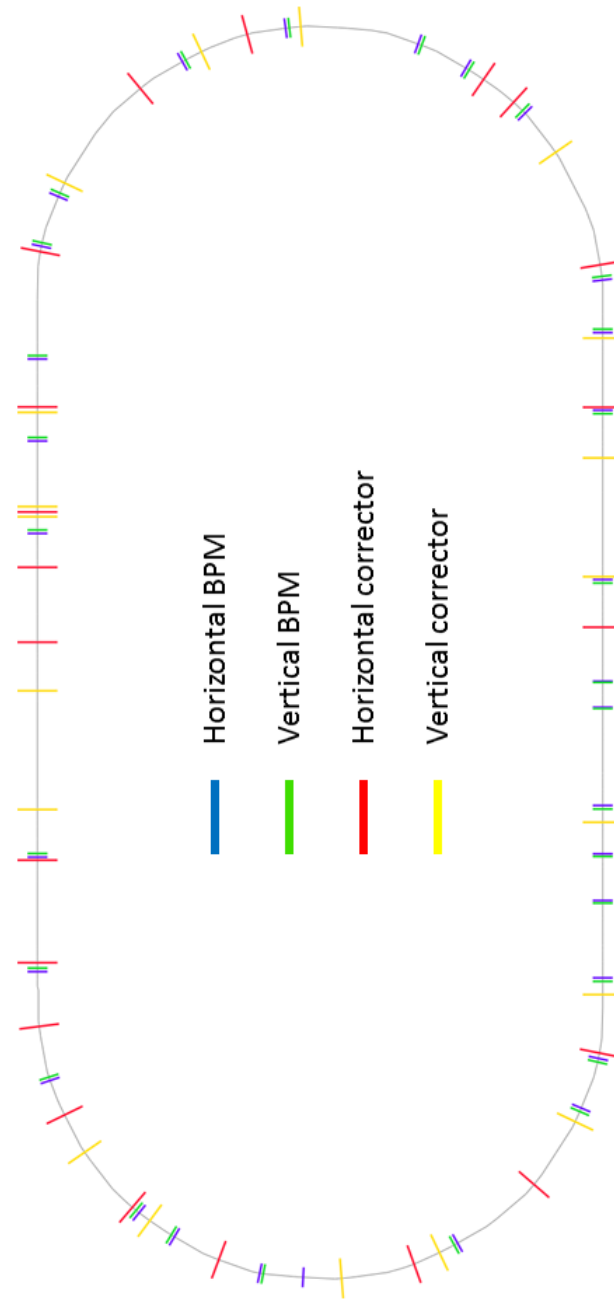


Figure 3.3: Placements of beam position monitors and corrector magnets at COSY. The injection takes place at the upper right corner. Each corrector magnet is connected to an exclusive power supply. There are 22 (19) correctors installed in total for the purpose of influencing the beam in x-(y-)direction. To measure the beam position 30 (29) monitors are used for the horizontal (vertical) direction. The magnets that can steer the beam in horizontal direction are indicated in red, the ones for the vertical direction are shown in yellow. Beam position monitors (BPMs) are marked in blue (green) if they measure the orbit position in the horizontal (vertical) plane.

## 4 Beam Dynamics in Periodic Closed Lattices

A knowledge of beam dynamics is essential when studying the orbit of a storage ring. Therefore this chapter gives a brief introduction in the dynamics of a beam in a periodic closed lattice and introduces the notation used in this thesis.

### 4.1 Charged particles in a magnetic field

Particle motion in a storage ring is governed by the Lorentz force. The particles pass the element structure many times and the natural angular distribution in an ensemble of particles will lead to a loss of the beam intensity after a finite amount of time due to particles that hit the wall of the beam pipe. Besides defining the reference orbit for particles by a specific element structure it is therefore crucial to prevent particle loss and hence retain the beam intensity. This is generally achieved by applying electromagnetic fields acting on particles via the *Lorentz force*

$$F_L = q(\vec{E} + \vec{v} \times \vec{B}), \quad (4.1)$$

where  $q$  is the charge of the particle,  $\vec{E}$  is the electric field,  $\vec{v}$  is the particles velocity and  $\vec{B}$  is the magnetic field. Considering relativistic particles with a momentum perpendicular to magnetic field, electric and magnetic fields have the same impact on the particles if  $\vec{E} = c\vec{B}$  is fulfilled. Since producing high electric fields is technically challenging it is common to almost exclusively use magnetic fields to guide the beam through the accelerator.

#### 4.1.1 Multipole expansion

In a typical pure magnetic circular accelerator with only transverse magnetic fields, transverse beam dimensions are small compared to the bending radius. Therefore one can expand the magnetic fields in the vicinity of the ideal orbit. In a Cartesian coordinate system  $(x, y, s)$  with  $s$  pointing along the particle momentum,  $x$  defining the horizontal axis and  $y$  pointing in vertical direction the expansion of the magnetic field is given by

$$B_y(x) = B_{y0} + \frac{dB_y}{dx} x + \frac{1}{2!} \frac{d^2B_y}{dx^2} x^2 + \frac{1}{3!} \frac{d^3B_y}{dx^3} x^3 + \mathcal{O}(x^4). \quad (4.2)$$

Multiplying by the charge-momentum ratio  $\frac{q}{p}$  yields [17]

$$\begin{aligned} \frac{q}{p} B_y(x) &= \frac{q}{p} B_{y0} + \frac{q}{p} \frac{dB_y}{dx} x + \frac{1}{2!} \frac{q}{p} \frac{d^2B_y}{dx^2} x^2 + \frac{1}{3!} \frac{q}{p} \frac{d^3B_y}{dx^3} x^3 + \mathcal{O}(x^4) \\ &= \underbrace{\frac{1}{\rho}}_{\text{Dipole}} + \underbrace{kx}_{\text{Quadrupole}} + \underbrace{\frac{1}{2!} mx^2}_{\text{Sextupole}} + \underbrace{\frac{1}{3!} ox^3}_{\text{Octupole}} + \mathcal{O}(x^4), \end{aligned} \quad (4.3)$$

where  $\frac{1}{\rho} (k, m, o)$  represents the magnet strength of the dipoles (quadrupole, sextupoles, octupoles). As indicated in Equation 4.3 the magnetic field can be written as the sum of multipoles each acting differently on the beam. In the case of a *linear beam optics* the underlying accelerator magnets only consist of the two lowest multipoles which imply only constant or linearly increasing forces with increasing transverse displacement from the center of the magnet. Higher order multipoles appear in the form of magnet errors and are deliberately used to correct field errors and chromaticity effects.

#### 4.1.2 Fundamental elements

Based on the findings of Section 4.1.1 the fundamental elements used for beam guidance are briefly described in this section. Assuming static magnetic fields with only transverse components one can show that the scalar potential in the area of the beam where no current flows is given by [18]

$$\Phi(x, y) = G_y(x) y - \frac{1}{6} \frac{d^2 G_y(x)}{dx^2} y^3 \quad (4.4)$$

with the given behavior of the vertical field component along the x-axis  $G_y(x)$ . The final field distribution then reads

$$\vec{B}(x, y) = \begin{pmatrix} \frac{d\Phi(x, y)}{dx} \\ \frac{d\Phi(x, y)}{dy} \\ 0 \end{pmatrix}. \quad (4.5)$$

For a given field distribution along  $x$ , the potential and the magnetic field in the  $(x, y)$ -plane can now be determined using Equations 4.4 and 4.5. In the following the field distributions for the main elements in an accelerator will be specified to define the optimal magnet shape.

##### 4.1.2.1 Dipole

Dipole magnets are used for bending a beam of charged particles. Therefore a constant field along the  $x$  direction is needed, requiring

$$G_y(x) = B_0 = \text{const.} \quad (4.6)$$

The second term in Equation 4.4 vanishes and the potential is directly given by

$$\Phi(x, y) = B_0 y, \quad (4.7)$$

with equipotential lines  $y(x)$  parallel to the  $x$  axis. Hence, a normal-conducting dipole is build of two parallel iron plates and the magnetic field is created via coils wound around the iron, as sketched in Figure 4.1.

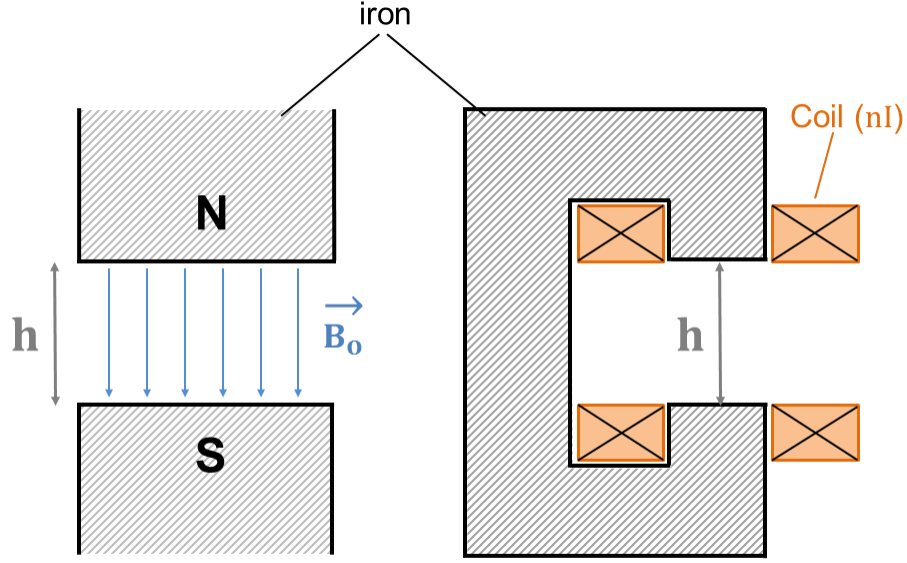


Figure 4.1: Sketch of a dipole: The left picture shows a transversal cut through the dipole. The particles move perpendicularly to the field lines. For field lines in the vertical direction the beam is bend horizontally. The illustration on the right is a zoomed out version of the left one. It shows the configuration of the coils which produce the homogeneous magnetic field in the gap. Based on [18].

Assuming a total number of  $n$  windings and a current  $I$  in the coil, the Maxwell relation

$$\oint \vec{H} ds = nI = I_{\text{total}} \quad (4.8)$$

shows the connection between the generating current and the resulting field strength. The field is furthermore assumed to be constant in the iron ( $H_{\text{iron}} = \text{const.}$ ) and between the plates ( $H_0 = \text{const.}$ ). Since  $H_{\text{iron}} = \frac{H_0}{\mu_r}$  with  $\mu_r \gg 1$ , Equation 4.8 simplifies to (according to the quantities in Figure 4.1)

$$nI = \oint \vec{H} d\vec{s} = H_{\text{iron}} l_{\text{iron}} + H_0 h \approx H_0 h, \quad (4.9)$$

where  $h$  is the distance between the magnetic north- and south-pole (see Figure 4.1) and  $l_{\text{iron}}$  is the length of the integration path inside the iron core. Using  $B_0 = \mu_0 H_0$  the field of an ideal dipole magnet can therefore be written as

$$B_0 = \mu_0 \frac{nI}{h}. \quad (4.10)$$

From the equality of the Lorentz force (Equation 4.1) and the centripetal force one can calculate the dipole strength

$$\frac{1}{\rho} = \frac{q}{p} B_0 = \frac{q \mu_0 n I}{p h}, \quad (4.11)$$

which linearly depends on the field generating current. The deflection angle  $\alpha$  in the dipole can easily be deduced geometrically and reads

$$\alpha = \frac{L}{\rho}, \quad (4.12)$$

where  $L$  is the length of the dipole.

#### 4.1.2.2 Quadrupole

In order to focus the beam quadrupole magnets are needed since their fields vanish for a non-displaced particle and increase linearly with increasing displacement  $\Delta x$  or  $\Delta y$  from the magnet center [19]. Using the field gradient  $g = \frac{\partial B}{\partial x}$ , the field distribution is therefore described by

$$G_y(x) = gx. \quad (4.13)$$

As in the case of a dipole the second term of Equation 4.4 vanishes and the resulting potential reads

$$\Phi(x, y) = gxy. \quad (4.14)$$

In this case the equipotential lines are hyperbolas. A quadrupole therefore consists of four poles of hyperbolic shape as shown in Figure 4.2. One can see from the field lines that a quadrupole with a horizontally focusing plane acts defocusing in the vertical plane and vice versa. Focusing a beam in both directions hence requires at least two quadrupoles rotated relatively to each other by  $90^\circ$ .

A relation between current and resulting field is derived analogously to Section 4.1.2.1. Using Equation 4.9 and following the integration path illustrated in Figure 4.3 yields

$$\oint \vec{H} \, d\vec{s} = \int_0^1 \vec{H}_0 \, d\vec{s} + \int_1^2 \vec{H}_{\text{iron}} \, d\vec{s} + \int_2^0 \vec{H} \, d\vec{s} = nI. \quad (4.15)$$

Since  $\mu_r \gg 1$ ,  $H_{\text{iron}}$  is comparatively small and the integral inside the iron ( $1 \rightarrow 2$ ) can be neglected. For the third part ( $2 \rightarrow 0$ ),  $\vec{H}$  is always orthogonal to  $d\vec{s}$  thus the integral is zero. The only remaining part is the path between the magnet center and the pole surface. Here the field is given by  $B_x = gy$  and  $B_y = gx$  which directly follows from the form of the potential in 4.14.

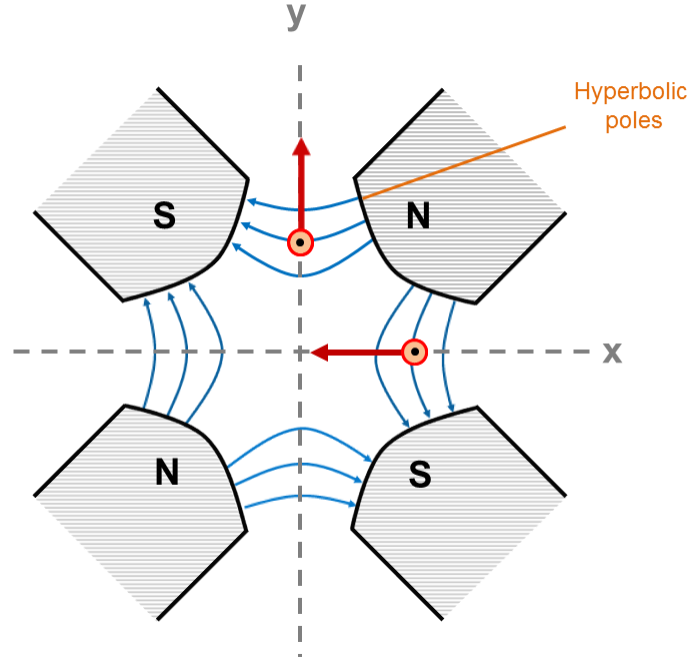


Figure 4.2: Transversal cut through a quadrupole magnet; the beam moves perpendicularly to the x-y-plane. The quadrupole acts focusing in x-direction and defocusing in y-direction for particles moving out of the plane. Based on [18].

The absolute value of the magnetic field strength along the path ( $0 \rightarrow 1$ ), where  $x = y$ , is given by

$$H = \frac{g}{\mu_0} \sqrt{x^2 + y^2} = \frac{g}{\mu_0} r, \quad (4.16)$$

with  $r = a$  being the distance from the magnet center to the pole surface. Performing the remaining integral thus yields

$$\int_0^a H \, dr = \frac{g}{\mu_0} \int_0^a r \, dr = \frac{g}{\mu_0} \frac{a^2}{2} = nI \quad (4.17)$$

and the quadrupole strength can be written as

$$k = \frac{q}{p} g = \frac{q}{p} \frac{2\mu_0 n I}{a^2}. \quad (4.18)$$

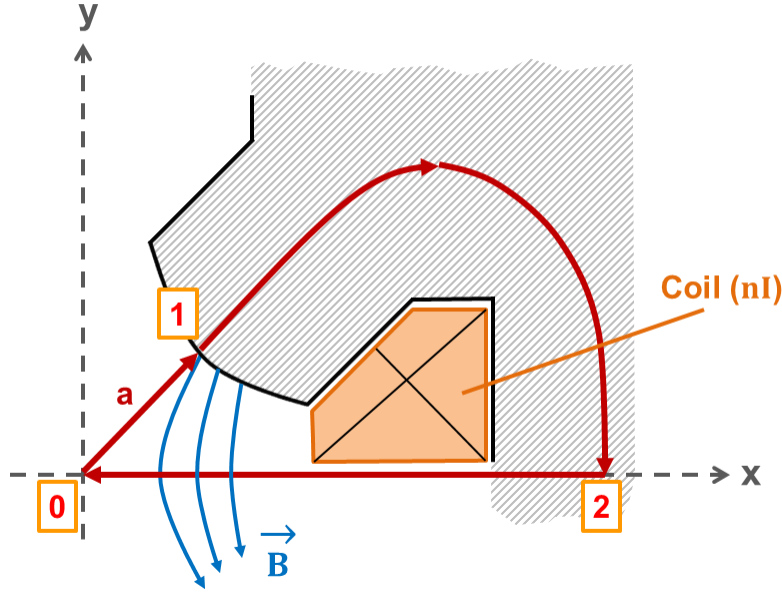


Figure 4.3: One pole of a quadrupole and the integration path which is used to determine the relation between current in the coil and the resulting magnetic field. When they cross the  $x$ -axis, the field lines are orthogonal to it. The permeability inside the iron is much larger than outside the quadrupole. Based on [18].

#### 4.1.2.3 Sextupole

The last magnet used in COSY is the sextupole magnet which is needed to compensate chromaticity, which is explained in more detail in Section 4.4.2. Sextupoles have a quadratic field distribution along the  $x$  axis which can be described by

$$G_y(x) = \frac{1}{2}g'x^2. \quad (4.19)$$

Therefore the second term of Equation 4.4 no longer vanishes but leads to a coupling of horizontal and vertical particle motion inside the sextupole. Inserting  $G_y(x)$  into Equation 4.4 yields

$$\Phi(x, y) = \frac{1}{2}g' \left[ x^2y - \frac{y^3}{3} \right]. \quad (4.20)$$

The equipotential lines again define the design of the magnet poles which leads to six poles arranged to each other with an angle of  $60^\circ$  and with alternating polarity. The poles and the equipotential lines are illustrated in Figure 4.4. Again the distance from the origin of the magnet to the pole surface is called  $a$ .

Analogously to dipoles and quadrupoles one can calculate the relation of current and

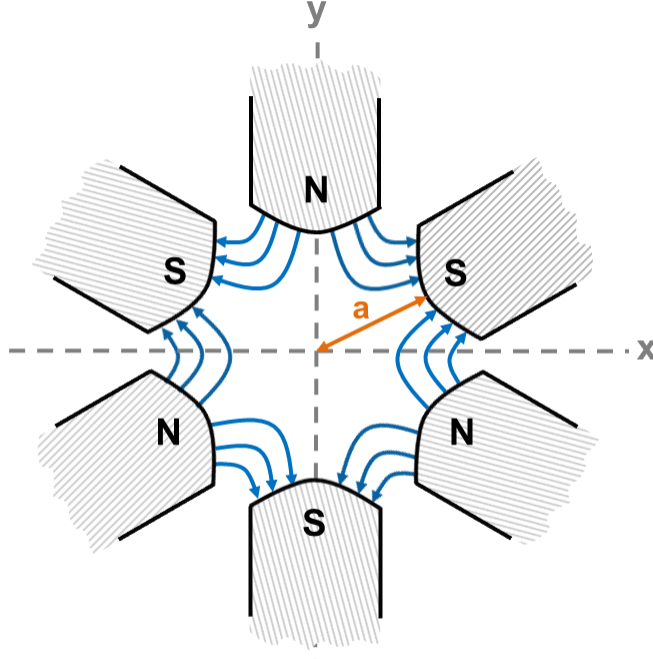


Figure 4.4: Shown is a transversal cut through a sextupole magnet and the field lines between the poles. Based on [18].

magnetic field strength. Using the same arguments as before leads to [18]

$$g' = \frac{\partial^2 B_y}{\partial x^2} = 6\mu_0 \frac{nI}{a^3} \quad (4.21)$$

and the sextupole strengths can be found to be

$$m = \frac{q}{p} g' = \frac{q}{p} 6\mu_0 \frac{nI}{a^3}. \quad (4.22)$$

#### 4.1.2.4 Beam Position Monitor

Studying the orbit in a storage ring requires devices to measure the beam position along the ring. Bunched beams are commonly investigated using electrostatic pick-ups allowing a non-destructive measurement of the beam position and the bunch length. The method is based on the effect of induced charges on an insulated metal plate due to the field generated by the beam particles. Since this electric field is time dependent in a bunched beam, the induced signal is alternating [20]. Figure 4.5 shows the effect schematically. In order to determine the center of mass of the beam position, four pick-ups are placed around the beam pipe, with two of them arranged face to face<sup>3</sup> in the horizontal or vertical plane respectively. Such a setup is called *beam position monitor* (BPM) [18].

<sup>3</sup> This configuration cannot be used when investigating electrons due to synchrotron radiation damages.

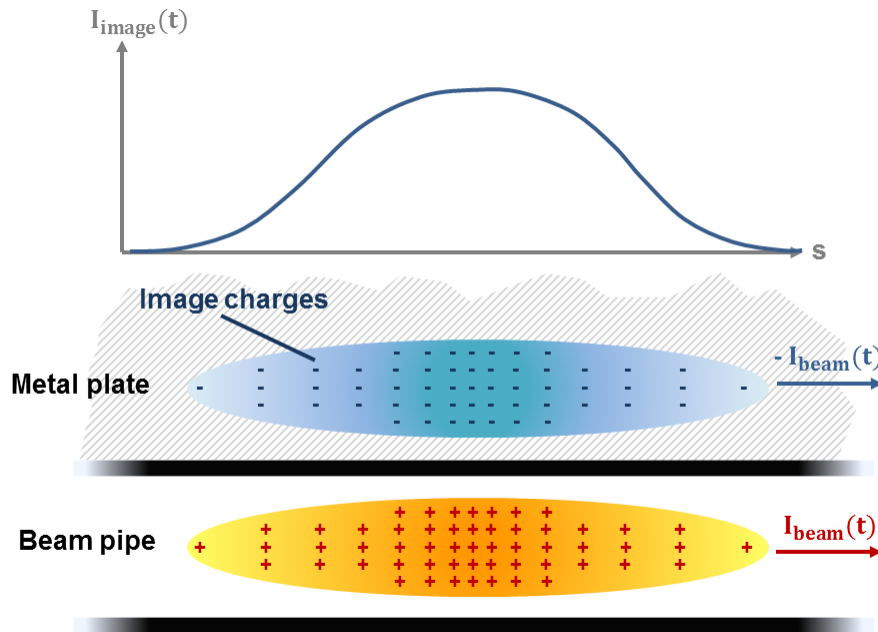


Figure 4.5: The time dependent charged particle flux in a bunched beam induces a time dependent image current in the beam pipe wall due to the changing electric field. This effect can be used to measure the beam position with pick-up plates positioned around the beam pipe. Based on [20].

With increasing particle energy the longitudinal component of the generated field decreases more and more as can be seen in Figure 4.6. For velocities with  $\beta > 0.5$  the field can be estimated to be completely transverse which implies the same time behavior of the induced current and the passing beam. A turn-by-turn readout enables measurements of turn-based quantities like the betatron tune (see Section 4.4) or the chromaticity (see Section 4.4.2). The closed orbit is obtained by measuring on a much longer time scale than the revolution time in the storage ring. Doing so, the betatron oscillations (see Section 4.4) average out and the resulting data represents the averaged position of the bunch. Besides transverse observations also the bunch length as a function of time can be recorded [20].

Due to its large signal strength and linear measurement behavior, linear-cut, also called shoe-box, BPMs are often used in storage rings. Figure 4.7 shows the geometry of such a rectangular device where the triangle electrodes in both directions (vertical and horizontal) can be identified. Their signal strengths is related to the fraction of the beam that is covered by the BPM electrode. Hence for a given displacement of the beam the signal is proportional to the length of the beam projection on the surface of the electrode.

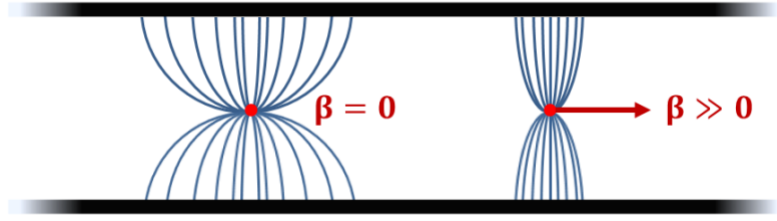


Figure 4.6: The field line distribution of a charged particle moving in the beam pipe gets more and more transversal with increasing velocity. For a relativistic particle the field can be assumed to be completely transverse. As a consequence the time behavior of the beam and the induced wall current are equal. Based on [20].

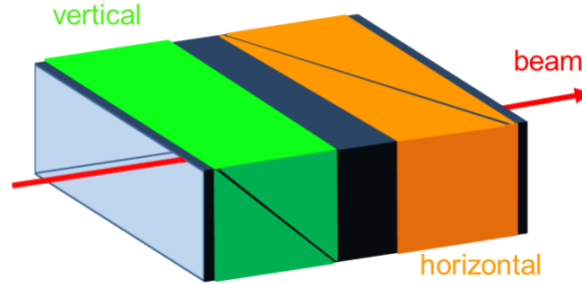


Figure 4.7: Shown is the geometry of a rectangular BPM, called shoe-box BPM. The design of the pick-up plates allows a linear position reading in both directions. Based on [20].

The length of the beam covered by the electrodes can be derived using Figure 4.8 where a topview onto the BPM is shown. The beam passes the structure with a finite horizontal displacement.

From geometry one finds

$$l_{\text{right}} = (a + x) \tan(\alpha) \quad (4.23)$$

$$l_{\text{left}} = (a - x) \tan(\alpha). \quad (4.24)$$

Solving for the horizontal displacement  $x$  gives

$$x = a + \frac{l_{\text{right}} - l_{\text{left}}}{l_{\text{right}} + l_{\text{left}}}. \quad (4.25)$$

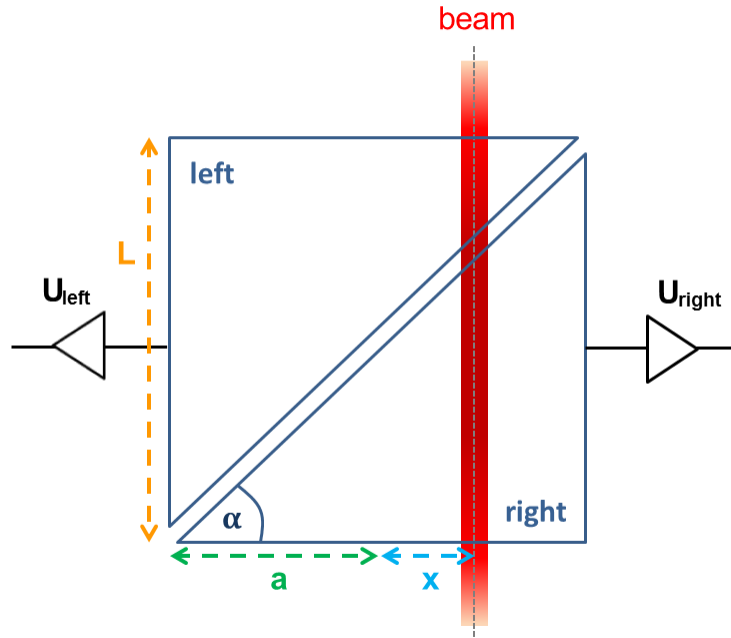


Figure 4.8: Topview on a shoebox BPM. The signal is proportional to the length of the beam that is covered by the BPM electrode. This allows a linear position determination. Based on [20].

Since the position reading is linear the displacement of the beam can be expressed by the difference of the measured voltages at the electrodes which leads to

$$x = a \frac{U_{\text{right}} - U_{\text{left}}}{U_{\text{right}} + U_{\text{left}}} = a \frac{\Delta U}{\Sigma U}. \quad (4.26)$$

A similar expression can be found for vertical displacements of the beam.

## 4.2 Coordinate system

A beam consists of many particles and each of those particles contributes to the propagation of the beam through the elements of the ring. The main purpose of investigating beam dynamics is to determine deviations from a specified reference orbit for all particles in the beam. Since describing these deviations with respect to a static laboratory coordinate system in most cases turns out to be cumbersome, it is convenient to choose a co-moving Cartesian coordinate system [17]. Its origin follows the reference particle which moves along the reference orbit with momentum  $\vec{p}_0$ . The reference orbit, also called closed orbit, is defined by the field distribution in the accelerator and is the one-turn periodic path of the reference particle. It can be measured as the averaged beam position at every element over a time much larger than the revolution time. The current position of the coordinate system on the reference orbit is called  $s$  and is calculated from an arbitrary but fixed starting point [21]. Figure 4.9 shows the idea of such a coordinate system. The unit vector  $\vec{e}_s$  always points along the reference particles momentum, while the unit vectors  $\vec{e}_x$  and  $\vec{e}_y$  span the plane orthogonal to  $\vec{e}_s$ , where  $\vec{e}_x$  lies collinear and  $\vec{e}_y$  is perpendicular to the plane of the storage ring. Assuming the reference path always lies in the horizontal plane, the transformation of the coordinate system from point A to point B on the reference path is given by

$$\vec{e}_{x,B} = \vec{e}_{x,A} \cos(\varphi) + \vec{e}_{s,A} \sin(\varphi), \quad (4.27)$$

$$\vec{e}_{y,B} = \vec{e}_{y,A}, \quad (4.28)$$

$$\vec{e}_{s,B} = -\vec{e}_{x,A} \sin(\varphi) + \vec{e}_{s,A} \cos(\varphi), \quad (4.29)$$

where

$$\varphi = \int_A^B \frac{ds}{\rho(s)}, \quad (4.30)$$

with bending radius  $\rho(s)$  [18].

The change of the unit vectors over time is given by

$$\dot{\vec{e}}_x = \frac{d\vec{e}_x}{d\varphi} \frac{d\varphi}{dt} = \frac{1}{\rho} \dot{s} \vec{e}_s, \quad (4.31)$$

$$\dot{\vec{e}}_y = 0, \quad (4.32)$$

$$\dot{\vec{e}}_s = \frac{d\vec{e}_s}{d\varphi} \frac{d\varphi}{dt} = -\frac{1}{\rho} \dot{s} \vec{e}_x. \quad (4.33)$$

To describe the trajectory of a particle  $\vec{r}(s)$  in the beam it is thus sufficient to know its position with respect to the trajectory of the reference particle  $\vec{r}_0(s)$ . Using the transverse deviations from the reference orbit of a single particle  $x(s)$  and  $y(s)$ , its trajectory can be parametrized as [21]

$$\vec{r}(s) = \vec{r}_0(s) + x(s)\vec{e}_x(s) + y(s)\vec{e}_y(s). \quad (4.34)$$

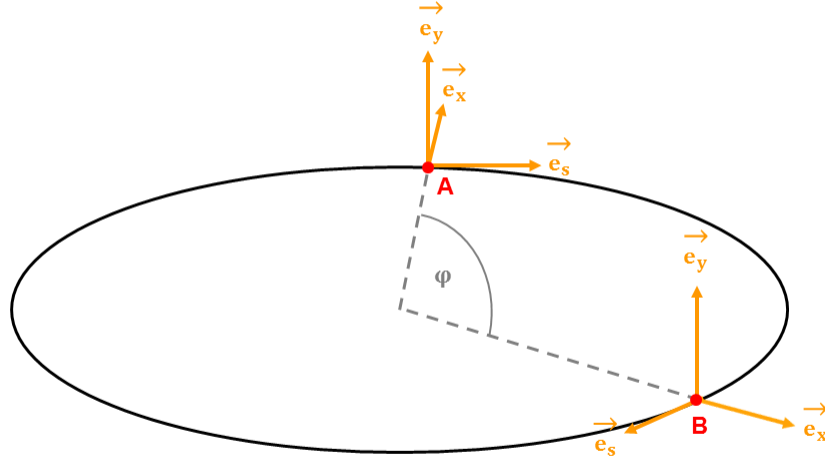


Figure 4.9: Co-moving coordinate system with its origin located at the reference particles' position. The s-axis is tangential to the reference orbit, the x-axis points in radial direction and y denotes the vertical direction. Based on [2].

### 4.3 Equation of motion

In this section the equations of motion of a particle passing the magnetic structure of an accelerator will be derived. Equation 4.34 describes the general trajectory of a particle relative to the reference orbit.

To formulate the equations of motion, the time derivatives of  $r(s)$  are needed. Using Equations 4.31 to 4.33 yields

$$\dot{\vec{r}}(s) = \dot{x}\vec{e}_x + \dot{y}\vec{e}_y + \left(1 + \frac{x}{\rho}\right)\dot{s}\vec{e}_s, \quad (4.35)$$

$$\ddot{\vec{r}}(s) = \left[\ddot{x} - \left(1 + \frac{x}{\rho}\right)\frac{\dot{s}^2}{\rho}\right]\vec{e}_x + \ddot{y}\vec{e}_y + \left[\frac{2}{\rho}\dot{x}\dot{s} + \left(1 + \frac{x}{\rho}\right)\ddot{s}\right]\vec{e}_s. \quad (4.36)$$

At every point in time the position  $s$  on the path through the accelerator is uniquely determined and can therefore be used as the independent variable.

Hence time derivatives can be transformed into derivatives with respect to  $s$  resulting in [18]

$$\dot{\vec{r}}(s) = x'\dot{s}\vec{e}_x + y'\dot{s}\vec{e}_y + \left(1 + \frac{x}{\rho}\right)\dot{s}\vec{e}_s, \quad (4.37)$$

$$\ddot{\vec{r}}(s) = \left[ x'' \dot{s}^2 + x' \ddot{s} - \left(1 + \frac{x}{\rho}\right) \frac{\dot{s}^2}{\rho} \right] \vec{e}_x + \left( y'' \dot{s}^2 + y' \ddot{s} \right) \vec{e}_y + \left[ \frac{2}{\rho} x' \dot{s}^2 + \left(1 + \frac{x}{\rho}\right) \ddot{s} \right] \vec{e}_s. \quad (4.38)$$

The Lorentz force (Equation 4.1) acts on particles traversing electromagnetic fields. Assuming a pure magnetic accelerator it reduces to

$$m\ddot{\vec{r}}(s) = q(\dot{\vec{r}}(s) \times \vec{B}). \quad (4.39)$$

Assuming a pure magnetic storage ring consisting only of dipoles and quadrupoles with only vertical magnetic fields the equations of motion for a particle traversing the magnetic structure are given by [17]

$$x''(s) + \left( \frac{1}{\rho^2(s)} - k(s) \right) x(s) = \frac{1}{\rho(s)} \frac{\Delta p}{p_0} \quad (4.40)$$

$$y''(s) + k(s)y(s) = 0. \quad (4.41)$$

#### 4.4 Transverse motion

Ignoring dispersive effects. i.e.  $\frac{\Delta p}{p_0} = 0$ , the equations of motion 4.40 and 4.41 become second order homogeneous differential equations of the form

$$x''(s) + K(s) x(s) = 0, \quad (4.42)$$

$$y''(s) + k(s) y(s) = 0, \quad (4.43)$$

with

$$K(s) = \frac{1}{\rho^2(s)} - k(s). \quad (4.44)$$

Equations 4.42 and 4.43 are known as *Hill's differential equations*.

Since both equations are of equal form and thus can be solved with the same procedure, the following calculations will only consider the solution in horizontal direction. The vertical solution can be found analogously. Except for the  $s$  dependent coefficient  $K(s)$  which is periodic over one turn with a length of  $C$ , i.e.  $K(s+C) = K(s)$ , the differential equation resembles the one of a harmonic oscillator. For simplicity the  $s$  dependence will not be explicitly mentioned in every step in the following calculations. By analogy with the harmonic oscillator the ansatz

$$x(s) = Au(s)\cos[\Psi(s) + \Psi_0] \quad (4.45)$$

is chosen, where  $A$  and  $\Psi_0$  are the constants of integration defining the trajectory of every individual particle. Inserting equation 4.45 into Equation 4.42 leads to

$$\underbrace{(u'' - u\Psi'^2 + uK)}_{\text{I}} \cos(\Psi + \Psi_0) - \underbrace{(2u'\Psi' + u\Psi'')}_{\text{II}} \sin(\Psi + \Psi_0) = 0. \quad (4.46)$$

Independently of each other, terms I and II must vanish for Equation 4.46 to hold. Thus

$$u'' - u\Psi'^2 + uK = 0 \quad (4.47)$$

and

$$2u'\Psi' + u\Psi'' = 0. \quad (4.48)$$

Integrating Equation 4.48 twice yields

$$\Psi'(s) = \frac{1}{u^2} \quad (4.49)$$

and

$$\Psi(s) = \int_0^s \frac{ds'}{u^2(s')}. \quad (4.50)$$

Inserting 4.49 into Equation 4.47 the differential equation of  $u(s)$  can finally be written as

$$u''(s) + K(s)u(s) = \frac{1}{u^3(s)}, \quad (4.51)$$

which has a uniquely defined periodic solution  $u(s)$ . Introducing the betatron function  $\beta(s)$  with

$$\beta(s) = u^2(s) \quad (4.52)$$

the general solution of Hill's differential equation are pseudo-harmonic oscillations, so called betatron oscillations, about the reference orbit with an s dependent amplitude given by

$$x(s) = A\sqrt{\beta(s)} \cos[\Psi(s) + \Psi_0] \quad (4.53)$$

and

$$x'(s) = \frac{A}{\sqrt{\beta(s)}} \left[ \underbrace{\frac{1}{2}\beta(s)}_{:= -\alpha(s)} \cos[\Psi(s) + \Psi_0] - \sin[\Psi(s) + \Psi_0] \right]. \quad (4.54)$$

The parameter  $A$  denotes the amplitude of the oscillation and  $\Psi_0$  indicates the initial phase. The betatron function  $\beta(s)$  depends on the magnetic structure of the accelerator and can be interpreted as a measure of the transverse beam profile. The betatron tune, defined as the number of betatron oscillations per turn, is calculated by [21]

$$Q = \frac{1}{2\pi} \int_s^{s+C} \Psi' ds = \frac{1}{2\pi} \int_s^{s+C} \frac{ds'}{\beta(s)}. \quad (4.55)$$

The particles thus perform oscillations about the reference orbit. The oscillation amplitude is dependent on the magnetic structure ( $\beta(s)$ ) and on the integration constant  $A$ . It is different for each particle as  $A$  is an intrinsic quantity of a particle. Figure 4.10 illustrates the transverse motion of several particles along the accelerator. The particle with the largest value of  $A$  defines the envelope of the particle trajectories. All other particles move within the boundaries defined by this envelope.

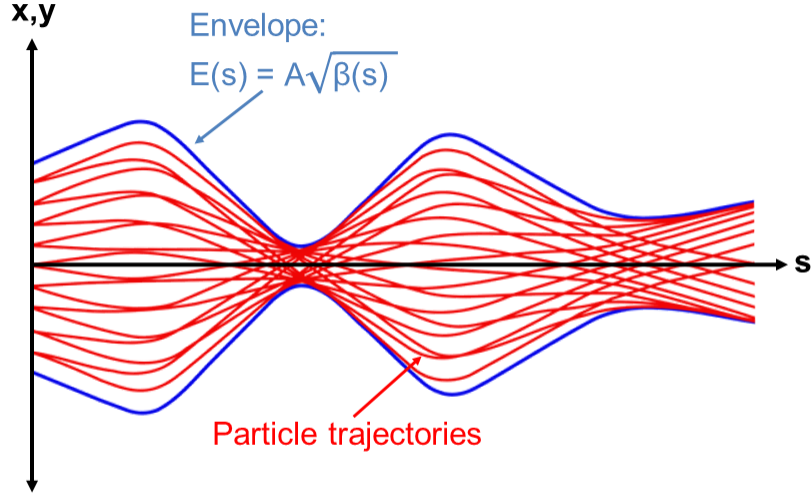


Figure 4.10: The transverse motion of all particles in the beam is limited by the particle with the largest value of  $A$ . Its trajectory along the ring forms the envelope for all other particles. Based on [18].

#### 4.4.1 Dispersion

Considering now particles with a non-vanishing momentum deviation  $\frac{\Delta p}{p_0}$ . From Equation 4.40 it follows that a momentum deviation only influences the trajectory of the particle in sections with a finite bending radius  $\rho$ . It is therefore sufficient to solve the equation of motion only within a bending magnet with constant bending radius  $\rho$  where a vanishing quadrupole contribution, i.e. a homogeneous dipole field is assumed. Equation 4.40 then turns into

$$x''(s) + \frac{1}{\rho^2}x(s) = \frac{1}{\rho} \frac{\Delta p}{p_0}. \quad (4.56)$$

The dispersion function  $D(s)$  is defined for a momentum spread of  $\frac{\Delta p}{p_0} = 1$  and fulfills the differential equation

$$D''(s) + \frac{1}{\rho^2}D(s) = \frac{1}{\rho}, \quad (4.57)$$

with the periodicity conditions

$$D(s + C) = D(s), \quad (4.58)$$

$$D'(s + C) = D'(s) \quad (4.59)$$

and the boundary conditions

$$D(0) = D_0, \quad (4.60)$$

$$D'(0) = D'_0. \quad (4.61)$$

The modified horizontal motion of a particle is then given by

$$x_{\text{total}}(s) = x(s) + x_D(s) = x(s) + D(s) \frac{\Delta p}{p_0} \quad (4.62)$$

where  $x(s)$  describes the betatron oscillation and  $x_D(s)$  represents the additional motion due to momentum deviation [21].

The differential equation 4.57 is solved using an ansatz of a harmonic oscillation and the particular solution [18]

$$D_p(s) = \rho. \quad (4.63)$$

Incorporating the boundary conditions finally leads to

$$D(s) = D_0 \cos\left(\frac{s}{\rho}\right) + \rho D'_0 \sin\left(\frac{s}{\rho}\right) + \rho \left(1 - \cos\left(\frac{s}{\rho}\right)\right) \quad (4.64)$$

$$D'(s) = -\frac{D_0}{\rho} \sin\left(\frac{s}{\rho}\right) + D'_0 \cos\left(\frac{s}{\rho}\right) + \sin\left(\frac{s}{\rho}\right). \quad (4.65)$$

Besides the betatron oscillations the particles with non-vanishing momentum deviations now oscillate around a dispersion trajectory defined by  $\frac{\Delta p}{p_0}$ .

The path length of a particle in the accelerator therefore differs from the reference orbit length. It can easily be shown that a dispersive particle travels the distance [18]

$$ds = \frac{\rho + x_D}{\rho} ds_0 \quad (4.66)$$

at positions with non-vanishing dispersion, where  $ds_0$  denotes the path length the reference particle passes in the same time interval.

With  $L_0$  denoting the path length of the reference particle the total path length over one turn is given by

$$L = L_0 + \Delta L = \oint \frac{\rho + x_D}{\rho} ds = \oint ds + \frac{\Delta p}{p_0} \oint \frac{D(s)}{\rho(s)} ds \quad (4.67)$$

which leads to a change in the path length of

$$\Delta L = \frac{\Delta p}{p_0} \oint \frac{D(s)}{\rho(s)} ds. \quad (4.68)$$

#### 4.4.2 Chromaticity

Particles with a momentum deviation from the reference momentum  $p_0$  are exposed to a slightly different quadrupole strength than the reference particle and are therefore focused differently. The error of chromatic aberration is already well known from optics. The effect is illustrated in Figure 4.11, where the focusing quadrupole is represented by a focusing lens.

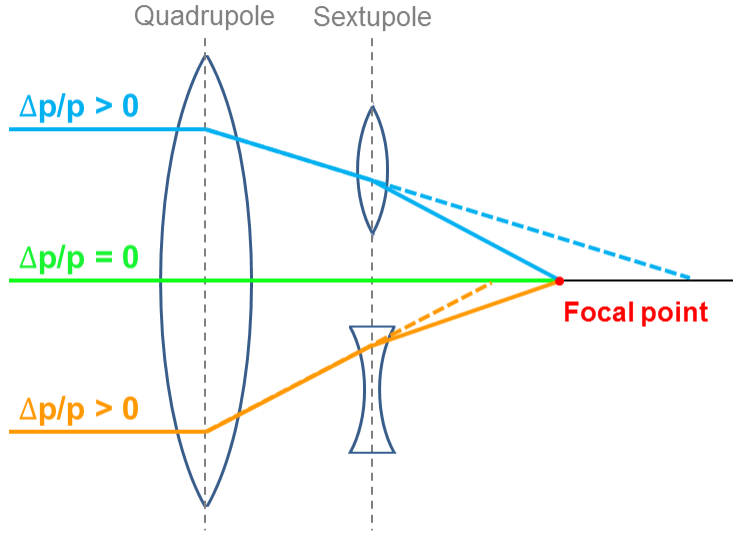


Figure 4.11: The effect of momentum dependence of the focusing strength of a quadrupole is called chromaticity. Depending on the radial position of the particles, sextupoles create quadrupole components which can correct the chromaticity effect if they are positioned in dispersive regions. Based on [18].

Assuming only small deviations from the reference momentum the quadrupole strength seen by a particle with momentum  $p = p_0 + \Delta p$  is given by

$$k(p) = -\frac{q}{p} g = -\frac{q}{p_0 + \Delta p} g \approx -\frac{q}{p_0} \left(1 - \frac{\Delta p}{p_0}\right) g = k_0 - \Delta k. \quad (4.69)$$

A momentum deviation can be interpreted as a quadrupole error [18]

$$\Delta k = \frac{\Delta p}{p_0} k_0. \quad (4.70)$$

One can show that the quadrupole error leads to a change in the betatron tune over a distance  $ds$  of [18]

$$dQ = \frac{\Delta p}{p_0} \frac{1}{4\pi} k_0 \beta(s) ds. \quad (4.71)$$

Since the particle retains its momentum deviation over many turns, all quadrupoles have the same error from the particles perspective. Hence the total tune shift is calculated by integrating over all quadrupoles in the accelerator. The dimensionless quantity

$$\xi := \frac{\Delta Q}{\frac{\Delta p}{p_0}} = \frac{1}{4\pi} \oint k(s) \beta(s) ds \quad (4.72)$$

is called natural chromaticity and increases with growing focusing strength  $k(s)$ . The main contributions come from quadrupoles with large focusing strengths where the betatron function is large. Since a tune shift can lead to a working point at optical resonances [17] and hence to a loss of particles, chromaticity has to be compensated for. A correction is performed at positions where the particles are separated according to their momenta, i.e. at positions with non-vanishing dispersion. At these positions sextupole magnets are installed which have a focusing strength dependent on the transverse position. The principle of compensating chromaticity using sextupoles is schematically illustrated in Figure 4.11.

## 4.5 Orbit correction

Due to the magnetic structure of the accelerator the closed orbit deviates from the trajectory through all magnet centers. Considering field imperfections, magnet misalignments and other external effects on the beam, the closed orbit changes and its deviations get larger. To ensure an orbit that resembles the desired target orbit as closely as possible, a correction system is needed. In many cases the target orbit is equal to the trajectory through the magnet centers but one can also imagine desired orbits with  $x \neq 0$  and  $y \neq 0$ . To manipulate the orbit, additional dipoles are used to steer the beam in vertical and horizontal direction. In order to find the best field strength configurations of these corrector magnets it is essential to know the influence of every single corrector in the orbit. The orbit response due to perturbations at one of the corrector magnets can be measured using the beam position monitors. It is noticeable that this measurement only takes place at discrete positions and that the largest parts of the true orbit stay unobserved. An unfavorable distribution of BPMs could lead to

a situation, where large, local orbit distortions are not recognized by the measurements and to which the orbit correction therefore cannot react. Minimizing the BPM orbit readings therefore is only the optimal correction method if the electronic or mechanical offset of the BPMs with respect to the adjacent quadrupoles is removed [22].

#### 4.5.1 Orbit response matrix

Assuming  $m$  BPMs and  $n$  corrector dipoles the  $n$ -dimensional vector  $\vec{x}$  represents the measured orbit with respect to the path through the magnet centers. The orbit response due to perturbations at the corrector magnets can be written as

$$\Delta\vec{x} = R\Delta\vec{k}, \quad (4.73)$$

with  $\vec{k}$  summarizing all corrector strengths. The  $m \times n$  dimensional matrix  $R$  is the so called *orbit response matrix* involving all BPM responses  $i$  ( $i = 1, \dots, m$ ) to a perturbation at corrector  $j$  ( $j = 1, \dots, n$ ) given by the matrix elements

$$R_{ij} = \frac{\Delta x_i}{\Delta k_j}. \quad (4.74)$$

The orbit response matrix can also be calculated from the optical functions and it can be shown that the matrix elements then read [23]

$$R_{ij} = \frac{\sqrt{\beta_i \beta_j}}{2\sin(\pi Q)} \cos(\Psi_i - \Psi_j - \pi Q), \quad (4.75)$$

where  $Q$  is the betatron tune,  $\beta_{i,j}$  are the betatron functions at the respective position of the BPM and the corrector and  $(\Psi_i - \Psi_j)$  denotes the phase advance between BPM and corrector magnet.

An efficient orbit correction uses the orbit response matrix to determine the set of corrector strengths that lead to the desired orbit. With a given target orbit  $\vec{x}_{\text{tar}}$  the condition under which the problem has to be solved reads

$$\Delta\vec{x} \stackrel{!}{=} \vec{x}_{\text{tar}} - \vec{x}. \quad (4.76)$$

Since the dimensions of the orbit response matrix depend on the number of BPMs and correctors,  $R$  is not always invertible. For a set of less correctors than BPMs there is in general no analytical solution. Besides solving for  $\Delta\vec{k} = R^{-1}\vec{x}$  one minimizes the residual error  $\delta \equiv ||R\Delta\vec{k} - \Delta\vec{x}||$  with respect to  $\Delta\vec{k}$ :

$$\delta = \sqrt{(R\Delta\vec{k} - \Delta\vec{x})^2} \rightarrow \min!. \quad (4.77)$$

Squaring Equation 4.77 and taking the derivative with respect to  $\Delta\vec{k}$  yields [24]

$$\begin{aligned} \frac{\partial \delta^2}{\partial \Delta\vec{k}} &= 2R^T(R\Delta\vec{k} - \Delta\vec{x}) \stackrel{!}{=} 0 \\ \Rightarrow \Delta\vec{k} &= (R^T R)^{-1} R^T \Delta\vec{x}. \end{aligned} \quad (4.78)$$

It is hence necessary to find a way to invert the matrix  $(R^T R)$ . There are different algorithms for orbit correction, some of them work on a global basis others only perform local corrections. The method that will be used in this thesis is the so called *Singular Value Decomposition*, a numerical algorithm used for matrix inversion. A detailed description is given in [23].

## 5 Closed Orbit Influencing Effects

In this chapter different influences on the closed orbit of COSY are investigated. The simulations are performed with *Methodical Accelerator Design* version 10 (MAD-X) [3].

In order to understand the transverse deviations of the beam inside COSY, it is crucial to think about possible effects influencing the particles and to quantify their impact. Various misalignments can lead to false signals, limiting the measurement of an upper bound of the deuteron EDM. From section 2.2 it is known that an EDM of  $5 \cdot 10^{-19}$  e-cm is distinguishable and can be measured at the precursor experiment at COSY if the randomized error standard deviation of displaced quadrupoles is below 0.1 mm. Respectively for an EDM of  $5 \cdot 10^{-20}$  e-cm the positioning of the quadrupoles must be within a standard deviation smaller than 0.01 mm [2]. One challenge in the process of preparing the precursor experiment is thus to provide a precise beam with small vertical deviations from the path through the magnet centers. With the current setup of COSY the measured closed orbit yields a *RMS* in the transverse direction of the order of 1 mm. Simulating various imperfections and investigating their effect on the closed orbit helps understanding the measured orbit and give a hint of possible improvements to narrow down the transverse deviations.

The underlying model for all simulations includes the dipoles, quadrupoles and sextupoles at COSY as well as the corrector magnets and BPMs. The sextupole strengths are set to zero resulting in a linear machine. The optics is adjusted in a way that the dispersion is zero in the straight sections. Figure 5.1 shows the optical functions for the simulation model. Several misalignments and distortions can now be included in the reference model to study their effects on the closed orbit.

### 5.1 Magnet misalignments

The magnet' strengths and their positions mainly determine how the beam propagates through the ring. It is therefore important to investigate the effect of misaligned quadrupoles and dipoles in the model and to compare them to the actual setup at COSY.

#### 5.1.1 Quadrupole displacement

If a quadrupole is shifted in the vertical or longitudinal direction, the beam passes the magnet at different positions than in the ideal case and thus experiences a different field. Therefore, the path of the beam through the machine and the vertical closed orbit changes. The dominant influence comes from shifts along the x- and y-axis since this directly changes the force acting on the passing particles even for a beam moving on the magnetic axes.

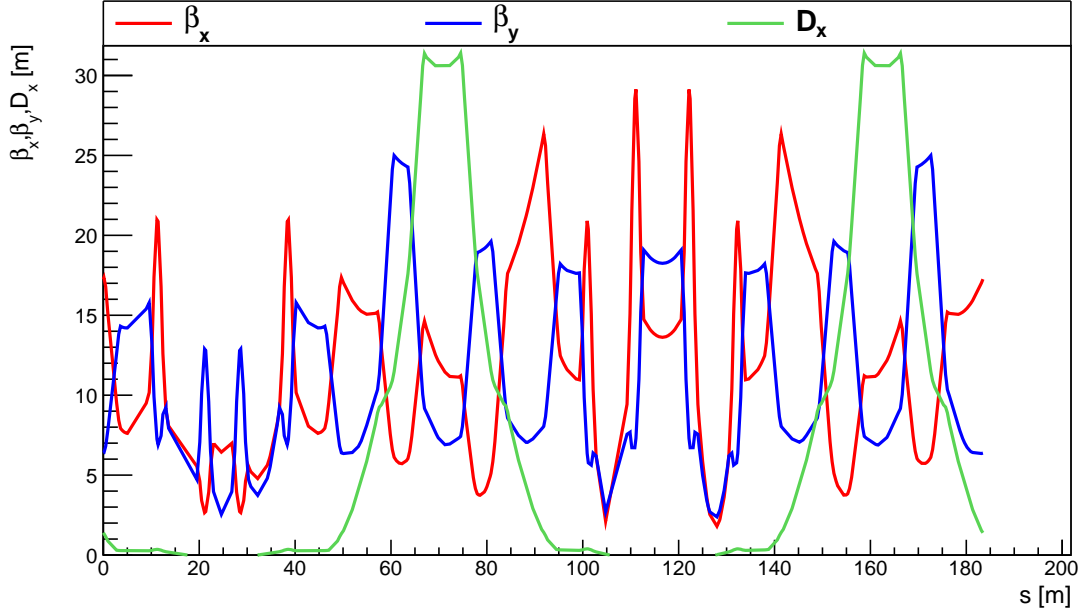


Figure 5.1: Optical functions of the COSY model in MAD-X. The dispersion is adjusted to zero in the straight sections by tuning the quadrupole strengths accordingly.

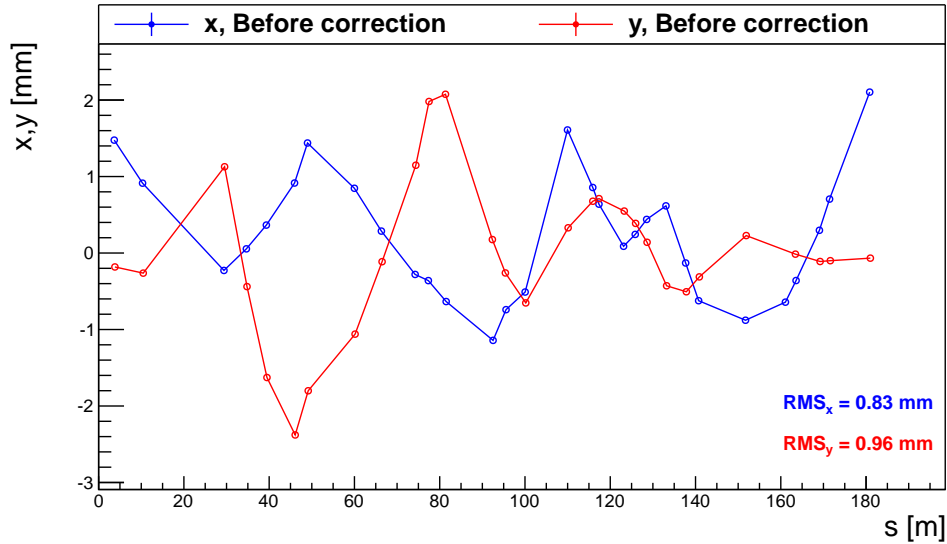
In the simulations, the displacement of each quadrupole is randomly generated using a Gaussian distribution and assuming equal standard deviation but independence in all three directions:

$$\Delta(x, y, s) = \text{Gauss}(0, \sigma_{x,y,s}) \quad \text{with} \quad \sigma_x = \sigma_y = \sigma_s. \quad (5.1)$$

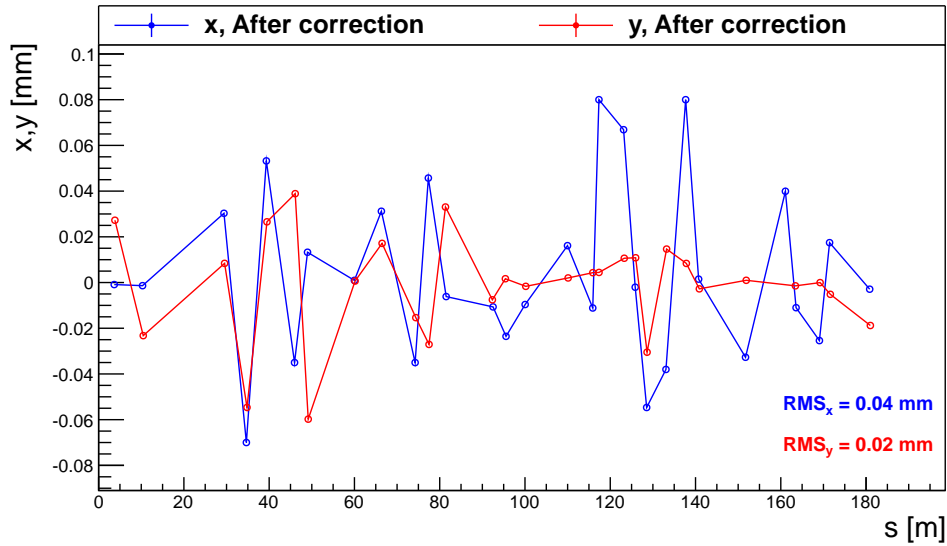
The calculation is performed for 100 logarithmically equidistantly distributed standard deviations between zero and one millimeter and for 1000 random samples of magnet displacements for each value of  $\sigma$ . During each simulation the closed orbit is calculated for the given set of displacements before and after applying the orbit correction using the SVD<sup>4</sup> algorithm. In Figure 5.2 the uncorrected and corrected closed orbits in both transverse directions are shown exemplarily for one random configuration of displacements with a standard deviation of 0.1 mm. The orbits show the transverse deviation from the path through the magnet centers where only BPM readings are taken into account. Therefore the curves do not end at the same points where they start, although the orbit is closed. Averaging over all 1000 sample values leads to the mean *RMS* value in horizontal and vertical direction.

For the results of the internal orbit correction of MAD-X one has to crosscheck whether the suggested strengths for the corrector magnets are in a possible range and can be realized at COSY. Therefore Figure 5.3 displays the maximum corrector strengths used in the model for every standard deviation of the Gaussian random generation process. For standard deviations below 0.2 mm all steerer values lie in an acceptable range and could be taken over to the real machine.

<sup>4</sup>Singular Value Decomposition



(a)



(b)

Figure 5.2: Example of simulated transverse closed orbits at COSY for a representative random sample of Gaussian distributed quadrupole displacements with a standard deviation of 0.1 mm. The uncorrected orbits are shown in (a) the corrected ones in (b).

Considering larger standard deviations, the steerer strengths reach a level that cannot be achieved at every energy at COSY. At maximum energy for instance the maximum corrector strength at COSY is of the order of 1 mrad. At lower particle energies, corrector strengths up to 10 mrad can be realized.

The orbit correction of MAD-X thus generates better results than the orbit correction of the real machine for large standard deviations. Therefore the simulation results before the orbit correction may be more trustworthy than the ones after applying the internal correction.

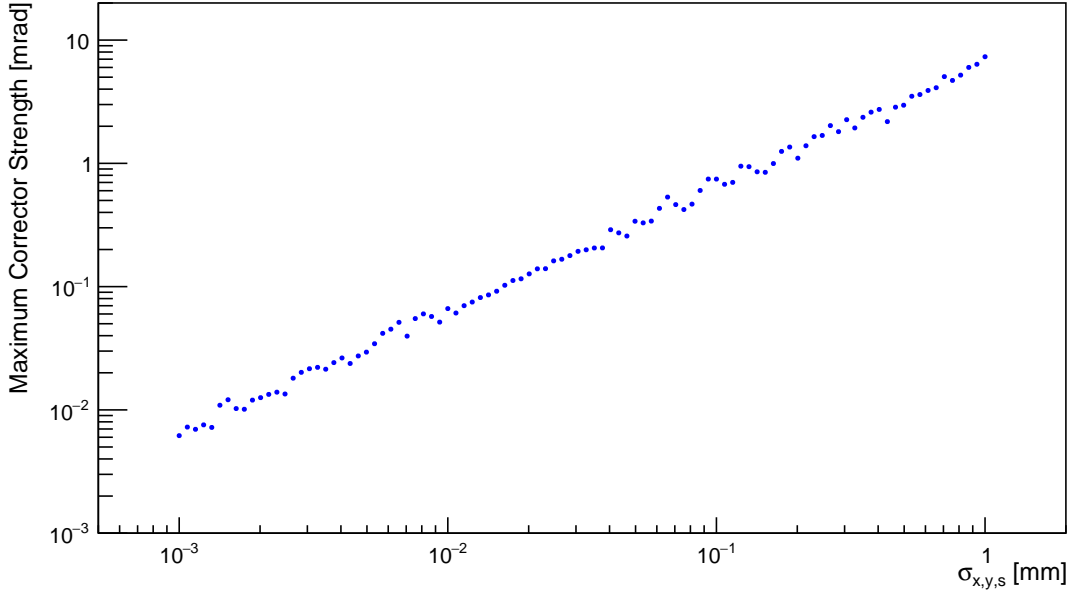
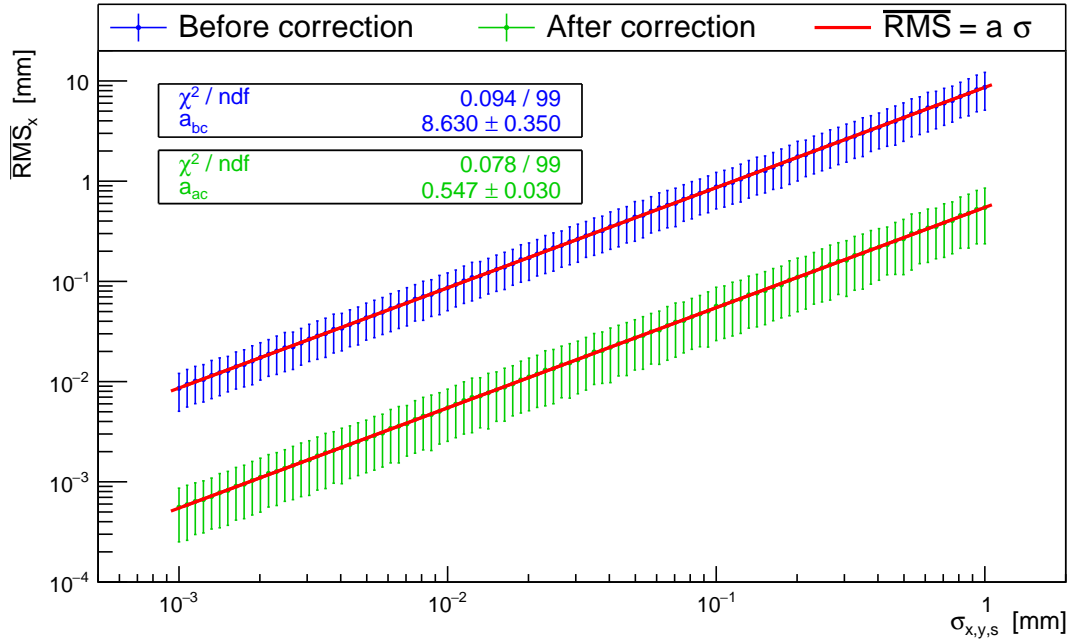


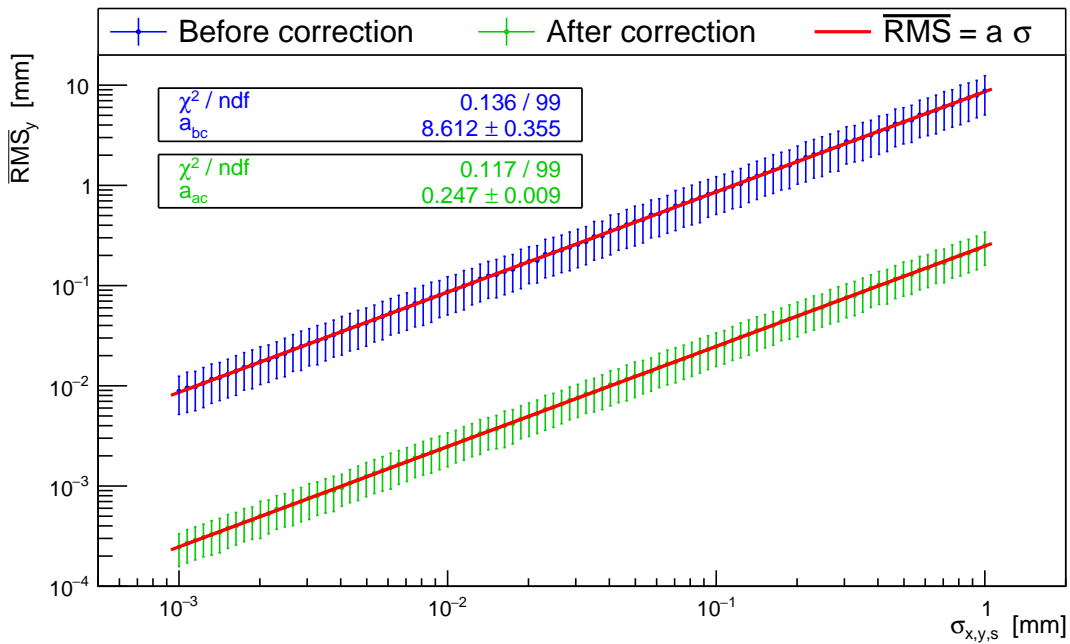
Figure 5.3: Maximum corrector strength used after orbit correction in the simulation model. The values represent the maximum corrector strength over all random samples.

Figure 5.4 shows the results of the analysis in both transverse directions.

Considering only the values at the BPMs models the realistic case since one cannot measure the beam position in other places during real machine operation. In turn, analyzing the orbit with respect to all elements leads to the true *RMS* which generally cannot be measured. The orbit correction lowers the transverse *RMS* of the orbit by approximately one order of magnitude. The linear behavior of the curves can be explained by the machine model including only active dipoles and quadrupoles and thus only constant or linear changing fields in transverse directions. For ideal elements, i.e. no displacement of magnets, the closed orbit is identical to the path through the centers of all magnets. Therefore linear fits with vanishing y-intercept are performed to describe the behavior in a physical meaningful manner. The slopes of the linear fits are summarized in Table 1. The corresponding  $\chi^2/ndf$  values are very small which indicates that the errors on the mean *RMS* values resulting from the averaging over all samples are still overestimated. For the uncorrected orbit it makes no difference if the BPM data or the orbit deviation values at all elements are used. Here the BPMs sufficiently describe the full orbit. For the corrected orbit one can identify a difference by comparing the *RMS* of the corrected orbit, resulting on the one hand from the BPM readings and on the other hand from taking the beam position at all elements into account. In the case of BPM measurements the *RMS* is always slightly lower than the true closed orbit *RMS*. This is a plausible effect since the correcting algorithm (SVD) corrects the orbit with respect to the values measured at the BPMs. Hence the correction has its strongest effect at the positions of the BPMs where it tries to narrow down the beam as closely as possible to the center of the BPM.



(a)



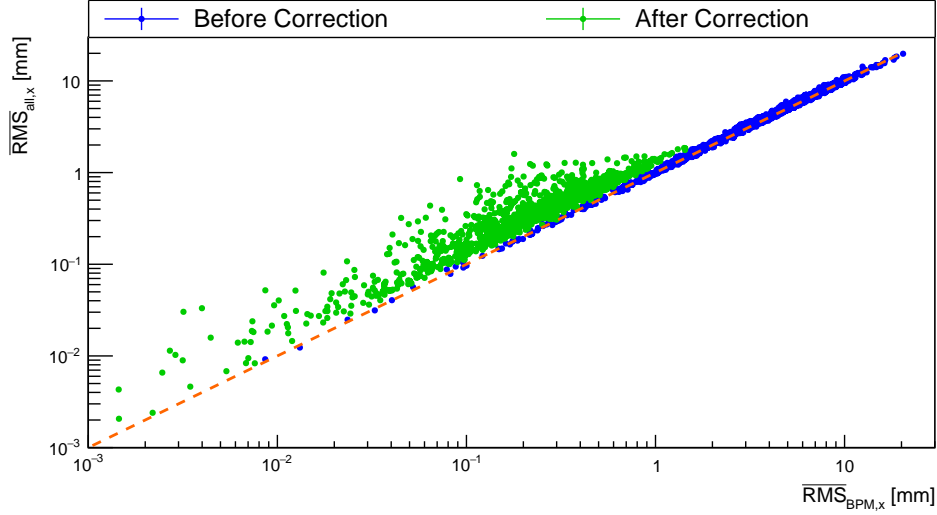
(b)

Figure 5.4: Influence in horizontal (a) and vertical (b) direction of Gaussian distributed quadrupole displacements with increasing standard deviation of magnet displacement. The mean  $RMS$  values are calculated according to the BPM readings and therefore represent the measurable orbit.

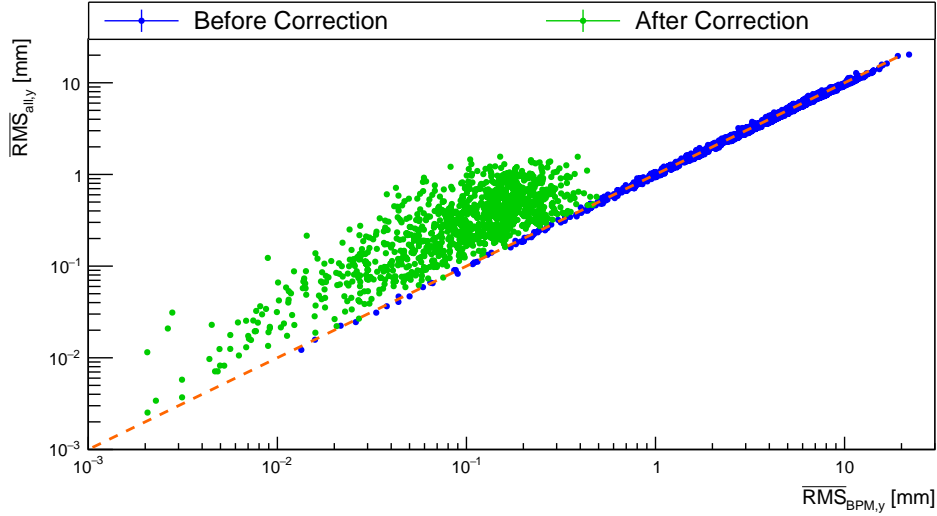
Quadrupole displacement, Fit parameters					
		$a_x$	$a_y$	$\chi^2/\text{ndf, x}$	$\chi^2/\text{ndf, y}$
BPMs	uncorrected	$8.630 \pm 0.350$	$8.612 \pm 0.355$	0.094/99	0.136/99
	corrected	$0.547 \pm 0.030$	$0.247 \pm 0.009$	0.078/99	0.117/99
all elements	uncorrected	$8.807 \pm 0.345$	$8.383 \pm 0.333$	0.094/99	0.137/99
	corrected	$0.940 \pm 0.039$	$0.847 \pm 0.045$	0.086/99	0.108/99

Table 1: Parameters of the linear fit to the mean *RMS* values resulting of quadrupole displacements. The subscript of the slope of the linear fits  $a$  indicates the considered transverse direction. The measurable values are indicated by *BPMs*, the parameters corresponding to the true *RMS* values are indicated by *all elements*.

Figure 5.5 compares the true to the measured *RMS*. Here a representative random sample is chosen to illustrate the effects. The true *RMS* ( $RMS_{\text{all},x(y)}$ ) is the result of taking all elements into account. The measurable *RMS* ( $RMS_{\text{BPM},x(y)}$ ) is calculated only from the BPM readings. Whereas there is no significant difference between the *RMS* values of the uncorrected orbits, the values after the orbit correction show, that the real *RMS* is higher than the measured one. As the algorithm only takes BPM measurements into account and ignores the effect in the rest of the ring, the true *RMS* values after orbit correction fluctuate in a larger range. This can be seen by the significantly larger spread of the true *RMS* values after the orbit correction.



(a)



(b)

Figure 5.5: Comparison of measurable and true  $RMS$  values in x-direction (a) and in y-direction (b). The measurable values ( $\overline{\text{RMS}}_{\text{BPM},x(y)}$ ) only take the BPM readings into account. The true  $RMS$  ( $\overline{\text{RMS}}_{\text{all},x(y)}$ ) is calculated with respect to the orbit deviations at every element in the ring. The dashed lines illustrate a line with a slope of one.

### 5.1.2 Quadrupole rotation

Besides shifts in every direction, magnets can also be rotated around every axis. Similar to the investigation of the quadrupole shifts, the rotations of every magnet are randomly generated according to

$$\Delta(\phi, \Theta, \Psi) = \text{Gauss}(0, \sigma_{\phi, \Theta, \Psi}) \quad \text{with} \quad \sigma_{\phi} = \sigma_{\Theta} = \sigma_{\Psi}, \quad (5.2)$$

where  $\phi$  ( $\Theta$ ,  $\Psi$ ) indicates a rotation around the x- (y-, s-) axis. Again 1000 different random samples of rotations are generated for each standard deviation. The standard deviation varies from zero to one milliradian and is divided logarithmically equidistantly into 100 steps. The results for the uncorrected and the corrected *RMS* values of the closed orbits in both transverse directions are given in Figure 5.6. The analysis is performed on the data taken only from the BPMs, i.e. the measurable orbit, because all simulations aiming at understanding the measured orbit at COSY resulting from BPM measurements. The slope of the linear fits with zero intercept are shown in Table 2. For completeness also the slope parameters of the fits to data with respect to all elements in the ring are given. As before they represent the true *RMS* values of the closed orbit in the machine.

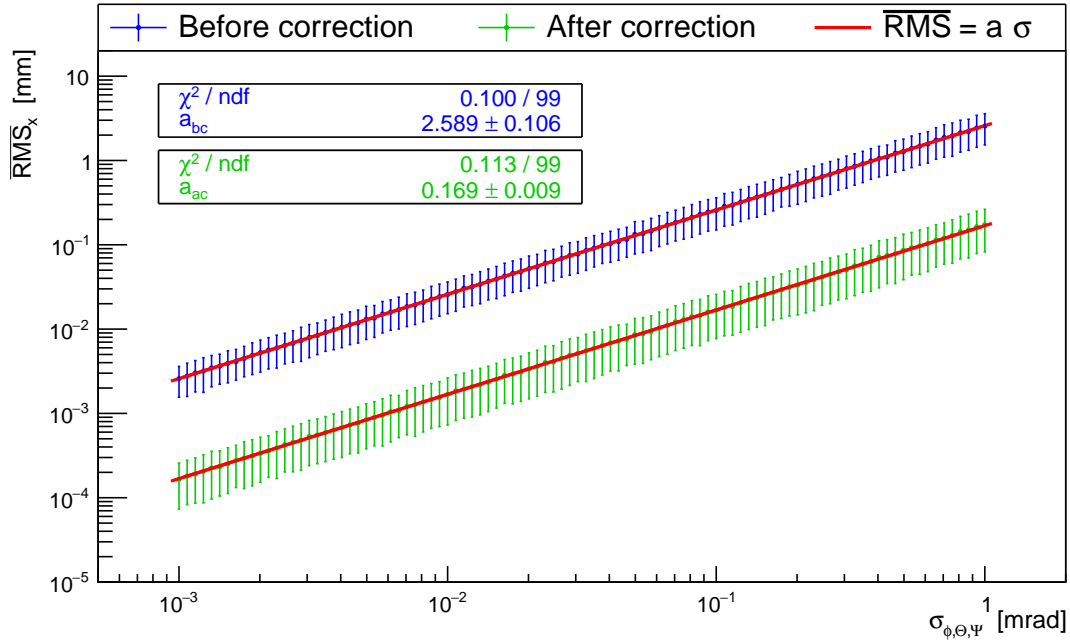
Quadrupole rotation, Fit parameters					
		$a_x$ [mm/mrad]	$a_y$ [mm/mrad]	$\chi^2/\text{ndf, x}$	$\chi^2/\text{ndf, y}$
BPMs	uncorrected	$2.589 \pm 0.106$	$2.576 \pm 0.109$	0.100/99	0.094/99
	corrected	$0.169 \pm 0.009$	$0.070 \pm 0.003$	0.113/99	1.423/99
all elements	uncorrected	$2.643 \pm 0.104$	$2.507 \pm 0.102$	0.095/99	0.094/99
	corrected	$0.290 \pm 0.012$	$0.255 \pm 0.014$	0.096/99	0.111/99

Table 2: Parameters of the linear fit to the mean *RMS* values resulting of quadrupole rotations. The subscript of the slope of the linear fits  $a$  indicates the considered transverse direction. The measurable values are indicated by *BPMs*, the parameters corresponding to the true *RMS* values are indicated by *all elements*.

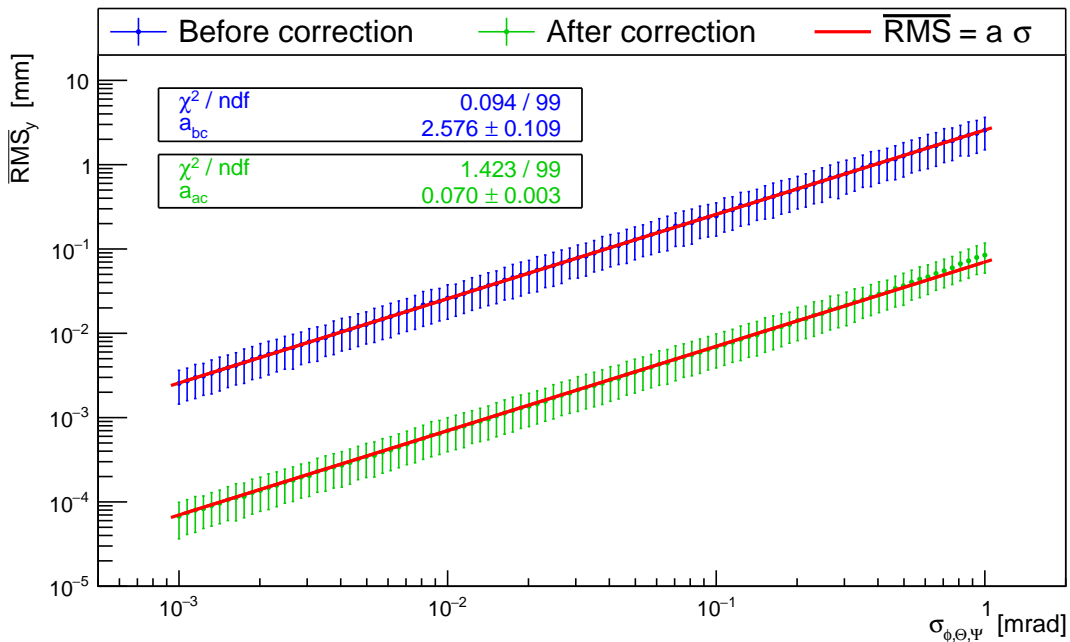
The effect of rotations is smaller by a factor of approximately three compared to shifting the quadrupoles. This result is plausible and can be understood by considering an ideally adjusted beam entering the quadrupole. Without any placement errors, the beam would traverse the magnet at the center and would not experience any force. If the quadrupole is now shifted for example in x-direction with respect to the incident beam, the particles are exposed to a field proportional to the shift  $\Delta x$ . If the quadrupole however is rotated in the horizontal plane, i.e. around the y-axis, the particles' deviation from the ideal path through the magnet increases linearly with the covered distance and is limited by the length of the quadrupole and the rotation angle. As illustrated in Figure 5.7, the force acting on the particles is thus zero as they enter the magnet and increases as they pass. The deviation from the ideal axis in the rotated quadrupole can be expressed by

$$\Delta x(s) = l(s) \tan(\alpha), \quad (5.3)$$

where  $l(s)$  describes the covered distance in the magnet. For angles between zero and one milliradian and typical quadrupole lengths in the range of 0.3 m to 0.6 m the maximum deviation of the particles at the end of the magnet  $\Delta x_{max}$  is smaller than the corresponding shift. The cumulative effect of rotating quadrupoles is thus smaller than effects from shifting the magnets.



(a)



(b)

Figure 5.6: Influence in horizontal (a) and vertical (b) direction of Gaussian distributed quadrupole rotations with increasing standard deviation. The mean  $RMS$  values are calculated according to the BPM readings and therefore represent the measurable orbit.

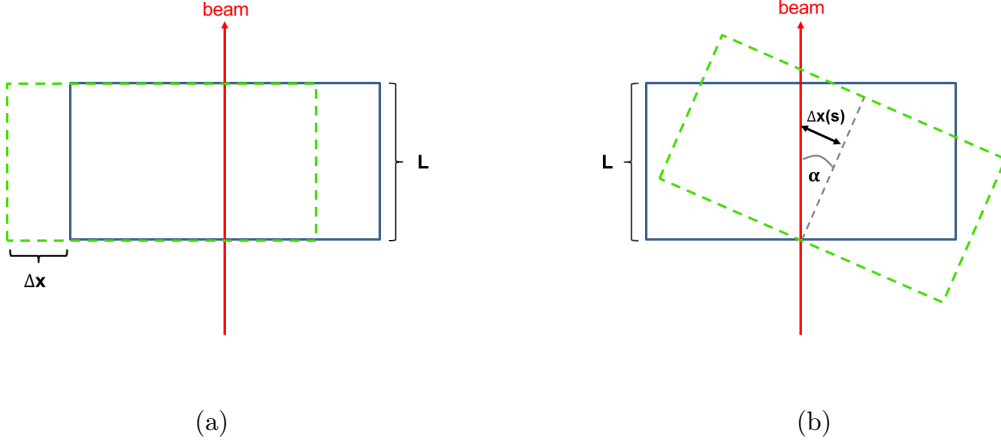
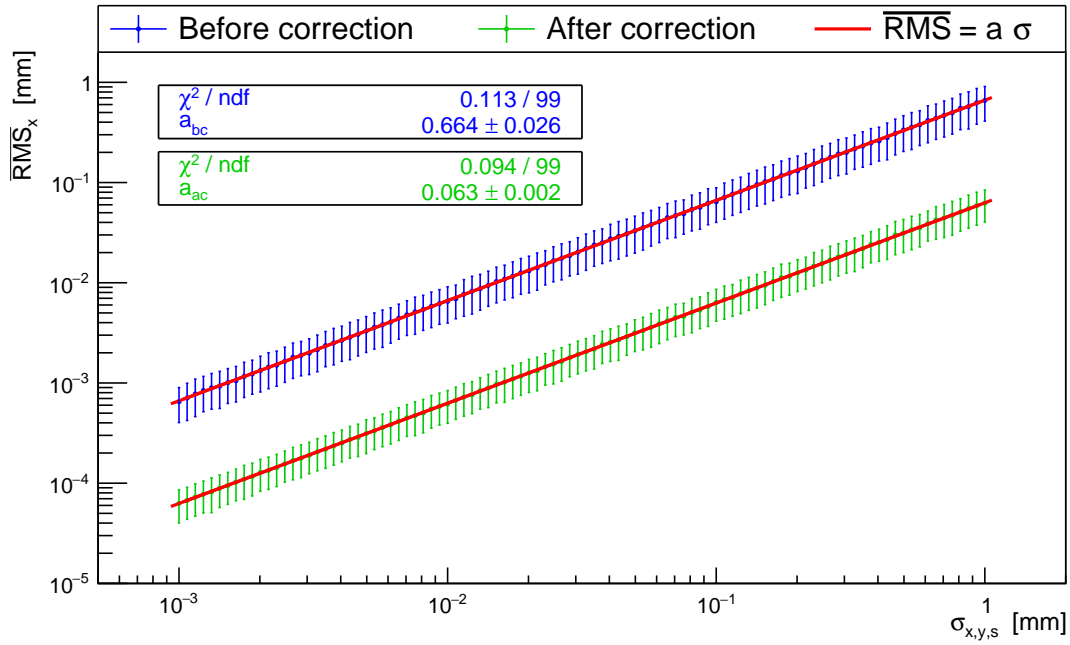


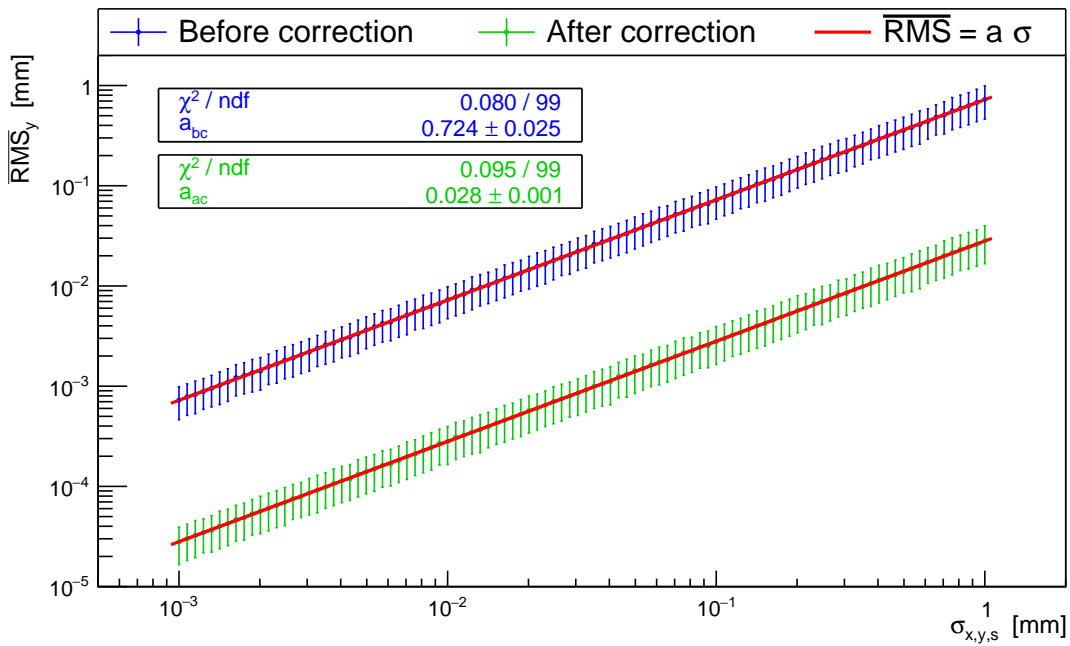
Figure 5.7: Comparison of shifting and rotating a quadrupole in the horizontal plane. Figure (a) illustrates a shift along the x-axis, (b) shows a rotation about the y-axis. A shift along the horizontal axis directly leads to a shifted beam position relative to the magnet center whereas a rotation leads to a linearly increasing horizontal displacement of the beam inside the magnet.

### 5.1.3 Dipole displacement

Considering further effects, also the positioning of the dipoles in the ring can influence the beam. A dipole shifted in longitudinal direction changes the bending of the beam which will have an influence on the closed orbit in horizontal direction. The quadrupoles are ideally positioned and their longitudinal placement is done with respect to the ideal positions of the dipoles. Thus for ideally placed dipoles the quadrupoles are positioned in a way that the beam passes the magnet centers. If the dipoles are shifted longitudinally, the beam no longer enters the quadrupoles on the magnetic axis but with a horizontal deviation. Since the magnetic field in vertical direction depends linearly on the horizontal position of the beam in the quadrupole, a force in x-direction acts on the particles and additionally influences the orbit in the horizontal plane. Due to fringe fields of the dipoles and the entrance and exit angles there is also an effect in vertical direction if the dipoles are shifted along the three axes. Dipole displacements are generated according to Equation 5.1. For each standard deviation 1000 runs are performed with different random seeds. The horizontal average closed orbit *RMS* is displayed in Figure 5.8. The slopes of the linear fits are given in Table 3, on the one hand for the *RMS* values related to BPM readings and on the other hand for the true *RMS* related to orbit deviations at all elements. Again the high estimated errors lead to small values of  $\chi^2/ndf$ . The effect on the mean closed orbit *RMS* is one order of magnitude smaller than the effect of displaced quadrupoles. This is due to the different field configurations of the two magnet types. In a quadrupole, the transverse field components increase linearly with increasing transverse deviation of the incident particle. The resulting force influences the transverse motion of the particle. For a dipole, shifts along the x- or y-axis do not have this effect since the equipotential lines of a dipole field are parallel to the x-axis.



(a)



(b)

Figure 5.8: Influence in horizontal (a) and vertical (b) direction of Gaussian distributed dipole displacements with increasing standard deviation. The mean  $RMS$  values are calculated according to the BPM readings and therefore represent the measurable orbit.

Dipole displacement, Fit parameters					
		$a_x$	$a_y$	$\chi^2/\text{ndf, x}$	$\chi^2/\text{ndf, y}$
BPMs	uncorrected	$0.664 \pm 0.026$	$0.724 \pm 0.025$	0.113/99	0.080/99
	corrected	$0.063 \pm 0.002$	$0.028 \pm 0.001$	0.094/99	0.095/99
all elements	uncorrected	$0.680 \pm 0.025$	$0.704 \pm 0.024$	0.109/99	0.080/99
	corrected	$0.131 \pm 0.003$	$0.052 \pm 0.002$	0.093/99	0.095/99

Table 3: Parameters of the linear fit to the mean *RMS* values resulting of dipole displacements. The subscript of the slope of the linear fits  $a$  indicates the considered transverse direction. The measurable values are indicated by *BPMs*, the parameters corresponding to the true *RMS* values are indicated by *all elements*.

### 5.1.4 Dipole rotation

Rotations of dipoles have different effects depending on the rotation axis. A rotation around the longitudinal direction, i.e. around the momentum direction of the particles, leads to a decreased vertical magnetic field and a non-vanishing field component in horizontal direction. Thus the beam is bend less in the horizontal plane and experiences a deviation in the vertical direction. Considering ideal quadrupole fields and positions, the change in horizontal bending leads to a different entering position in the quadrupoles which enhances the effect in x-direction. The field changes after a rotation about the longitudinal axis are illustrated in Figure 5.9.

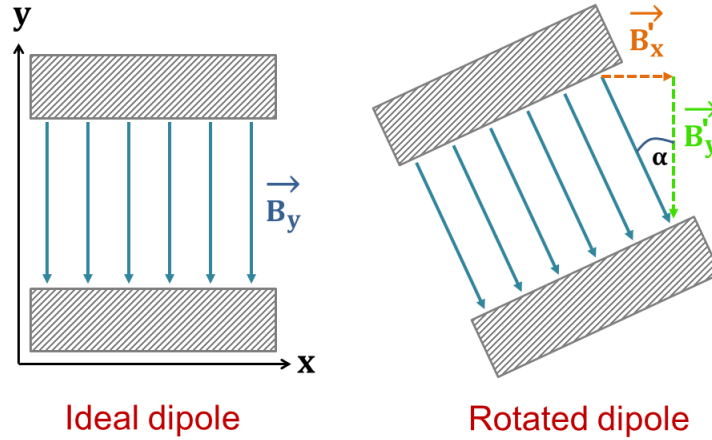


Figure 5.9: Dipole rotated around the longitudinal axis. The initially pure vertical magnetic field is now decreased and a non-vanishing horizontal field component appears.

It is easy to deduce that the resulting vertical (horizontal) field is proportional to  $\cos(\alpha)$  ( $\sin(\alpha)$ ):

$$B'_x = B_y \cdot \sin(\alpha) \approx B_y \cdot \alpha, \quad (5.4)$$

$$B'_y = B_y \cdot \cos(\alpha) \approx B_y \left(1 - \frac{\alpha^2}{2}\right). \quad (5.5)$$

For small angles, the field thus changes linearly with the rotation angle in x-direction and quadratically in vertical direction. Similar equations can be achieved for the rotation around the other axes. One therefore expects a quadratic change in the horizontal closed orbit *RMS* and a linear behavior in vertical direction.

After a rotation of a dipole about the horizontal axis, the resulting field has a smaller component in vertical direction and an additional non-vanishing field in longitudinal direction. This again leads to a weaker bending of the beam. The longitudinal field

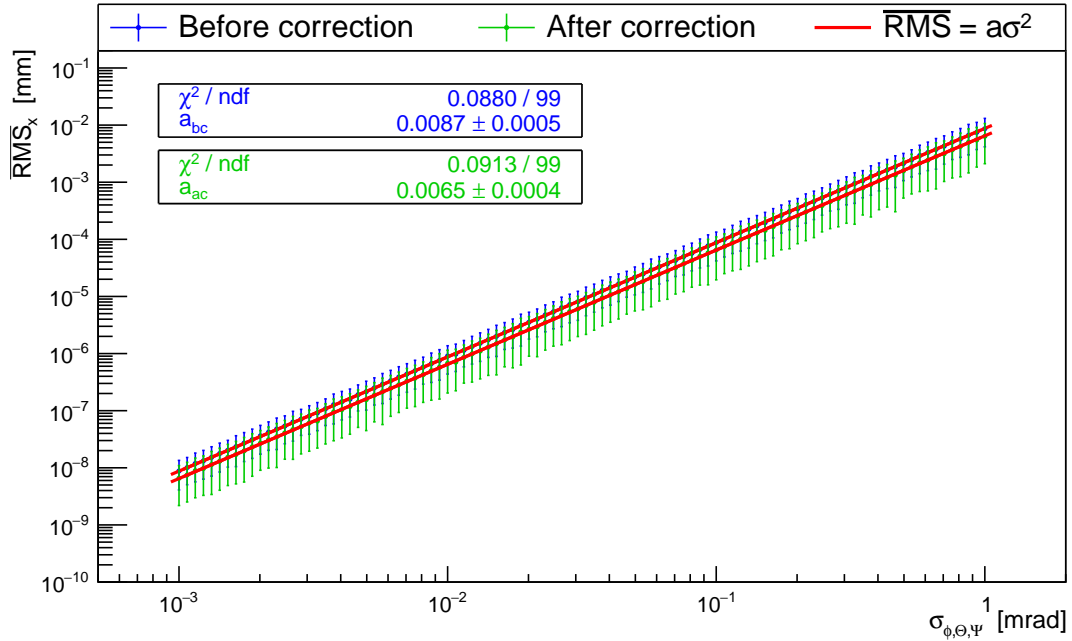
has no influence on the beam assuming all particle momenta point in the longitudinal direction (ideal beam). For momentum components in x- (y-) direction the longitudinal dipole field component leads to a particle motion in y- (x-) direction. These transverse momentum components are small compared to the longitudinal particle momenta and can usually be neglected.

A rotation of a dipole about the vertical axis does not lead to changed field components of the dipole field. Only the path of the beam through the magnet becomes somewhat longer which leads to a change in the horizontal bending and therefore to a change in the horizontal orbit.

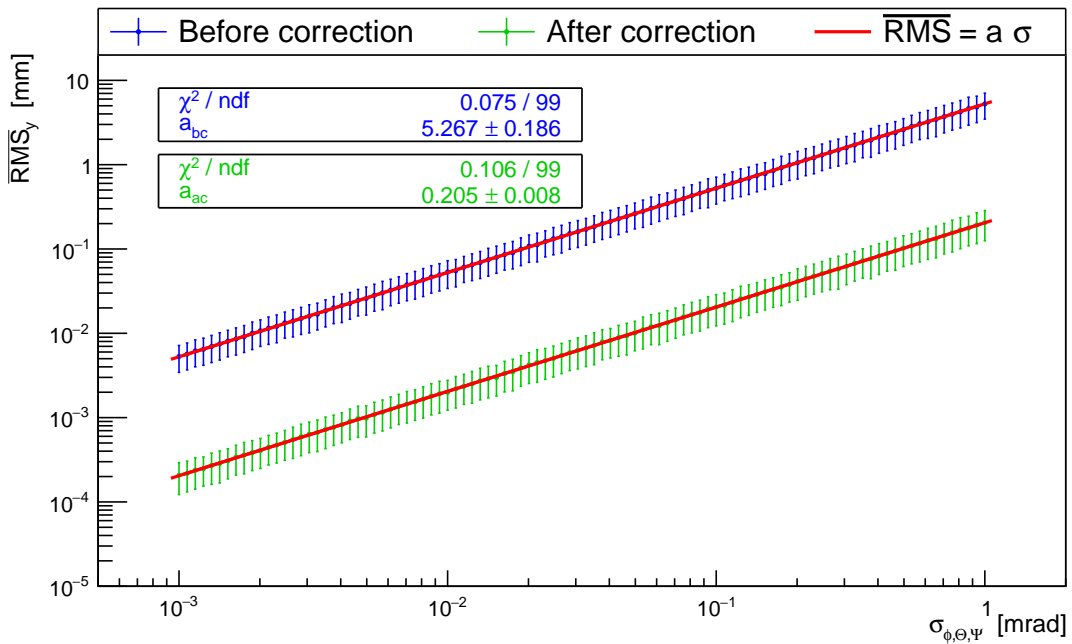
The random dipole rotation angles about every axis are Gaussian distributed with the same standard deviation but independent of each other. For each standard deviation 1000 random samples are generated to simulate the closed orbit and the change of its *RMS*. The results are shown in Figure 5.10 where a linear fit is performed in vertical direction and a quadratic function is fitted to the horizontal data. The quadratic dependence in horizontal direction cannot directly be seen due to the logarithmic axes but the quadratic fit and the corresponding small value of  $\chi^2/ndf$  indicate the validity of the assumption of a quadratic relation. The fit parameters for the linear fit in vertical direction and the quadratic fit for the x-direction are summarized in Table 4. As in former sections the realistic *RMS* calculation using only BPM values and the true *RMS* investigation considering all elements are distinguished. Similar to the linear fit function, the quadratic fit is performed such that the *RMS* is zero for vanishing standard deviation.

Dipole rotation, Fit parameters					
		$a_x$ [mm/mrad]	$a_y$ [mm/mrad]	$\chi^2/ndf, x$	$\chi^2/ndf, y$
BPMs	uncorrected	$0.0087 \pm 0.0005$	$5.267 \pm 0.186$	0.088/99	0.075/99
	corrected	$0.0065 \pm 0.0004$	$0.205 \pm 0.008$	0.091/99	0.106/99
all elements	uncorrected	$0.0088 \pm 0.0005$	$5.122 \pm 0.176$	0.088/99	0.078/99
	corrected	$0.0066 \pm 0.0005$	$0.380 \pm 0.013$	0.093/99	0.086/99

Table 4: Fit parameters of quadratic (linear) fits to the mean *RMS* values in horizontal (vertical) direction resulting of dipole rotations. The subscript of the fit parameter  $a$  indicates the considered transverse direction. The measurable values are indicated by *BPMs*, the parameters corresponding to the true *RMS* values are indicated by *all elements*.



(a)



(b)

Figure 5.10: Influence in horizontal (a) and vertical (b) direction of Gaussian distributed dipole rotations with increasing standard deviation. The mean  $RMS$  values are calculated according to the BPM readings and therefore represent the measurable orbit. The values in (a) show a quadratic behavior, the ones in (b) have a linear dependency.

## 5.2 BPM displacement

Even if the orbit in the machine was not distorted at all, measurements from displaced BPMs would lead to the illusion of an imperfect orbit. The orbit correction algorithm takes the BPM measurements as input and will provide magnet strengths for the corrector magnets. Switching on the magnets then will steer the beam and destroy its initially perfect trajectory. Simulating this effect, all elements in the simulation model are kept perfectly positioned, i.e. the beam passes the magnets in their centers. Then the BPMs are randomly displaced in the transverse direction using a Gaussian distribution assuming that the misalignments of one BPM are independent of other BPM displacements. For each standard deviation ten different sets of BPM displacements are generated. To find the mean *RMS* of the closed orbit, one has to average over these 10 random sample *RMS* values. Figure 5.11 (a) shows the results for the true orbit in horizontal direction. The orbit before applying any corrections is perfect and thus its *RMS* is equal to zero. After performing the orbit correction with respect to the displaced BPM measurements, the corrector magnets steer the beam away from the magnetic axes which leads to a non-vanishing *RMS* after orbit correction. As a result, the closed orbit quality is worse after the correction. Figure 5.11 (b) shows the values, that would have been measured by the BPMs in the horizontal plane. The corresponding results in vertical direction are given in Figure 5.12. Table 5 shows the parameters of the linear fits. The measured uncorrected orbit seems to be imperfect with a *RMS* unequal to zero. Therefore an orbit correction is applied as a plausible consequence. One can see that the effect of an orbit correction is quite small. The *RMS* values are not significantly decreased. This is due to the number and distribution of BPMs and corrector magnets at COSY. With a given setup of BPMs and correctors, the orbit correction algorithm can only reduce the closed orbit *RMS* to a minimum level depending on this setup. For a more efficient correction more BPMs and magnets are needed or an improved disposal of elements have to be found. Comparing the true with the measurable orbit after the orbit correction, it is apparent that the slopes are of the same order of magnitude. This can be explained by considering the readings at each BPM. As a representative example Figure 5.13 shows the BPM values for a fixed standard deviation and a fixed random seed. The wrongly measured BPM values before orbit corrections are given (green) and the true values after orbit correction are illustrated as well. The blue points represent the true orbit after correction, i.e. the measurements with perfect BPMs after orbit correction.

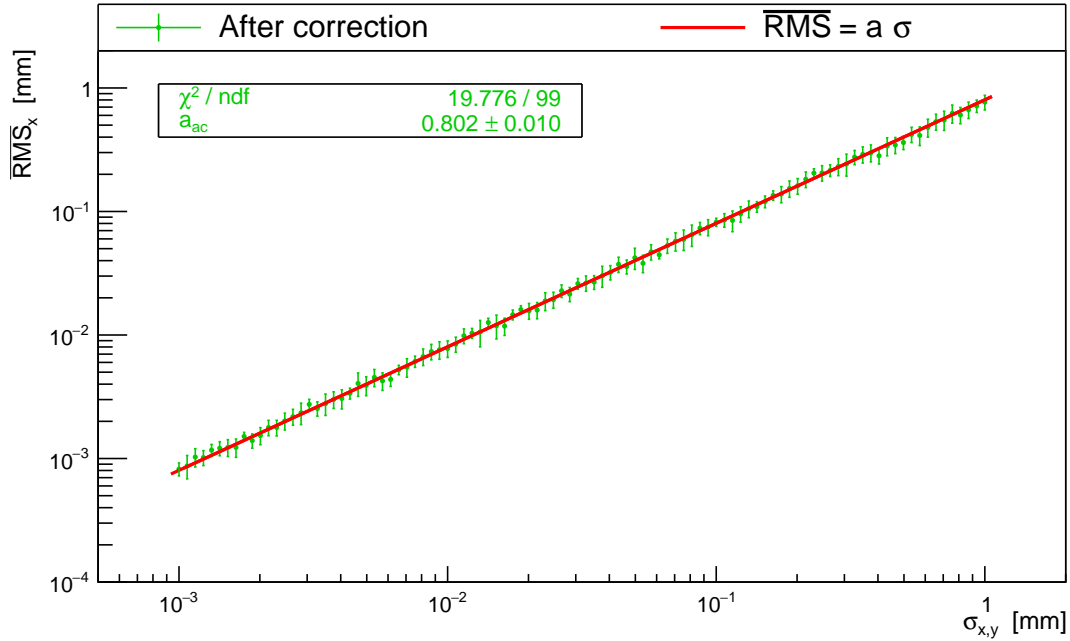
In the case of a non-distorted orbit and perfect BPMs, the BPM reading would always be zero. If the orbit deviates from the ideal path the perfect BPMs would measure the beam position correctly. Leaving the orbit at its ideal position and displacing the BPMs leads to the same result. Although the orbit is not deviating from the magnet centers, the BPMs measure deviations due to their shifted position. Not knowing that the BPMs are displaced from their ideal position, one suggests a distorted orbit based on the BPM readings. Performing an orbit correction with respect to the BPM readings and switching on the corrector magnets will distort the prior ideal orbit. The true closed orbit after the orbit correction is thus worse than before. Assuming a non-limited orbit correction, one expects that the BPM readings of ideal BPMs after the orbit corrections

BPM displacement, Fit parameters					
		$a_x$	$a_y$	$\chi^2/\text{ndf, x}$	$\chi^2/\text{ndf, y}$
True	uncorrected	0	0	0	0
	corrected	$0.802 \pm 0.010$	$0.773 \pm 0.011$	19.776/99	8.784/99
Measurable	uncorrected	$0.989 \pm 0.011$	$0.982 \pm 0.010$	13.994/99	13.017/99
	corrected	$0.570 \pm 0.011$	$0.590 \pm 0.010$	16.177/99	16.872/99

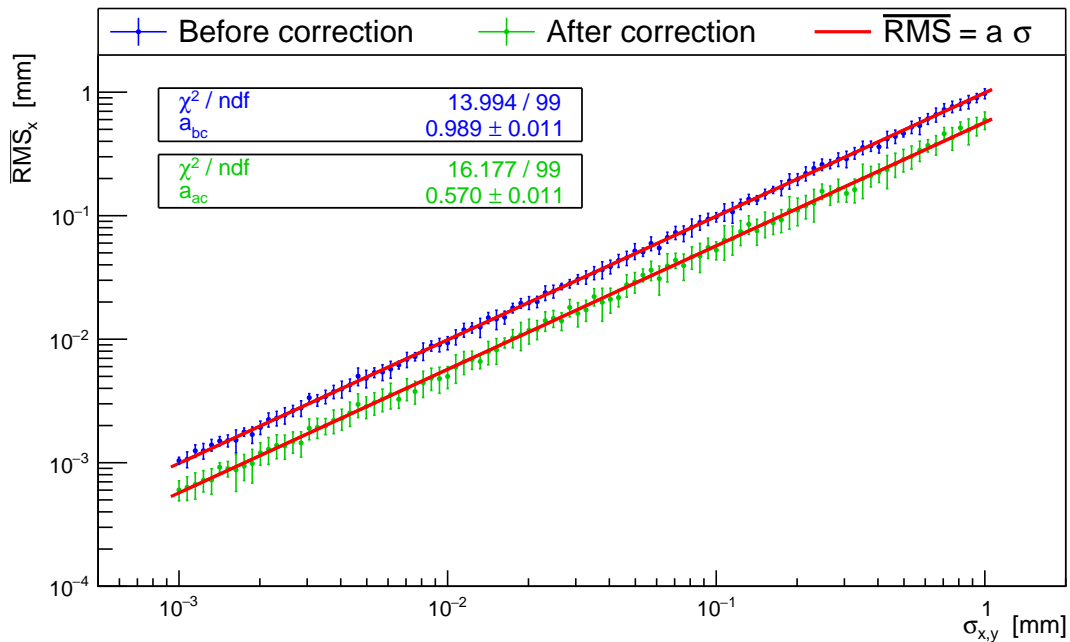
Table 5: Parameters of the linear fit to the mean *RMS* values resulting of BPM displacements. The subscript of the slope of the linear fits  $a$  indicates the considered transverse direction. The true values are indicated by *True*, the parameters corresponding to the measurable *RMS* values are indicated by *Measurable*. All values are calculated with respect to the BPM readings. For the true *RMS* values the BPMs are assumed to be perfectly positioned, the measurable values include the BPM displacements.

show the same values as the BPM readings of the displaced BPMs before applying the correction but with an opposite sign. The displaced BPMs would then measure an orbit deviation of zero, i.e. the orbit correction worked perfectly with respect to the displaced BPM readings which were used as an input for the correction algorithm.

As mentioned above the orbit correction is limited due to the number and positions of BPMs and corrector magnets and a perfect orbit correction to zero deviations is generally not possible. Therefore the absolute BPM readings of displaced BPMs before the orbit correction (green points in Figure 5.13) and the ones of ideal BPMs after the correction (blue points in Figure 5.13) differ. As a result, the measured orbit after correction at the displaced BPMs deviates from zero (red points in Figure 5.13). Especially the right half of the plot shows large deviations from zero and explains the non-vanishing *RMS*. Averaging over all random samples for each standard deviation then shows that the *RMS* of the corrected orbit with respect to the displaced BPMs is of the same order of magnitude as the true closed orbit *RMS* after correction.

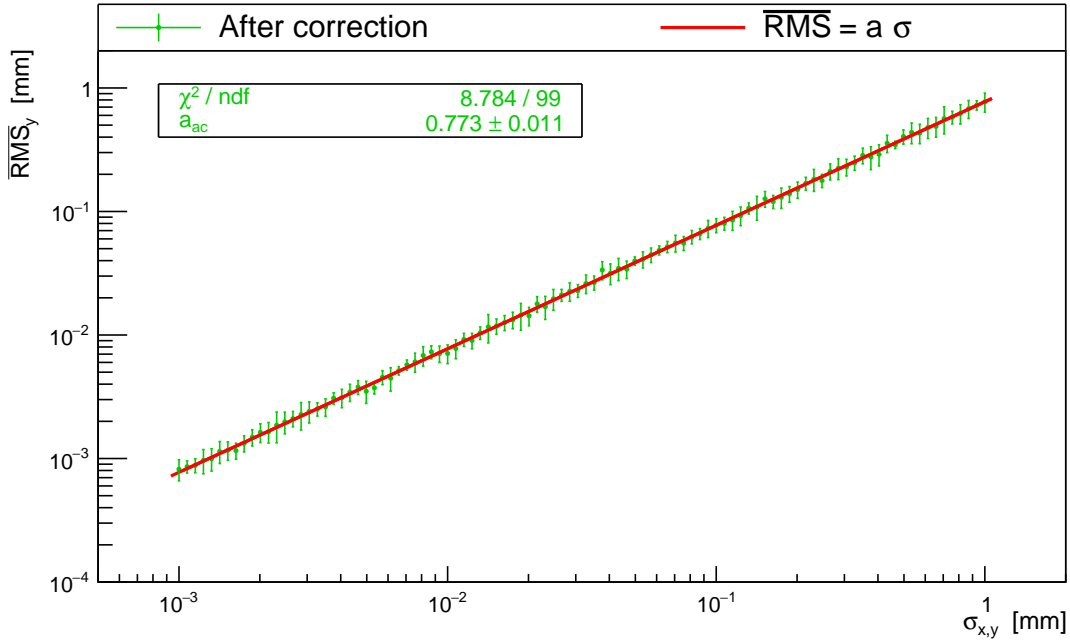


(a)

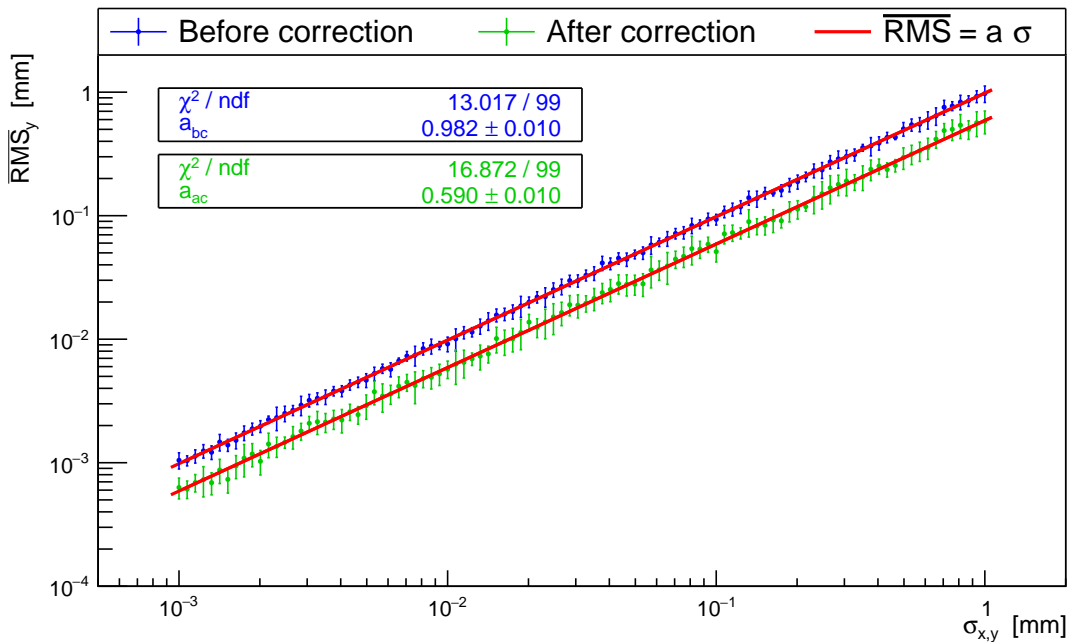


(b)

Figure 5.11: True (a) and measured (b) influence in horizontal direction of Gaussian distributed BPM displacements with increasing standard deviation. To (a): The true  $RMS$  value for the uncorrected closed orbit is equal to zero. The closed orbit  $RMS$  after correction deviates from zero since the corrector magnets are switched on. The mean  $RMS$  values are calculated with respect to the BPM readings ignoring the BPM displacements. To (b): The measured  $RMS$  value for the uncorrected closed orbit deviates from zero and leads to the illusion of an imperfect orbit. The mean  $RMS$  values are calculated with respect to the BPM readings including the BPM displacements.



(a)



(b)

Figure 5.12: True (a) and measured (b) influence in vertical direction of Gaussian distributed BPM displacements with increasing standard deviation. To (a): The true  $RMS$  value for the uncorrected closed orbit is equal to zero. The closed orbit  $RMS$  after correction deviates from zero since the corrector magnets are switched on. The mean  $RMS$  values are calculated with respect to the BPM readings ignoring the BPM displacements. To (b): The measured  $RMS$  value for the uncorrected closed orbit deviates from zero and leads to the illusion of an imperfect orbit. The mean  $RMS$  values are calculated with respect to the BPM readings including the BPM displacements.

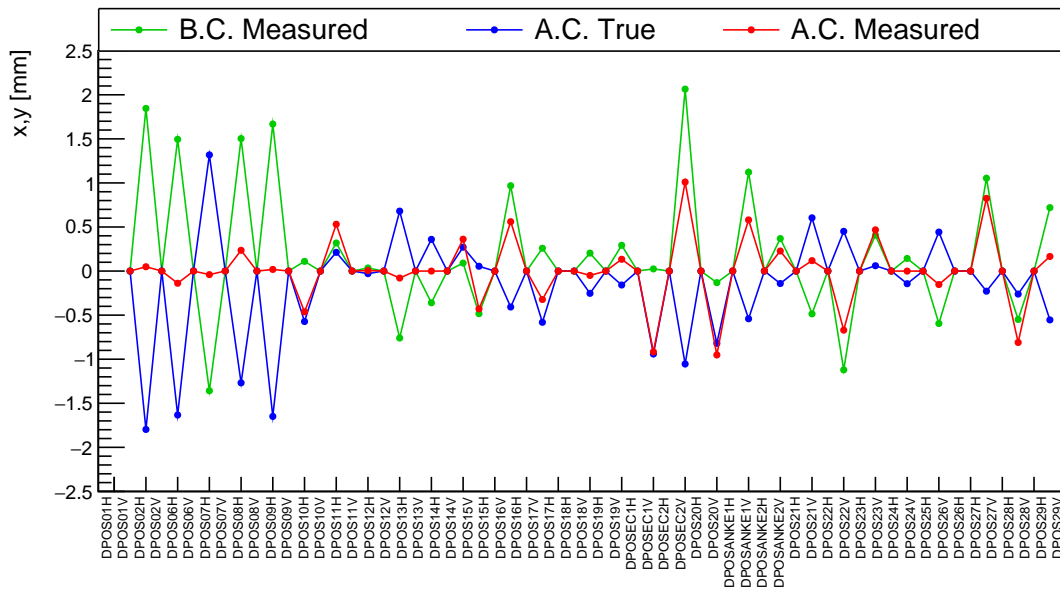


Figure 5.13: Comparison of the BPM displacement effect for perfectly positioned and displaced BPMs. The BPM readings of displaced BPMs are indicated by *Measured*. The label *True* represents BPM readings of perfectly positioned BPMs.

### 5.3 BPM resolution

Another limit on the orbit correction and thus on the final orbit quality is set by the resolution of the BPMs. As they cannot distinguish beam positions within the resolution limit, the lowest possible closed orbit *RMS* cannot lie below this limit.

#### 5.3.1 Constant resolution of 0.1 mm

For the first simulations a fixed value for the BPM resolution of 0.1 mm is assumed<sup>5</sup> which is independent of other misalignments. To estimate the effect on the closed orbit at COSY, the resolution limit is implemented as an additional misalignment on top of existing random dipole and quadrupole positioning and rotation errors. The standard deviation of positioning and rotation errors are always equal in one sample of misalignments. For each standard deviation of the magnet misalignments the corresponding measured value at each BPM is independently calculated by adding a random value to the true BPM measurement. The random number generation is performed according to a Gaussian distribution where the standard deviation indicates the resolution limit, i.e. in this case  $\sigma = 0.1$  mm. The new value that is measured at the BPM is then given by

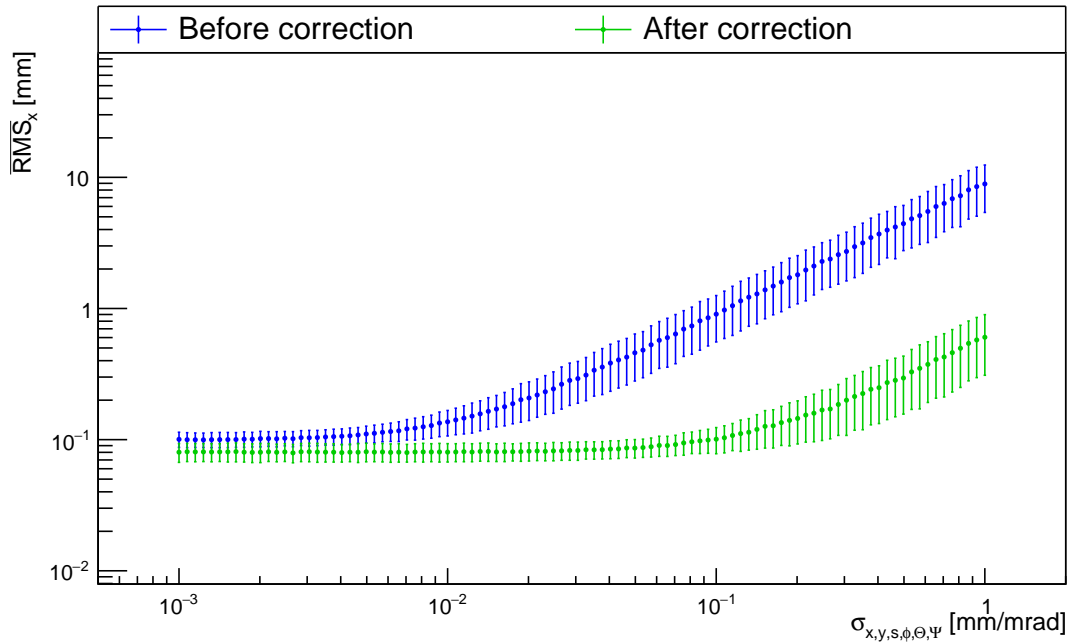
$$x_{\text{BPM}} = x_{\text{true}} + \text{Gauss}(0, \sigma_{\text{resolution}}), \quad (5.6)$$

with  $\sigma_{\text{resolution}}$  set to 0.1 mm. In total 1000 different random samples are generated for each standard deviation of magnet misalignments. The mean closed orbit *RMS* in each direction is calculated by averaging over these 1000 sample *RMS* values. The results for a fixed BPM resolution of 0.1 mm in both transverse directions are given in Figure 5.14. The *RMS* values are calculated with respect to the BPM readings.

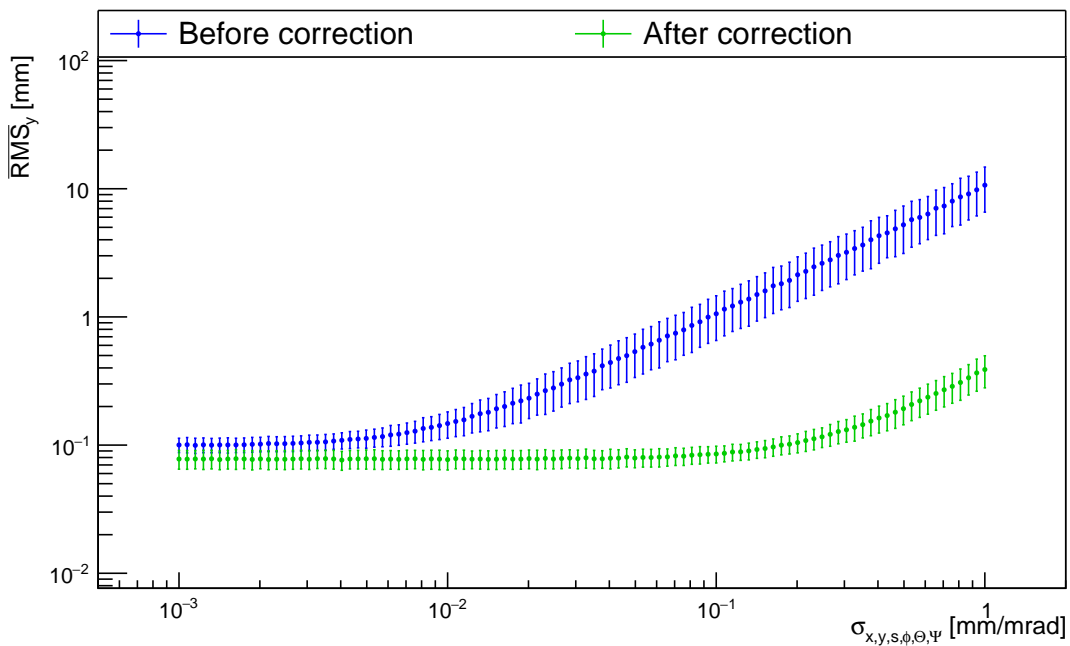
As expected, the restricted resolution inhibits a closed orbit measurement with an *RMS* below 0.1 mm. For standard deviations of the magnet misalignments below 0.1 mm this effect dominates the corrected orbit and thus limits the orbit correction efficiency. For standard deviations above 0.1 mm position and rotation errors of the magnets lead to a closed orbit *RMS* after orbit correction that is larger than the resolution limit anyway. Here the BPM resolution does not constrain the orbit correction significantly. The uncorrected closed orbit is only sensitive to resolution restrictions for standard deviations of the magnet misalignments smaller than  $10 \mu\text{m}$ . Considering the true *RMS* values which are calculated on the basis of the beam positions at all elements, the corrected closed orbit *RMS* increases in comparison to the *RMS* taken from the BPM values. Thus, the standard deviation at which the BPM resolution is dominated by magnet misalignments decreases by a factor of approximately five.

---

<sup>5</sup>Typical BPM resolution at COSY



(a)



(b)

Figure 5.14: Influence in horizontal (a) and vertical (b) direction of Gaussian distributed BPM resolutions with a constant standard deviation of 0.1 mm. The underlying reference lattice includes random dipole and quadrupole misalignments depicted on the x-axis. The mean  $RMS$  values are calculated according to the BPM readings and therefore represent the measurable orbit.

### 5.3.2 Running BPM resolution

In contrast to Section 5.3.1, the resolution of the BPMs is now assumed to be of the same order of magnitude as the misalignment errors of the magnets. As before, the new values read by the BPMs are calculated using Equation 5.6 but now the standard deviation in the resolution generation process is equal to the ones from the positioning and rotation generation process. The resolution thus increases as the position and rotation errors of the magnets increase. The resulting closed orbit *RMS* values after averaging over all iterations is shown in Figure 5.15 for the horizontal direction. The corresponding vertical results are given in Figure 5.16. In order to identify the net effect resulting from resolution constraints also the simulation results for ideal BPMs and combined dipole and quadrupole misalignments are shown. In Table 6 all fit parameters of the linear fits are summarized.

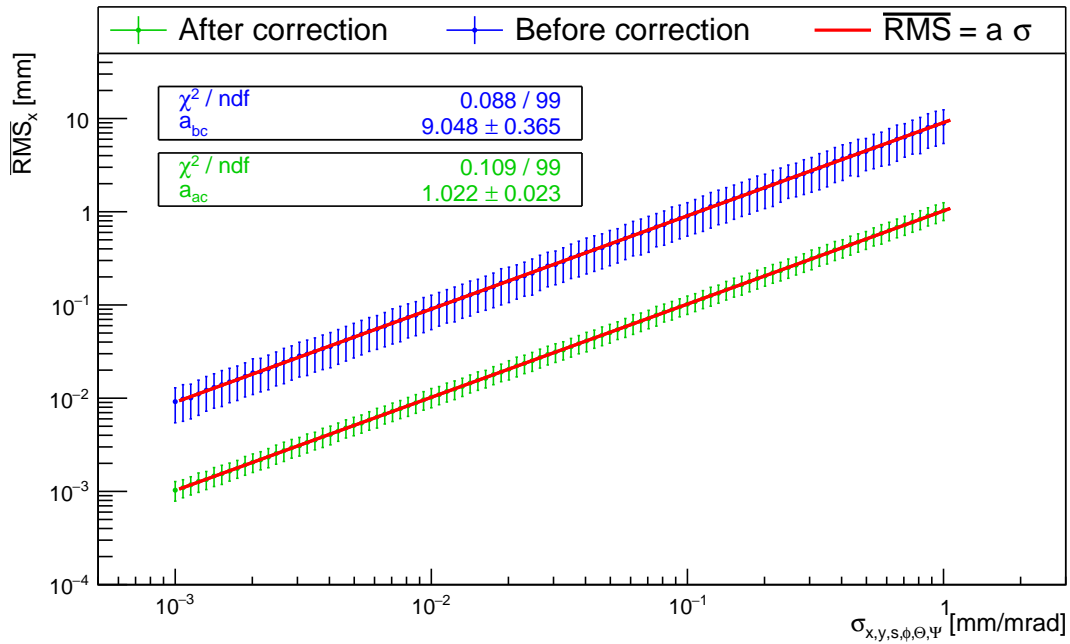
BPM with running resolution, Fit parameters					
		$a_x$	$a_y$	$\chi^2/\text{ndf, x}$	$\chi^2/\text{ndf, y}$
BPMs	uncorrected	$9.048 \pm 0.365$	$10.522 \pm 0.403$	0.088/99	0.085/99
	corrected	$1.022 \pm 0.023$	$0.955 \pm 0.013$	0.109/99	0.149/99
all elements	uncorrected	$9.233 \pm 0.360$	$10.237 \pm 0.377$	0.084/99	0.078/99
	corrected	$1.383 \pm 0.036$	$1.320 \pm 0.038$	0.095/99	0.091/99

Table 6: Parameters of the linear fit to the mean *RMS* values resulting of BPMs with running resolution. The subscript of the slope of the linear fits  $a$  indicates the considered transverse direction. The measurable values are indicated by *BPMs*, the parameters corresponding to the true *RMS* values are indicated by *all elements*.

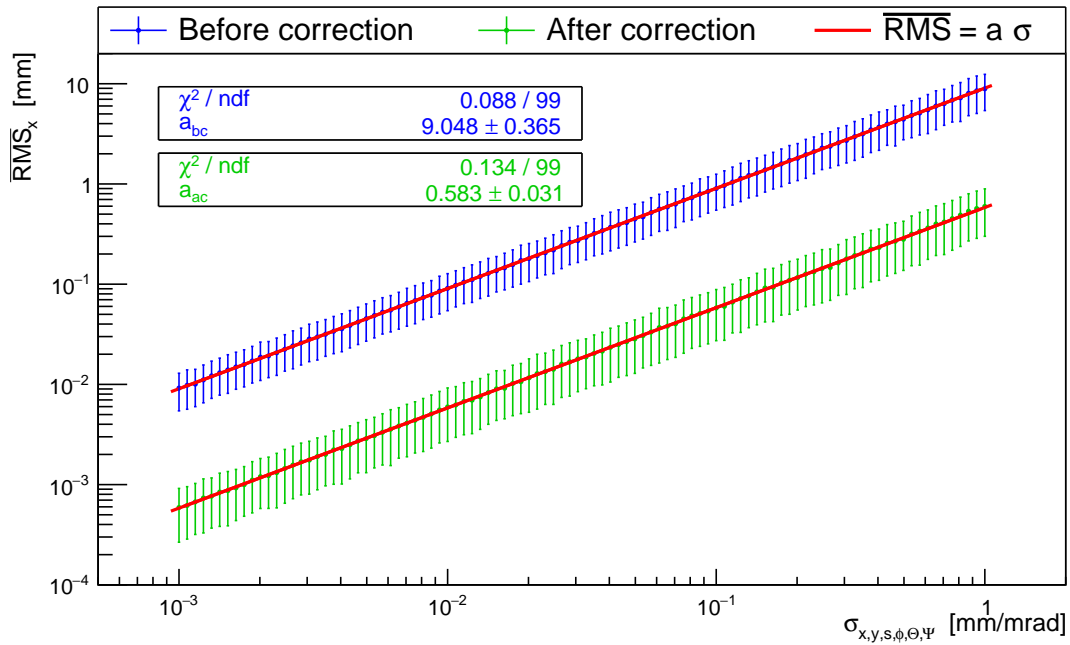
Dipole and quadrupole misalignments, Fit parameters					
		$a_x$	$a_y$	$\chi^2/\text{ndf, x}$	$\chi^2/\text{ndf, y}$
BPMs	uncorrected	$9.048 \pm 0.365$	$10.522 \pm 0.403$	0.088/99	0.085/99
	corrected	$0.583 \pm 0.031$	$0.341 \pm 0.011$	0.134/99	0.876/99
all elements	uncorrected	$9.233 \pm 0.360$	$10.237 \pm 0.377$	0.088/99	0.078/99
	corrected	$0.998 \pm 0.041$	$0.982 \pm 0.044$	0.101/99	0.094/99

Table 7: Parameters of the linear fit to the mean *RMS* values resulting of dipole and quadrupole misalignments including displacements and rotations. The subscript of the slope of the linear fits  $a$  indicates the considered transverse direction. The measurable values are indicated by *BPMs*, the parameters corresponding to the true *RMS* values are indicated by *all elements*.

One can easily see that the corrected orbit is influenced by the restricted resolution because the *RMS* value at every point equals the measurement limit of the BPMs given by the corresponding standard deviation. There is no significant effect on the uncorrected orbit since the position and rotation misalignments of the magnets dominate the process and the resulting *RMS* is larger than the resolution limit anyway. In order to extract the net effect of limited BPM resolutions, one must also consider the underlying dipole and quadrupole misalignments separately. Comparing the results in Table 6 to the results from combined dipole and quadrupole misalignments with ideal BPMs in Table 7 one can again see, that while the uncorrected orbits do not differ, the orbits after correction differ a lot. Due to the constraint BPM resolution the orbit cannot be corrected to a level lower than resolution level. A constraint BPM resolution thus indeed leads to a decrease in the corrected orbit quality.

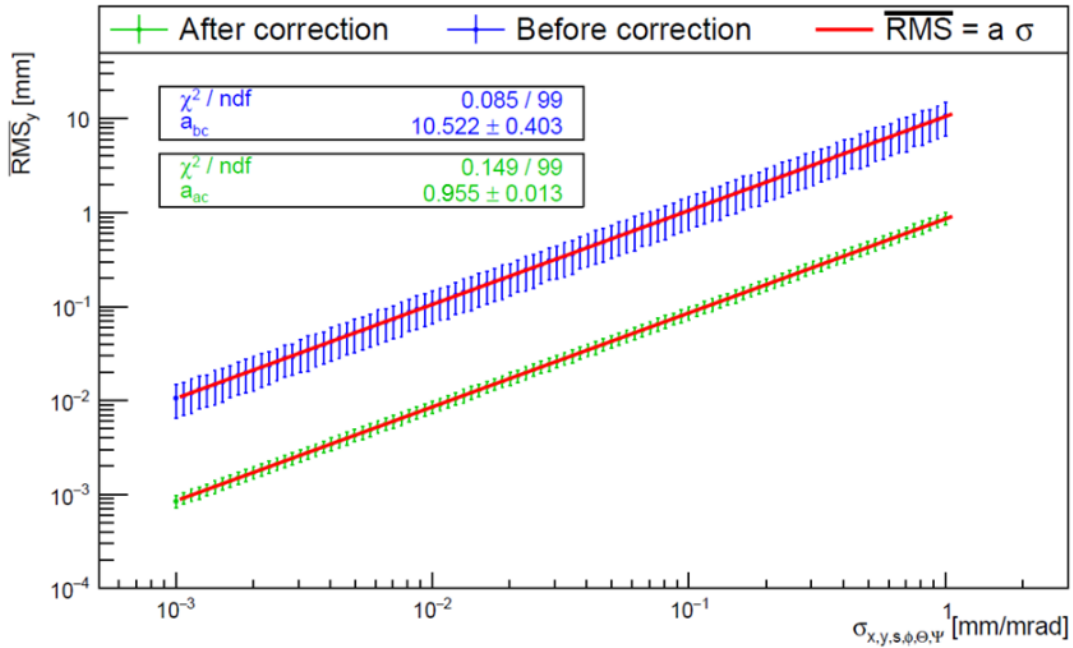


(a)

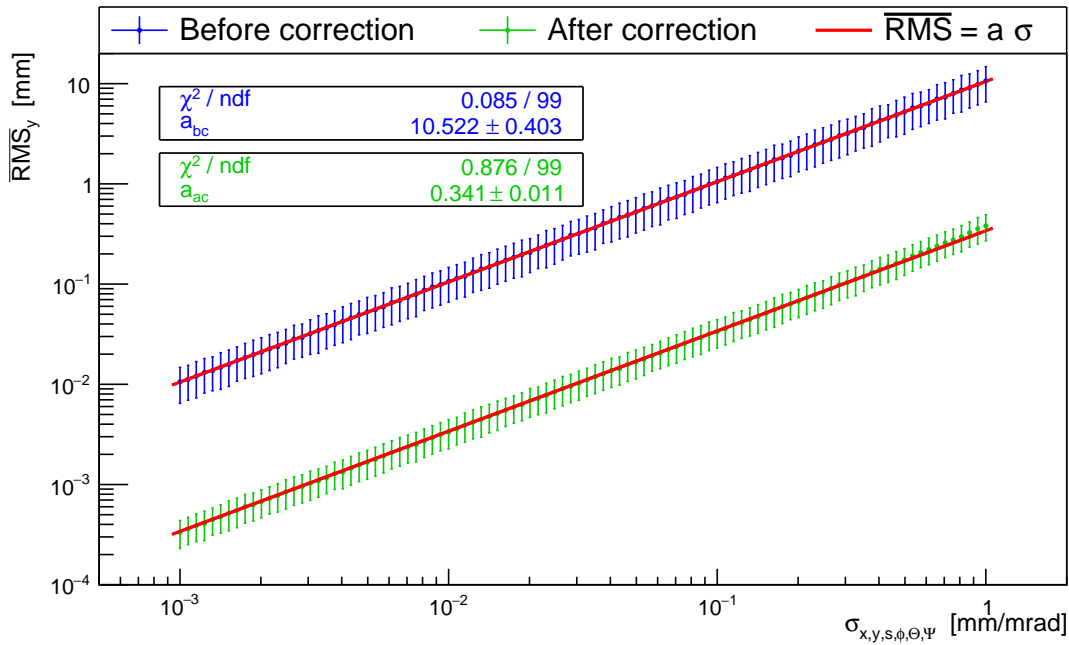


(b)

Figure 5.15: To (a): Influence in horizontal direction of Gaussian distributed BPM resolutions with a running standard deviation. The underlying reference lattice includes random dipole and quadrupole misalignments. The mean closed orbit  $RMS$  resulting of these misalignments assuming perfect BPMs is shown in (b). The mean  $RMS$  values are calculated according to the BPM readings and therefore represent the measurable orbit.



(a)



(b)

Figure 5.16: To (a): Influence in vertical direction of Gaussian distributed BPM resolutions with a running standard deviation. The underlying reference lattice includes random dipole and quadrupole misalignments. The mean closed orbit  $RMS$  resulting of these misalignments assuming perfect BPMs is shown in (b). The mean  $RMS$  values are calculated according to the BPM readings and therefore represent the measurable orbit.

## 5.4 Field instabilities

Until now, the fields provided by the magnets were assumed to be perfect. In the following the effect of varying dipole and quadrupole fields on the closed orbit are investigated. Given the current setup at COSY time dependent field changes cannot be corrected via the orbit correction method. The analysis of the simulations thus only includes uncorrected closed orbits. The simulation of field instabilities takes a fixed set of dipole and quadrupole displacement and rotations, defining the reference orbit. For each magnet family the set point of the provided field is then changed by adding a Gaussian distributed error with a mean of zero and a standard deviation set to a relative value  $X$  of the ideal field strength  $B_0$ :

$$B = B_0 + \text{Gauss}\left(0, \frac{X[\%]}{100} \cdot B_0\right). \quad (5.7)$$

After adding the field changes, the closed orbit is calculated. This process is repeated 1000 times. To analyze the effect of every random sample of field errors, the reference value at every BPM is subtracted from the new value at the BPM. The resulting deviations from the reference orbit are displayed in a histogram for each BPM and a Gaussian curve is fitted to the data. As an example, Figure 5.17 shows the distribution of deviations from the reference orbit at one BPM and the corresponding fit for the simulated field instabilities of dipoles. As expected, due to the way of error generation, the values are distributed around zero, i.e. the closed orbits including field instabilities of the dipoles vary around the reference orbit.

The width of the fit is taken as an indicator to quantify how much the field instabilities of the considered magnets change the *RMS* of the closed orbit at this specific BPM. To achieve a global value for the change of the closed orbit *RMS*, the average over all fit widths of the relevant BPMs is taken for a fixed relative error  $X$ . This means taking the BPMs, which measure in horizontal direction, into account for calculating the average *RMS* in x-direction and respectively the BPMs measuring in vertical direction for the value in y-direction. The whole process is then repeated for a different standard deviation of the Gaussian distributed field change.

### 5.4.1 Dipole field instabilities

Figure 5.18 shows the results for varying dipole fields in both directions. The errors are obtained by taking the uncertainties of the fit widths into account and performing an error propagation when averaging over the BPMs.

Since the ideal dipole fields are only pointing in the vertical direction, i.e. the beam is bend in the horizontal plane, it is not surprising, that the effect of field instabilities is larger in the horizontal plane. The contribution in the vertical direction is due to the misaligned magnets. For different dipole strengths the beam enters the quadrupoles at different transverse positions and the closed orbit changes also in vertical direction. For perfectly positioned elements this effect would vanish and merely an influence on the horizontal orbit would remain.

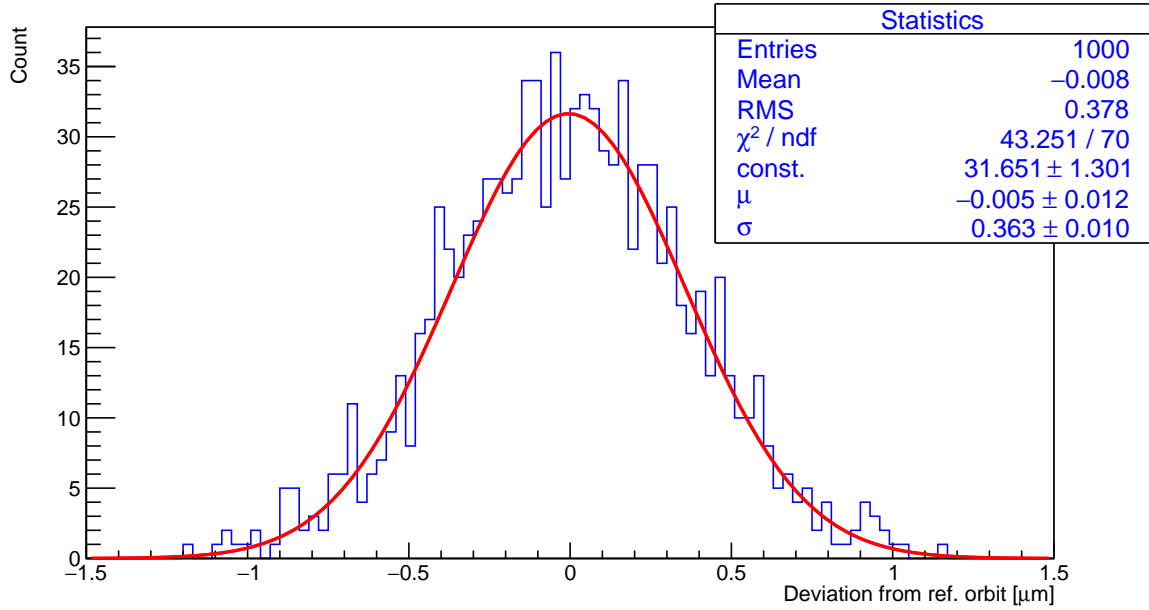
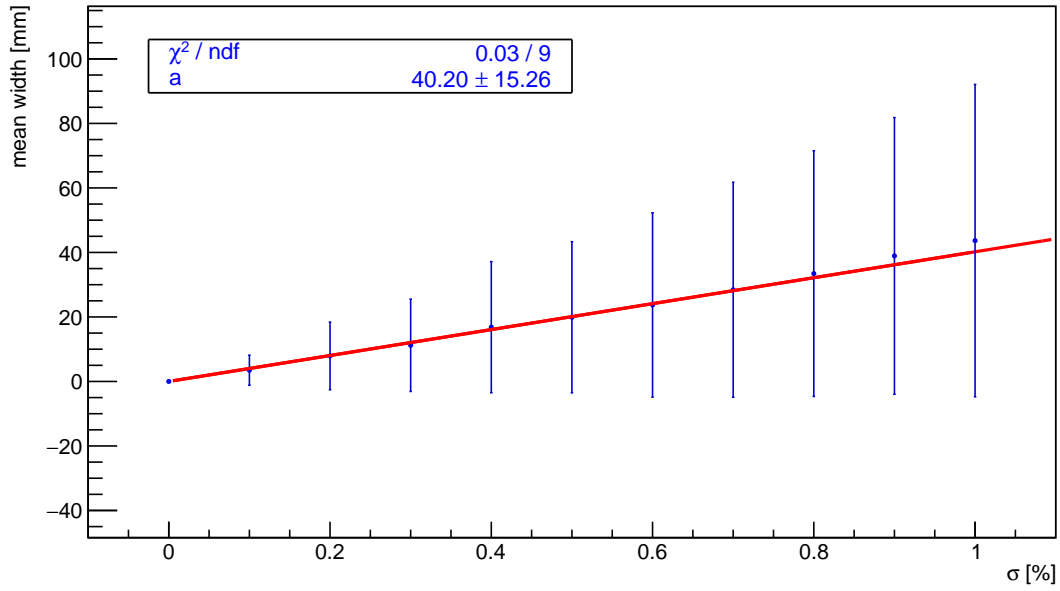


Figure 5.17: Exemplary histogram collecting BPM readings of all random samples at a specified BPM. The width of the Gaussian fit is used as an indicator of how much the field instabilities change the orbit at this BPM. Averaging over all fit widths leads to a global indicator value.

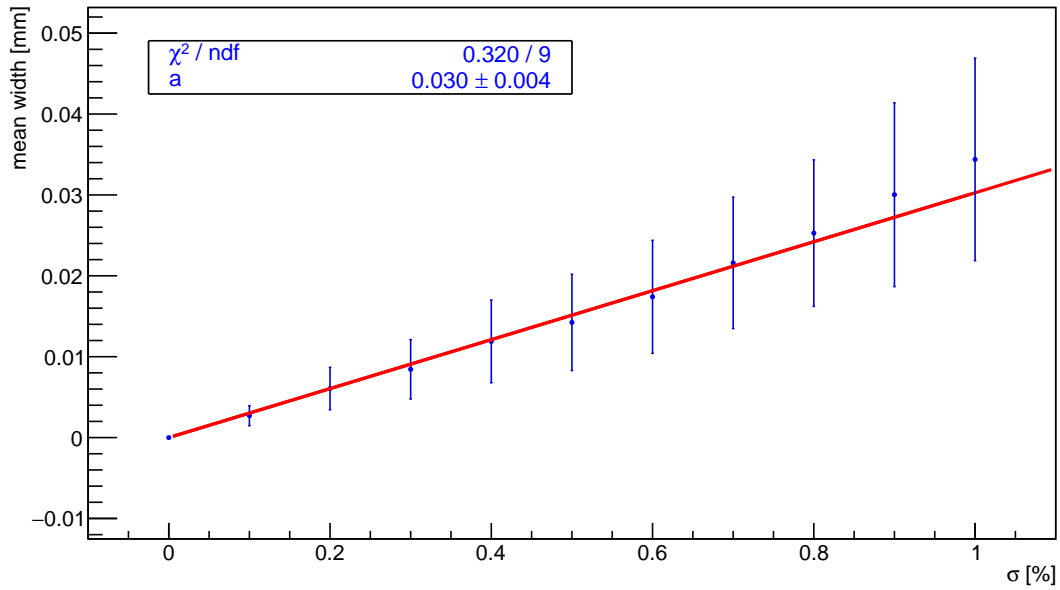
The slope  $a$  of the linear fit,

$$\overline{\text{RMS}} = a \cdot \sigma, \quad (5.8)$$

is a measure of the coupling between mean *RMS* change and the order of the field instability. The steeper the slope the more the orbit reacts to the changed fields. In Table 8 the slope values from both directions are summarized.



(a)



(b)

Figure 5.18: Influence in horizontal (a) and vertical (b) direction of Gaussian distributed dipole field instabilities. The mean width represents the change of the closed orbit *RMS*.

### 5.4.2 Quadrupole field instabilities

The dependency of the mean *RMS* on field instabilities in the quadrupoles are displayed in Figure 5.19 for both transverse directions.

As expected from the symmetries of a quadrupole field, the effect on the closed orbit is similar in the vertical and the horizontal plane. The parameters of both linear fits are given in Table 8. Comparing the effect of dipole field fluctuations to the influence of quadrupole field fluctuations for fixed  $\sigma$ , one can see a 200 times larger effect from the dipole field changes in the horizontal plane. In the vertical plane, the effect of quadrupoles exceeds the one of dipole fields by one order of magnitude.

Field instabilities, Fit parameters				
Magnet	$a_x$ [mm]	$a_y$ [mm]	$\chi^2/\text{ndf, x}$	$\chi^2/\text{ndf, y}$
Dipole	$40.20 \pm 15.26$	$0.030 \pm 0.004$	0.03/9	0.320/9
Quadrupole	$0.26 \pm 0.02$	$0.24 \pm 0.03$	0.54/9	0.57/9

Table 8: Parameters of the linear fits performed to the mean widths values due to field instabilities of dipoles and quadrupoles. The subscript of the slope of the linear fits  $a$  indicates the considered transverse direction.

Regarding the requirements for the precursor experiment at COSY, field instabilities would affect the closed orbit on a significant level if the resulting change of the transverse *RMS* is of the order of  $100 \mu\text{m}$ . In the case of dipole field changes this is the case for standard deviations of the randomized errors of  $\sigma > 2.5 \cdot 10^{-3} \%$ .

The quadrupole instabilities ought to be much larger than  $0.4\%$  to reach this level of change in *RMS*. In the next section one main source of field instabilities is investigated to estimate if there is a significantly large effect on the COSY orbit which has to be considered and reduced for the upcoming experiments.

## 5.5 Residual power supply oscillations

One main reason for field changes in the magnets are residual power supply oscillations which induce oscillating magnetic fields and cannot be controlled with an orbit control acting slower than the oscillation frequency of the power supplies. In the following a sinusoidal oscillation with a maximum amplitude of  $\frac{\Delta I_{max}}{2}$  is assumed as sketched in Figure 5.20.

Each power supply has a relative uncertainty on the provided current which determines the amplitude of the residual current oscillation. In Table 9 the uncertainties as well as the maximum possible current and the resulting peak-to-peak value  $\Delta I_{max}$  are given for each type of magnet that is installed at COSY [25]. The dependency of the magnet strength on the provided current is taken from Section 4.1.2 using Equations 4.11, 4.12, 4.18 and 4.22.

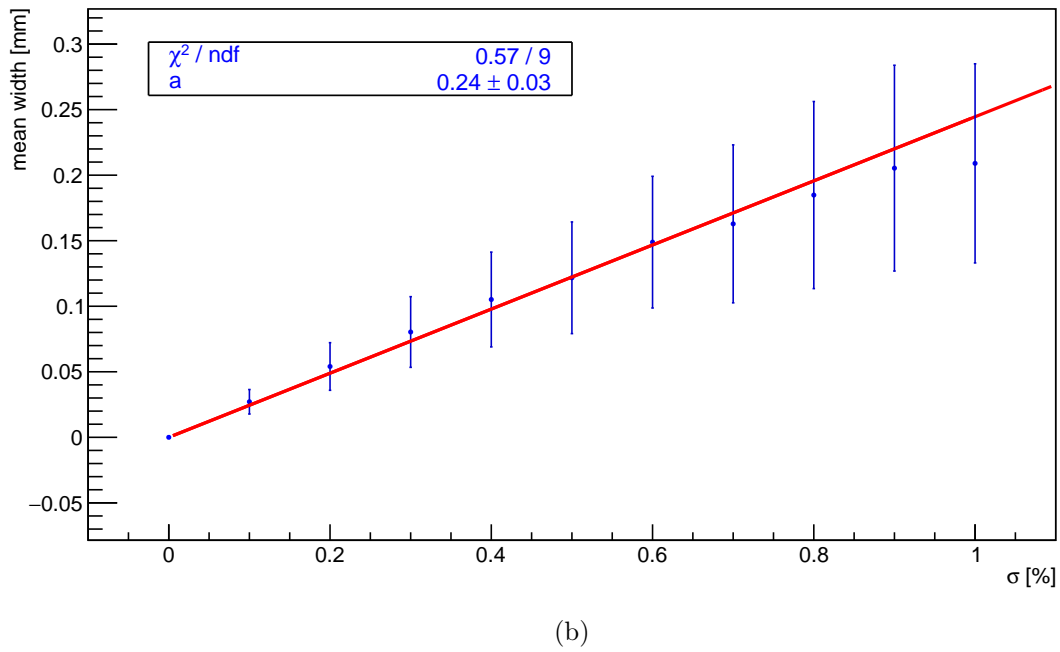
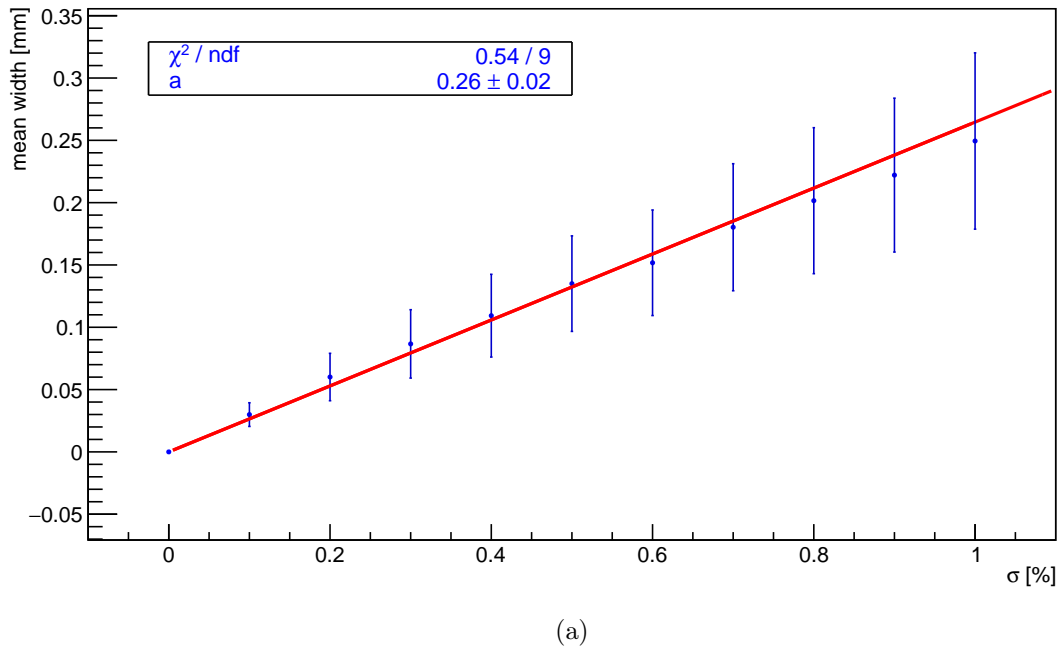


Figure 5.19: Influence in horizontal (a) and vertical (b) direction of Gaussian distributed quadrupole field instabilities. The mean width represents the change of the closed orbit *RMS*.

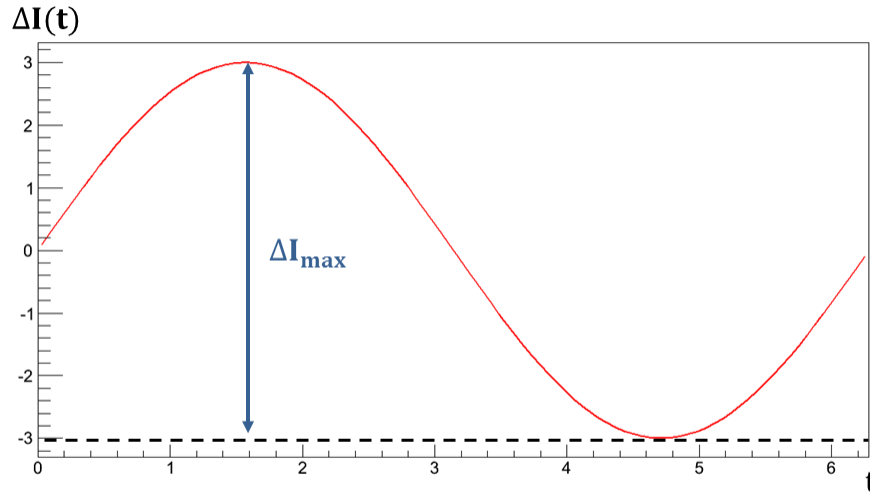


Figure 5.20: Sketch of sinusoidal residual power supply oscillation. The peak-to-peak value is called  $\Delta I_{\max}$ . The typical frequency of the power supply oscillation is approximately 600 Hz.

Independently of the magnet type, its strength depends linearly on the current. Thus one can easily deduce the oscillation of the magnet strengths given its variation of the current.

Relative error on the current of the COSY magnets			
Magnet	$\sigma$ [ppm]	max. current [A]	max. peak-to-peak value [A]
Dipole	20	5000	100
Quadrupole	20	550	11
Sextupole	500	275	137.5
Corrector	100	30	3

Table 9: Relative error and maximum current of COSY magnets.

To estimate the maximum effect of current oscillations, for each power supply an amplitude of the sine is randomly generated using a Gaussian distribution with the maximum possible amplitude, i.e. half of the peak-to-peak value in Table 9. Since the magnitude of the current change is time dependent, additionally a random phase of the sinusoidal field variation is generated uniformly.

The resulting value for the change in current is then given by

$$\Delta I = \text{Gauss}\left(0, \frac{\Delta I_{max}}{2}\right) \cdot \sin\left(\text{uniform}(0, 2\pi)\right). \quad (5.9)$$

Using the equations above, one can deduce the corresponding change in the magnet strength, incorporate them in the model and finally calculate the closed orbit for this set of field changes. One simulation thus results in a snapshot of the oscillation dynamics. By creating various of these snapshots one can investigate the average influence of power supply oscillations on the transverse orbit. In the following analysis 1000 snapshots, i.e. 1000 closed orbits calculations each for a different set of current values, are generated. As in Section 5.4 a reference orbit with a fixed set of misaligned dipoles and quadrupoles was chosen. To investigate the deviation from this reference orbit due to the incorporated field changes, the same method as in Section 5.4 is used. The deviations from the reference orbit at each BPM are collected in a histogram for all 1000 simulations and a Gaussian fit is performed. The width of the fit indicates the influence of the field oscillation at this specific BPM. Averaging over the widths of all Gaussian fits of the BPMs measuring in horizontal (vertical) direction indicates the influence on the closed orbit *RMS* in x- (y-) direction due to field changes caused by residual power supply oscillations. The results for every magnet type are summarized in Table 10. None of the *RMS* changes is of a larger order of magnitude than  $10 \mu\text{m}$ . Thus, regarding the precursor experiment at COSY, the residual power supply oscillations play a minor role when trying to improve the quality of the closed orbit to reach a transverse *RMS* of about  $100 \mu\text{m}$ . Since their effect is so small, they can neither explain the current measured orbits at COSY which give *RMS* values of the order of 1 mm. The effects of displaced and rotated magnets dominate the effect of power supply oscillations by many orders of magnitude.

Effect of residual power supply oscillations on the closed orbit <i>RMS</i>		
Magnet	$\Delta \overline{RMS}_x$	$\Delta \overline{RMS}_y$
Dipole	$(27.69 \pm 0.24) \mu\text{m}$	$(9.0 \pm 0.1) \text{ nm}$
Quadrupole	$(1.11 \pm 0.01) \mu\text{m}$	$(0.7 \pm 0.01) \mu\text{m}$
Sextupole	$(48.7 \pm 0.9) \text{ nm}$	$(49.9 \pm 0.6) \text{ nm}$
Corrector	$(34.43 \pm 0.30) \mu\text{m}$	$(28.07 \pm 0.22) \mu\text{m}$

Table 10: Influence of residual power supply oscillations of the COSY magnets in the closed orbit *RMS*.

Since the model only describes a linear machine in the case of active dipoles, quadrupoles and corrector magnets it is sufficient to perform the simulation for one fixed standard deviation in the Gaussian random generation process of amplitudes. Considering power supplies with a different relative error than in Table 9 one can easily scale the result to the new errors. Considering oscillations of sextupole power supplies, the machine is no longer linear, since now non-linear fields are incorporated. Even if the sextupole

strengths are set to zero<sup>6</sup> in the MAD-X basis model, the residual oscillations of their power supplies create small time dependent fields oscillating around zero. These fields then perturb the orbit. Since scaling in a non-linear machine is generally not possible, the simulation in case of sextupole field oscillations due to the power supplies have to be performed for various standard deviations of the randomized amplitudes. The result in Figure 5.21 shows how the influence of the sextupole power supplies on the average *RMS* of the closed orbit evolves for increasing standard deviation. Even if the machine is no longer linear, the *RMS* of the closed orbit increases almost linearly with increasing standard deviation. Thus for the considered relative power supply oscillations of zero to ten parts per million (ppm) non-linear effects seem to be negligible.

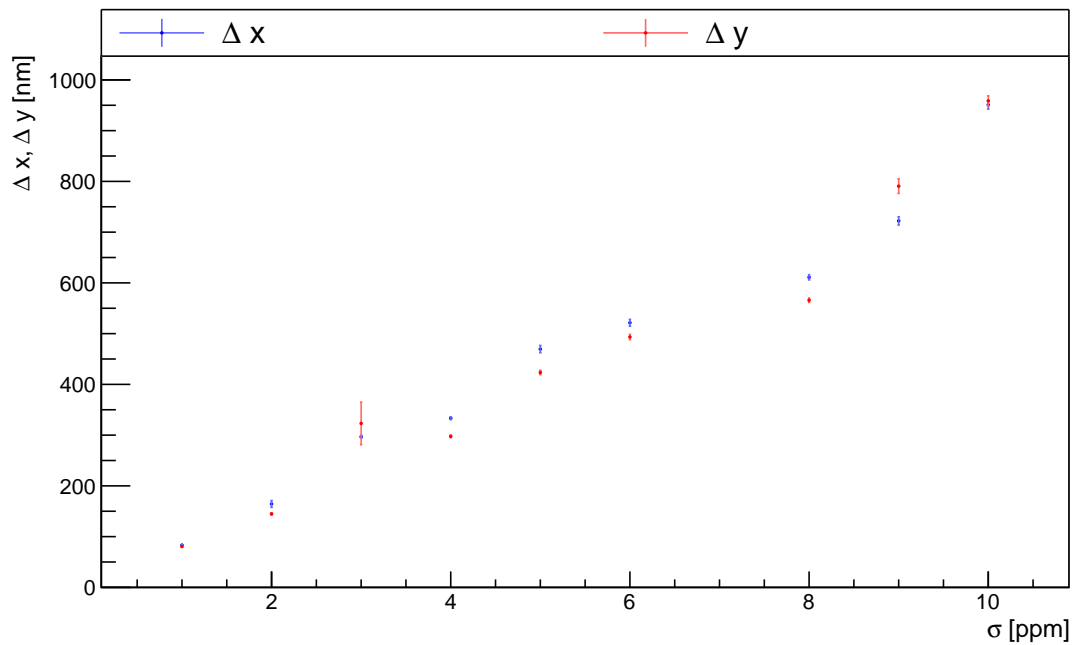


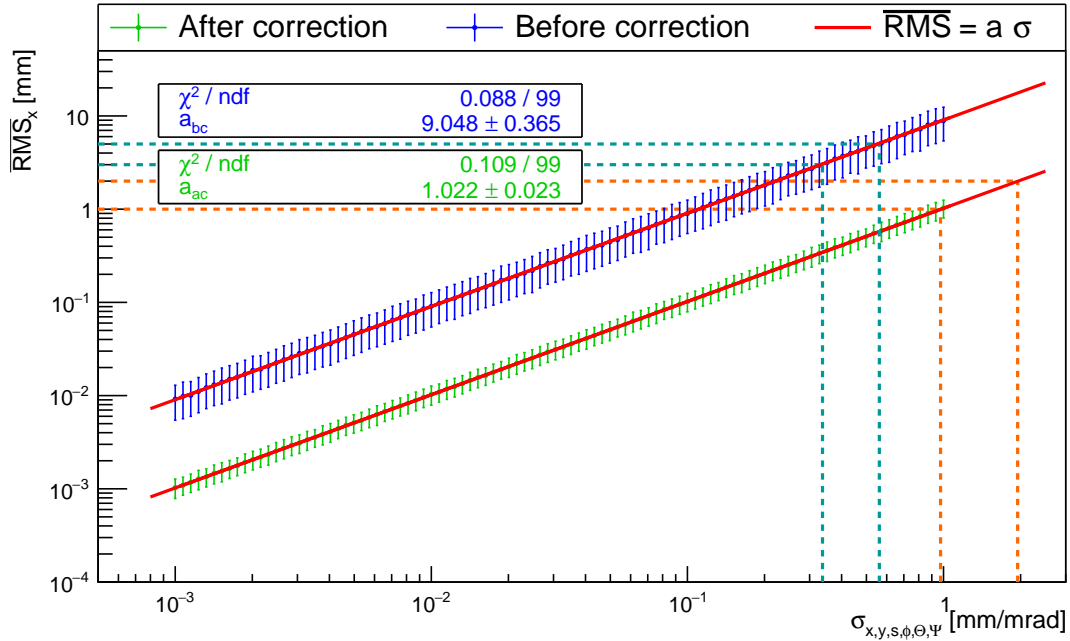
Figure 5.21: Influence of power supply oscillations of sextupoles on the closed orbit *RMS* as a function of standard deviation of the Gaussian randomized oscillation amplitude.

<sup>6</sup>This is the typical setup of the simulation model

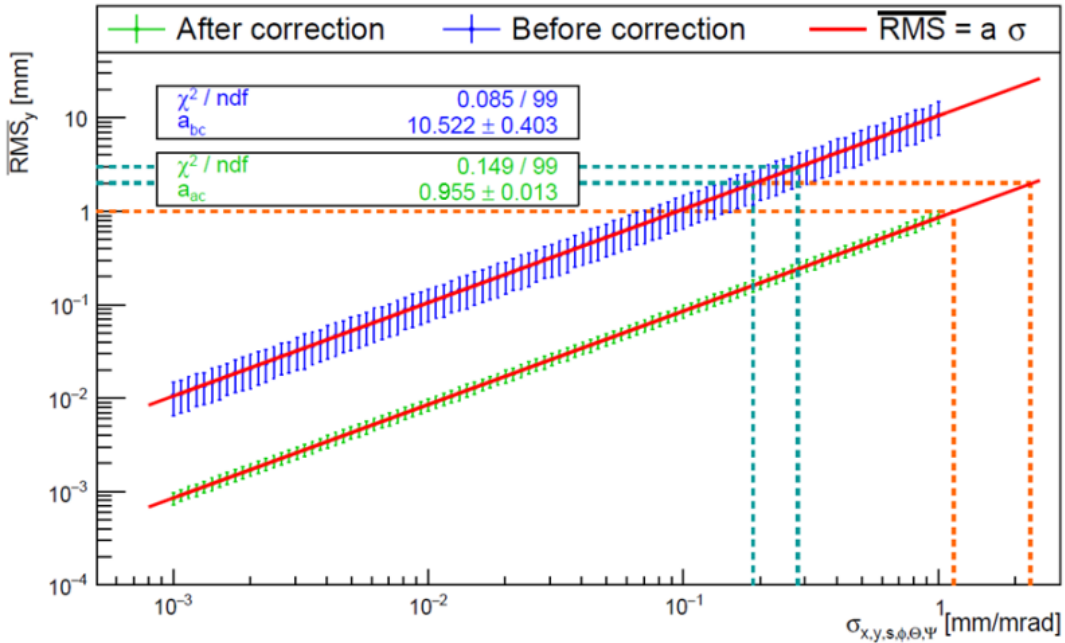
## 5.6 Comparison of simulation and measurement

A study of different effects that influence the closed orbit at COSY was performed to understand the measurement results and to estimate the main influences in order to control them in the future. From Section 5 it is known that the dominant effects are magnet misalignments and the resolution of the BPMs. Therefore the simulated orbit from these errors is now compared to the measured values at COSY. Figure 5.22 shows the simulation results if all magnet misalignments and a running BPM resolution are included. The dashed lines represent the interval in which the measured uncorrected and corrected closed orbit *RMS* values at COSY lie.

The projection of the measured COSY orbit values onto the x-axis (dashed lines) indicate the standard deviation range of the Gaussian distributed magnet misalignments. If the simulation includes all dominant effects, these ranges should overlap with the spread of the real magnet misalignments at COSY. From Figure 5.22 a range of 0.32 mm to 0.58 mm for the uncorrected orbit in x-direction and a range of 0.19 mm to 0.29 mm in y-direction can be deduced. For the corrected orbit these ranges shift to higher values and the resulting ranges become 1 mm to 2 mm for the x-direction and 1.2 mm to 2.2 mm in y-direction. Thus there is no overlap in the ranges of the uncorrected and corrected orbits. Since the simulations used the internal orbit correction of MAD-X there could be deviations from the real orbit correction implemented at COSY. Thus there may be additional effects influencing the orbit correction in the real machine operations which are not yet included in the MAD-X model. Therefore the results of the simulation for the uncorrected orbit are more reliable at this point. Assuming now that the magnet misalignments are Gaussian distributed and that they represent the dominant closed orbit influencing effect, the conclusion after comparing the measured COSY values with simulations then is that the COSY magnets are distributed with a standard deviation somewhere in the range between 0.19 mm to 0.58 mm.



(a)



(b)

Figure 5.22: Comparison of simulated and measured closed orbit in horizontal (a) and vertical (b) direction. The simulation results include dipole and quadrupole misalignments as well as running BPM resolution constraints. The dashed lines represent the ranges of measured closed orbit  $RMS$  values at COSY. The blue line corresponds to the uncorrected orbit, the orange one to the orbit measurements after correction. The projection of the measured  $RMS$  values at COSY onto the x-axis gives an estimate for the spread of the magnet misalignments at COSY.

## 5.7 Survey at COSY

The results of Section 5.1 show, that magnet misalignments are one of the main sources of closed orbit deviations at COSY. It is therefore necessary to determine the current positions of all dipoles and quadrupoles at COSY and to correct large displacement and rotation deviations from the target position. A corresponding survey was conducted in April 2016 by the external company *Stollenwerk* [26]. The dipoles and quadrupoles at COSY are armed with reference marks at which a laser-based position measurement according to a fixed reference point can be carried out. The positioning of these marks on the magnet is sketched in Figure 5.23.

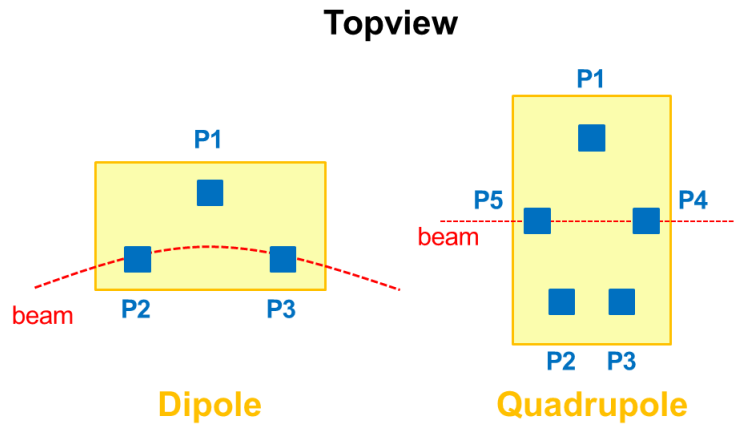


Figure 5.23: Topview on magnets: Reference marks on dipoles and quadrupoles. For dipoles the marks P2 and P3 are the closest to the beam path. In the case of a quadrupole, the marks P4 and P5 lie directly above the ideal beam trajectory through the magnet.

Taking the first dipole in the left arc in Figure 3.2 as the reference point, the relative vertical displacement of all other dipoles is measured. The same procedure is used for the quadrupoles, taking the first quadrupole after the injection point as the reference element. Given these information a best-fit-plane to which all elements afterwards should be optimally positioned was estimated. The best-fit-plane is found by taking the vertical measurement results and fitting a plane to the values which minimizes the vertical deviations. It turned out that taking only the reference marks P2 and P3 of the dipoles into account leads to the best result for the fitted plane. Ignoring some outliers of the measurement points further improves the result. Finally, the deviation of all magnets for the achieved best-fit-plane were calculated. Table 11 quantifies the amount of magnets lying in the vicinity of or deviate widely from the plane [27].

Figure 5.24 illustrates the deviations of dipoles and quadrupoles from the plane over the whole ring. Since the plane was determined using the dipole measurement points,

Vertical positioning of dipoles and quadrupoles relative to the best-fit-plane		
Deviation [mm]	Dipoles	Quadrupoles
$\Delta y \leq 0.2$	56 %	10 %
$0.2 < \Delta y \leq 0.5$	25 %	20 %
$0.5 < \Delta y \leq 1.5$	19 %	70 %

Table 11: Vertical deviations of the COSY magnets from the best-fit plane. The dipole values are taken from the reference marks P2 and P3, the vertical quadrupole position is given by P4 and P5 in Figure 5.23.

more than half of the dipoles lie within a deviation from the target plane of 0.2 mm which simultaneously represents the accuracy to which the magnets can be positioned. The quadrupoles show larger deviations. It is remarkable that the deviations of the quadrupoles show a systematic behavior (see Figure 5.24). In the arc sections they are positioned systematically to high, in the straight sections they are vertically positioned too low with respect to the best-fit plane. One explanation for the behavior in the straight sections is the adjustment procedure in these areas. To ensure a straight beam passing, elements within one straight section are positioned with respect to the first and last element in the section which define the straight line to which the other elements are adjusted. If the two reference elements are positioned too low, this also holds for all other elements in the straight section.

To calculate the horizontal and longitudinal deviation of every magnet from the best-fit plane, the measurement results of P1, P2 and P3 for the dipoles and the measurements of P4 and P5 for the quadrupoles were used. Figure 5.25 illustrates the process. In the case of dipoles, the three reference marks define the point, under which the beam passes in an ideal machine. The horizontal and longitudinal deviation from this point to its desired position then represents the dipole displacement in these directions. In order to determine the quadrupole deviation from the best-fit-plane, the reference marks P4 and P5 are used and their deviation from their desired position is calculated.

The provided data includes the horizontal and longitudinal deviation of the dipoles and additionally the vertical position of the reference marks P1, P2 and P3. The vertical deviation of the dipoles is given by the vertical measurement point of P2. Given the information about P1 and P3 one can calculate the rotation angle about the x-axis (s-axis) using the difference P3-P2 (P2-P1). The provided data in case of the quadrupoles includes the measurement points of P4 and P5 in every direction. The value of P5 in each direction defines the magnet displacement in this direction. The rotation angle about the x-axis (y-axis) can be calculated using the value of P4-P5 in vertical (horizontal) direction. Since not all measurements for all reference marks are provided, the remaining two rotation angles for dipoles (about y-axis) and quadrupoles (about s-axis) cannot be calculated and are set to zero.

Implementing the measured magnet misalignments into the COSY model in MAD-X and considering perfect BPMs leads to closed orbits shown in Figure 5.26. The *RMS* values are calculated with respect to the BPM readings.

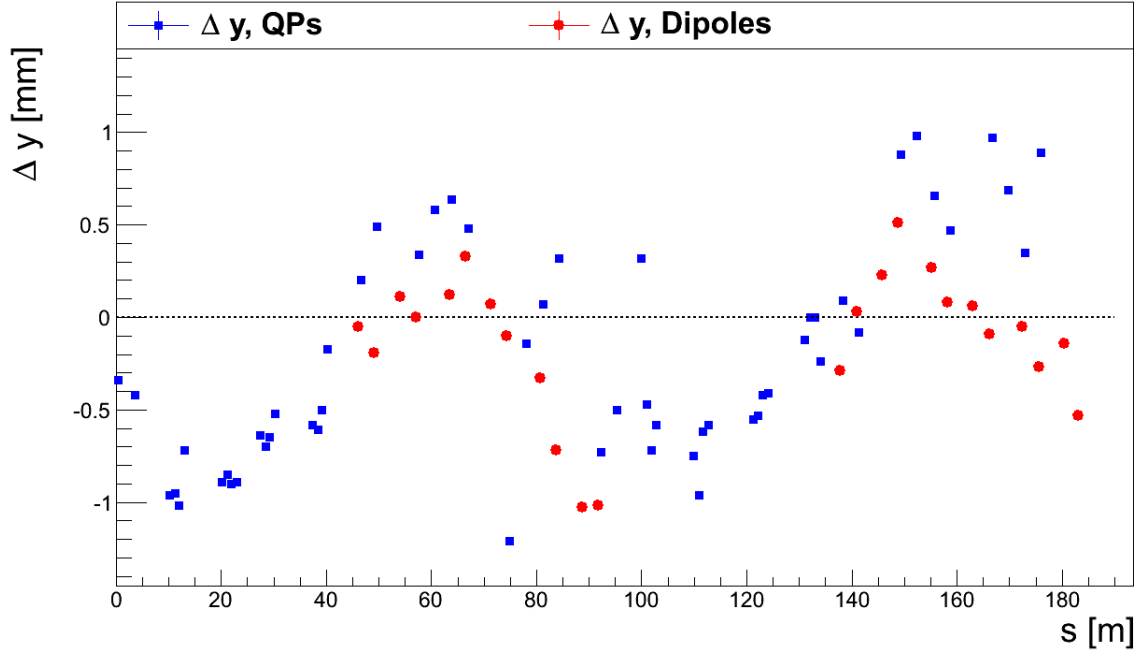


Figure 5.24: Vertical deviations from the best-fit-plane resulting of the survey which was performed in April 2016 at COSY [27]. The red points represent the vertical dipole deviations from the calculated plane. The blue points denote the vertical quadrupole deviations.

The corresponding values when taking all elements into account are given in Table 12. The uncorrected closed orbit *RMS* values are similar to the ones that are measured at COSY. The corrected values are one order of magnitude smaller than at the real machine. This is due to the assumption of perfect BPMs and as already mentioned in Section 5.6 the internal MAD-X orbit correction does not include all effects that influence the orbit correction. Since the BPMs at COSY do not have any reference marks, their position with respect to the magnets is unknown and large displacements are possible, leading to false measurements and thus additionally influencing the efficiency of the orbit correction. A beam based alignment would give information about the positions of the BPMS with respect to the nearby quadrupoles.

In all previous simulations magnet misalignments were assumed to be Gaussian distributed. In order to investigate the validity of this assumption the distributions of the magnet deviations from the best-fit-plane are shown in Figures 5.27 and 5.28. Only a few of the distributions show a Gaussian behavior. The remaining distributions cannot be described with a plausible function and thus the *RMS* of the values represents the spread of the values. Table 13 summarizes the *RMS* for all misalignment distributions. If a Gaussian fit could be performed, its width is taken as an indicator for the distribution spread instead.

Comparing the values in Table 13 with the conclusion of Section 5.6 almost all spread values lie in the suggested range of 0.19 mm to 0.58 mm. The suggestions deduced from the simulation results are thus consistent with the measured values at COSY.

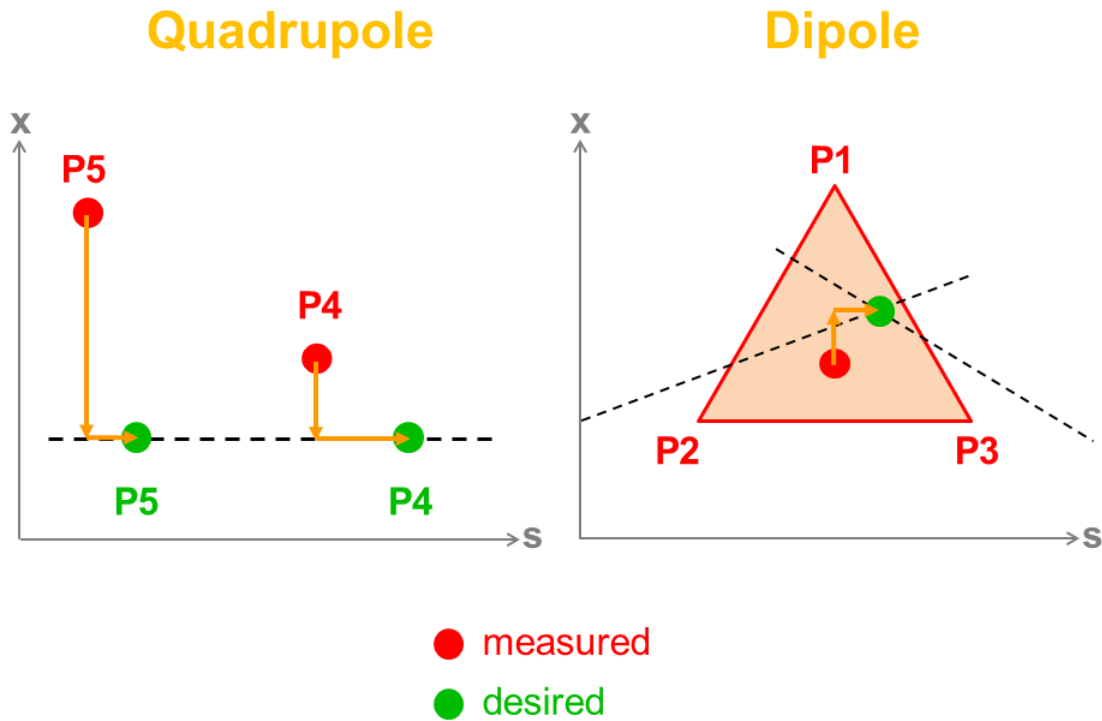


Figure 5.25: Determination of horizontal and longitudinal dipole and quadrupole deviations from the best-fit-plane. In the case of a dipole, the three reference marks determine the position of the dipole. For the quadrupole deviations the measured position of the reference marks P4 and P5 and their deviation from the desired positions determine the quadrupole displacement.

Misalignments from survey				
	$RMS_x$ [mm]		$RMS_y$ [mm]	
	Before correction	After correction	Before correction	After correction
BPMs	4.55	0.29	4.47	0.17
All	4.67	0.45	4.21	0.26

Table 12: Resulting  $RMS$  values when implementing the measured magnet misalignments of the survey at COSY in the MAD-X model. The values are calculated on the one hand with respect to only the BPM readings and on the other hand with respect to the beam position at all elements.

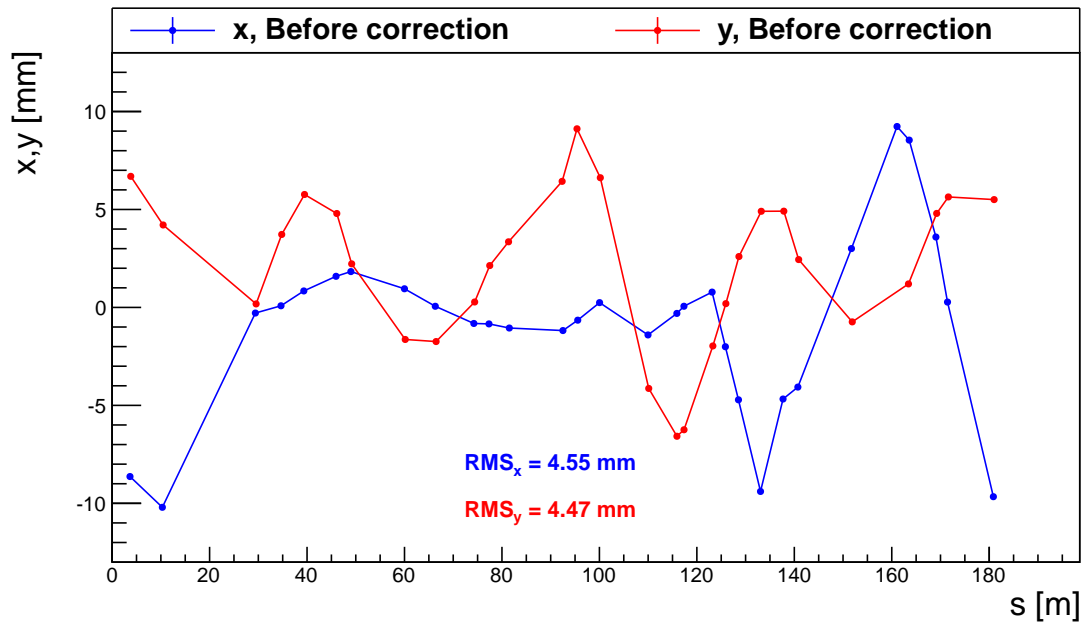
With the given survey data one can test whether the assumption of Gaussian distributed magnet misalignments and the resulting simulations are compatible with the simulation results using the measured misalignments.

Distribution spread of magnet misalignments at COSY					
	Dipoles				
	$\Delta x$ [mm]	$\Delta y$ [mm]	$\Delta s$ [mm]	$\Delta\phi$ [mrad]	$\Delta\Psi$ [mrad]
RMS	0.59	0.37	0.38	0.13	-
Fit, $\sigma$	-	-	-	-	0.29
	Quadrupoles				
	$\Delta x$ [mm]	$\Delta y$ [mm]	$\Delta s$ [mm]	$\Delta\phi$ [mrad]	$\Delta\Theta$ [mrad]
RMS	-	-	0.59	-	-
Fit, $\sigma$	1.79	0.44	-	0.49	0.22

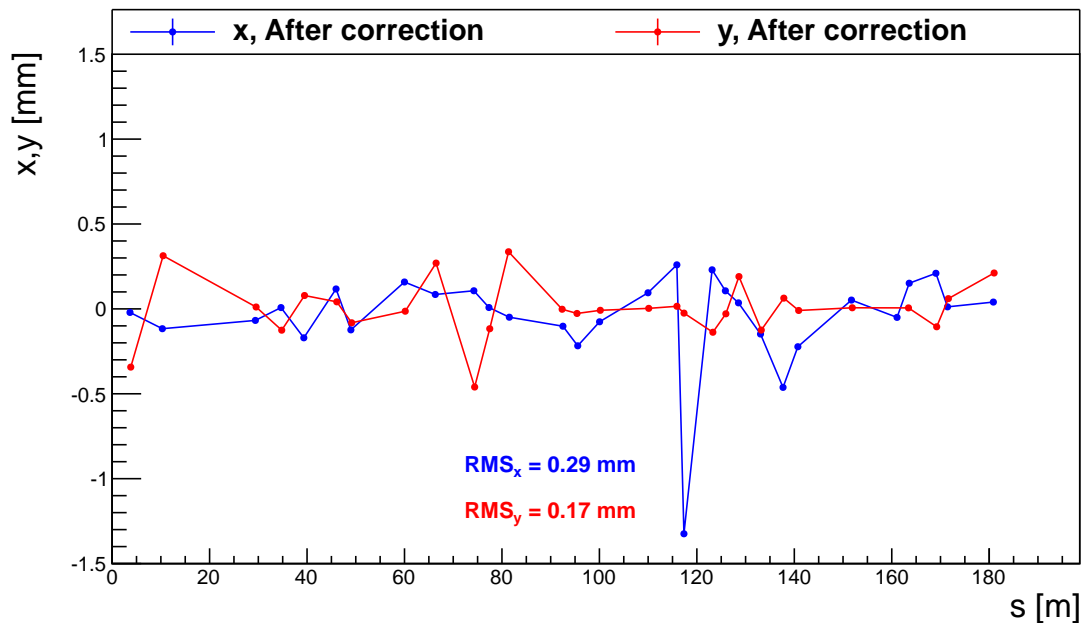
Table 13: Distribution spread of measured magnet misalignments. For distributions with no obvious underlying function the *RMS* of all values is taken as the distribution spread. If a Gaussian fit is plausible, its width is taken as the distribution spread instead.

Figure 5.29 shows the simulation result of Gaussian distributed magnet displacements and rotations for different standard deviations. The dashed lines represent the closed orbit *RMS* from the simulations including the survey data misalignments before and after the orbit correction. If the projections of these two lines onto the x-axis coincide, the simulation with Gaussian distributed misalignments can fully reproduce the simulation result using the measured misalignments.

In the horizontal direction the projection of the two dashed lines fully overlaps and thus the assumption of Gaussian distributed misalignments is reasonable. Although the projections onto the x-axis in the case of the vertical direction do not fully coincide the simulation results under the assumption of Gaussian misalignments nevertheless describes the real COSY data well since the gap between the two projections is quite small.



(a)



(b)

Figure 5.26: Simulated closed orbit before (a) and after (b) an orbit correction resulting from magnet misalignments taken from the survey data. The closed orbit  $RMS$  in the uncorrected case is similar to measured  $RMS$  values at COSY. Also the whole pathway of the uncorrected closed orbits show similarities to the measured orbits. The  $RMS$  values of the simulated corrected orbit are much smaller than the measured values at COSY since the simulation only includes misaligned magnets and no restrictions on the BPM quality.

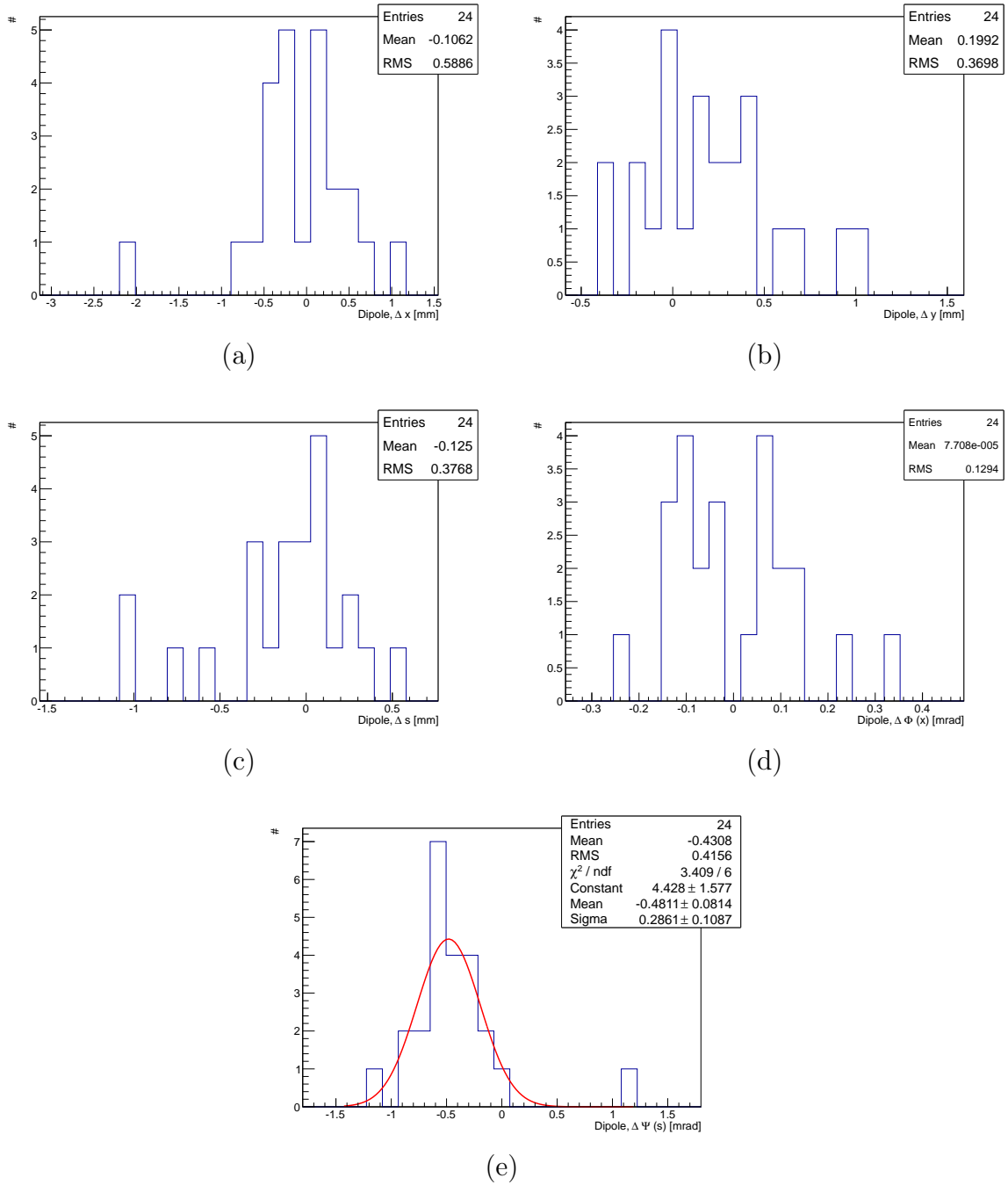


Figure 5.27: Distribution of dipole misalignments. In Figure (a) the horizontal deviations are collected. Figure (b) and (c) show the distributions for the vertical and longitudinal direction and (d) and (e) display the rotation angles around the x- and s-axis.

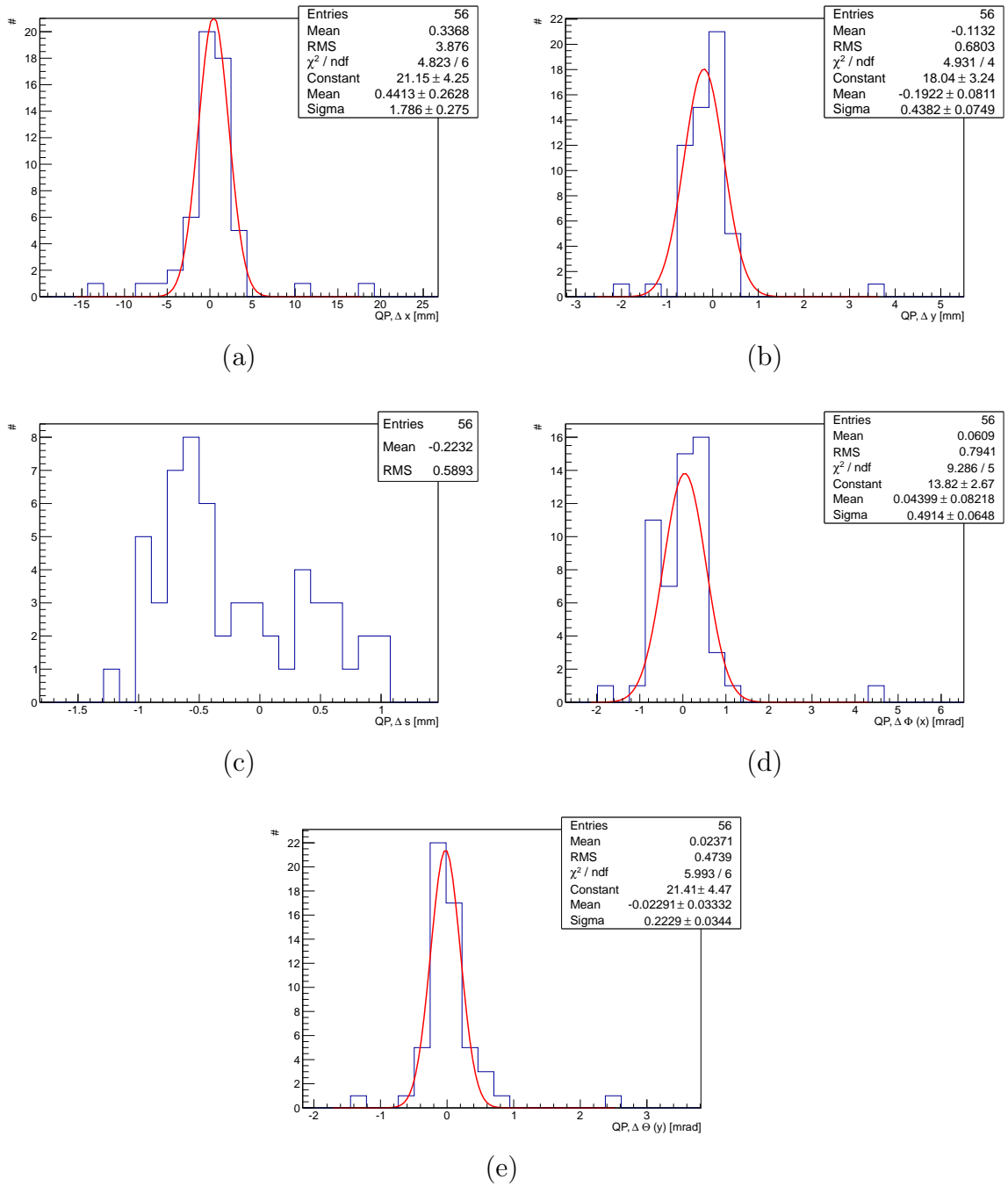
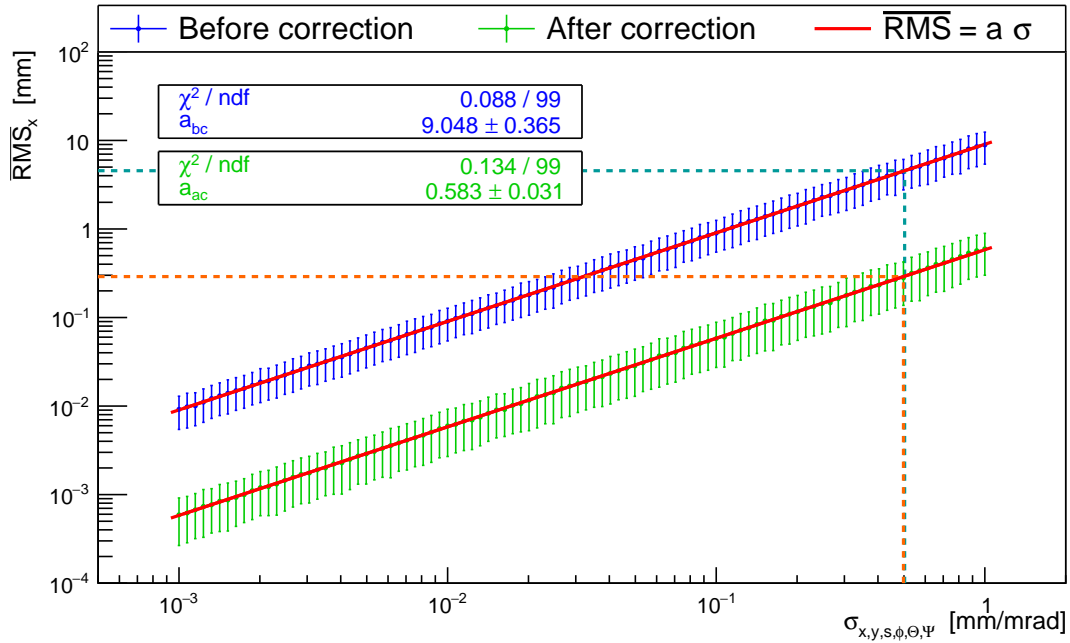
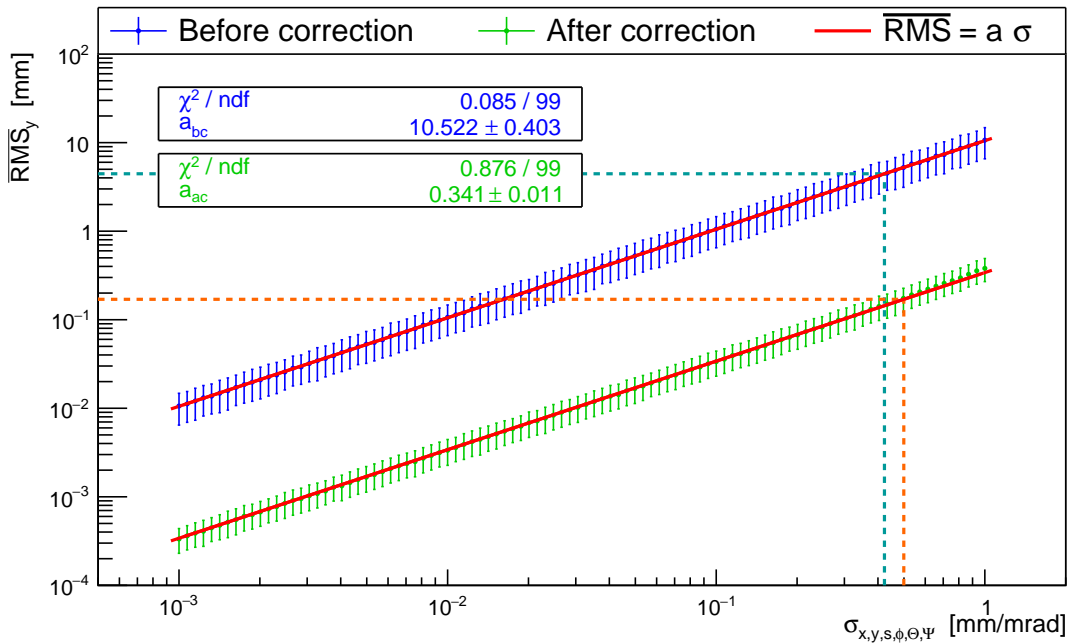


Figure 5.28: Distribution of quadrupole misalignments. In Figure (a) the horizontal deviations are collected. Figure (b) and (c) show the distributions for the vertical and longitudinal direction and (d) and (e) display the rotation angles around the x- and s-axis.



(a)



(b)

Figure 5.29: The plot shows the simulation results using Gaussian distributed magnet misalignments and different standard deviations. The results in x-direction are given in (a), those for y-direction are shown in (b). The dashed lines represent the  $RMS$  that results from simulations using the measured misalignments at COSY.

## 6 Upgrade of the Orbit Correction Setup at COSY

From Section 5 it is known, that the orbit correction efficiency is limited by the setting of the BPMs and corrector magnets in COSY. To achieve smaller values for the closed orbit *RMS* it is thus necessary to improve the orbit correction setup by positioning additional BPMs and magnets in the ring. Additional correcting dipole fields can be created by adding back-leg windings (BLWs) to the quadrupoles. Additional BPMs should be placed in the vicinity of these correctors to ensure that the correction happens at almost the same positions from where the orbit information is taken. In the following simulations the additional BPMs are positioned on top of existing quadrupoles. The challenge is to find out at which quadrupole new back-leg windings and BPMs have to be installed to achieve the largest reduction in the closed orbit *RMS*. Since displacement and rotation of dipoles and quadrupoles are the main sources of closed orbit distortion, these misalignments are considered in the following simulations.

The optimal placement of additional BPMs and correctors needs to be determined by simulating all possible combinations for a fixed number of additional elements. For the case of 56 quadrupoles this would result in

$$\sum_{k=1}^{N=56} \binom{N}{k} = 7.2 \cdot 10^{16} \quad (6.1)$$

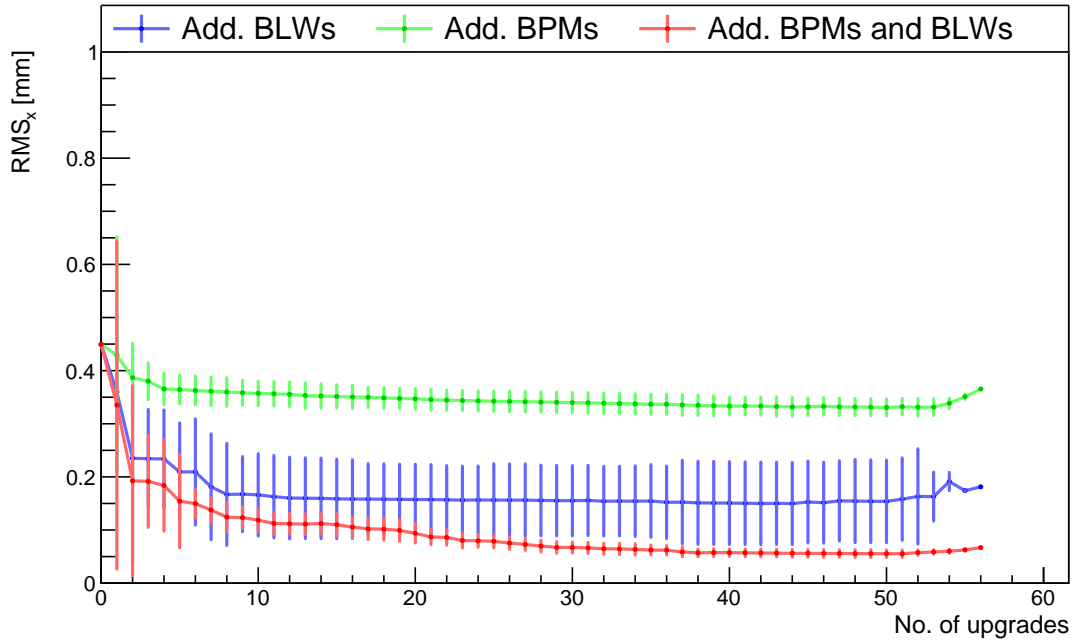
simulation runs. The corresponding computational demand exceeds the given technical possibilities. Assuming one simulation run to take 1 ms, the total duration of all runs would be approximately 2.3 million years. Thus, a heuristical ansatz is used to solve the combinatoric problem. The method starts by upgrading only one quadrupole. To find the optimal setting for this upgrade one quadrupole at a time is upgraded with the additional elements and the closed orbit *RMS* in x- and y-direction with respect to all elements after the orbit correction is simulated. As magnet misalignments the measured misalignments of the survey at COSY are included in the model. Since the goal of this heuristic is to find a setting of additional elements which reduces the *RMS* of the closed orbit in horizontal as well as in vertical direction, both directions cannot be analyzed independently. Thus, the quadratic sum of the *RMS* values in both directions is taken as an indicator for the positioning of the upgrade. To get the global indicator all 56 quadratic sums are compared to each other. The smallest value then determines the quadrupole which is upgraded with additional elements. The errors on the resulting *RMS* values in each direction are estimated by taking the difference of the largest and the smallest value out of the 56 possibilities. The method continues with the upgrade of a second quadrupole. Since one quadrupole is now already occupied there are 55 possibilities left to position the second upgrade. Again, the quadratic sums of the *RMS* values are compared to each other and the smallest value indicates on which quadrupole the second upgrade should be installed. This process is repeated until the number of upgrades is equal to the number of quadrupoles and thus every quadrupole is occupied by additional elements. As a result the heuristic gives the positioning of

quadrupole upgrades and the resulting *RMS* values as a function of the number of upgrades.

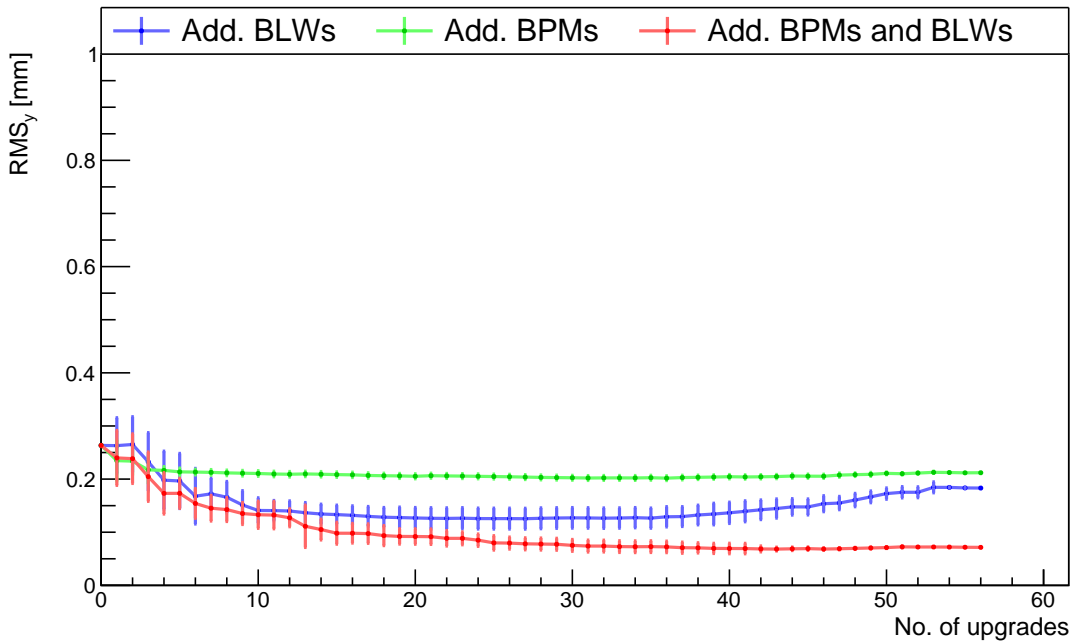
To investigate the influence of additional BPMs and back-leg windings separately the algorithm is applied using quadrupole upgrades only consisting of two BPMs (one for each direction) or two back-leg windings. Afterwards the combined effect is studied where an upgrade includes all four elements simultaneously. Figure 6.1 shows the resulting closed orbit *RMS* behavior. The x-axis denotes the number of upgraded quadrupoles, the y-axis displays the closed orbit *RMS*. The behavior in horizontal and vertical direction is quite similar.

Only adding new BPMs decreases the closed orbit *RMS* in x- (y-) direction by a factor of 1.28 (1.18) when using approximately 50 upgrades. This is a rather small effect compared to the effort that is needed. Installing more than 50 additional BPM pairs on the quadrupoles even leads to an increase in the closed orbit *RMS* in x-direction and thus decreases the orbit correction quality. A possible explanation of this behavior is the ratio of corrector magnets to BPMs. With many BPMs the orbit can be determined more precisely than before and local bumps or large deviations are measurable now. Holding the number of corrector magnets fixed, the orbit correction uses more detailed information but cannot correct all the artificial effects that are measured. The corrected orbit *RMS* thus gets worse. Considering the reverse case with a fixed number of BPMs and increasing number of back-leg windings the resulting *RMS* behavior is much more efficient. This is plausible since now the orbit correction uses more corrector magnets for the same measurement information. With the first ten quadrupole upgrades the closed orbit *RMS* in x- (y-) direction already decreases by a factor of about 2.7 (1.7) and decreases further when using more upgrades. Only for a very large number of upgrades the closed orbit *RMS* increases again. At this point there are much more corrector magnets than BPMs. Trying to find an optimal setting of all corrector magnet strengths can lead to local orbit bumps which increase the total *RMS* although the orbit is nicely corrected at most parts in the ring. Adding BPMs and back-leg windings simultaneously leads to a similar behavior as using only additional back-leg windings but decreases the resulting *RMS* values even further. Installing upgrades at every quadrupole, one ends up with a *RMS* reduction of a factor of about 6.4 in x-direction and 3.7 in y-direction compared to the incident values with no upgrades at all. In both directions this corresponds to an *RMS* value of about  $70\ \mu\text{m}$  after upgrading every quadrupole with additional BPMs and back-leg-windings. A table with the order in which the quadrupoles were upgraded is given in Appendix A. Since the errors in Figure 6.1 are significantly underestimate the true errors not only the order of quadrupole upgrades but also the magnitude of *RMS* change have to be treated with caution.

The results give a first estimate for orders of magnitude and reveal basic effects. For a more detailed and realistic investigation, an improved longterm heuristic is needed which includes more complex algorithm for the determination of the closed orbit *RMS* reduction in both transverse directions.



(a)



(b)

Figure 6.1: Horizontal (a) and vertical (b)  $RMS$  behavior for additional BPMs and back-leg windings installed at COSY. These upgrades are positioned onto existing quadrupoles. The x-axis indicates the number of occupied quadrupoles, the y-axis shows the corresponding  $RMS$  value.

## 7 Conclusion and Outlook

Planned high precision experiments at the Cooler Synchrotron COSY aim at directly measuring the Electric Dipole Moment (EDM) of deuterons for the first time. In this thesis several closed orbit influencing effects were investigated. Displacements and rotations of dipoles and quadrupoles were identified as the main influences which cause a closed orbit *RMS* of approximately 10 mm for a randomized Gaussian distributed standard deviation of 1 mm. Applying an orbit correction algorithm reduces the *RMS* by one order of magnitude. Taking BPM resolution constraints into account sets limits to the orbit correction efficiency and thus inhibits a closed orbit *RMS* below the resolution limit. Further investigated effects like displacements of BPMs and field oscillations due to residual power supply stability are dominated by these effects. Under the assumption of Gaussian distributed magnet misalignments a comparison of the simulated uncorrected orbit with the measurements at COSY was performed. This comparison results in a first estimate of the magnet misalignments with a standard deviation between 0.19 mm and 0.58 mm. Comparing the corrected orbits leads to the conclusion that there is a discrepancy between the internal orbit correction of MAD-X and the correction setup at COSY since the simulated corrected closed orbit *RMS* values lie far below the measured orbit *RMS*.

The measurement results of a survey at COSY were taken as input misalignments in the simulation model of COSY. The previous simulations assuming Gaussian distributed magnet misalignments are compatible with the simulation results using the measured misalignments. The *RMS* value of the simulated uncorrected closed orbit according to the survey data reproduced the measured closed orbit *RMS* at COSY. Magnet misalignments are thus the dominant closed orbit influencing effect.

In order to upgrade the current orbit correction setup additional BPMs and correction dipoles were simulated on top of existing quadrupoles using a heuristical algorithm giving a first estimate of a possible *RMS* reduction and the order in which the quadrupoles should be upgraded. As a result of this simplistic method the closed orbit *RMS* after orbit correction can be decreased by a factor of 6.4 (3.7) in horizontal (vertical) direction which corresponds to a closed orbit *RMS* of about 70  $\mu\text{m}$ .

A more detailed investigation of the upgrade of the current correction system requires more computational power and an improved heuristic.

In summary, this thesis showed that an orbit correction system on its own can hardly ensure a transverse closed orbit *RMS* below 100  $\mu\text{m}$  as it is required for the precursor experiments at COSY. The main challenge is to provide a ring with well positioned magnets and thus to reduce the significant effect of misalignments on the orbit. For a high precision experiment at COSY, the magnets have to be positioned as accurate as possible to their target position. Furthermore, additional correction dipoles can improve the efficiency of the orbit correction and a beam based alignment would give information about the BPM positions relative to the nearby quadrupoles.

## A Upgrade of the orbit correction system

Order of quadrupole upgrades			
Total no. of upgrades	QP for next upgrade		
	Add. BPMs	Add. BLWs	Add. BPMs + BLWs
1	QT8	QT26	QT5
2	QT9	QT5	QT27
3	QU18	QU24	QU7
4	QT7	QU7	QU19
5	QU9	QT29	QT10
6	QT14	QU19	QU15
7	QU4	QT11	QT6
8	QT1	QT6	QT29
9	QU20	QT16	QT1
10	QU12	QU15	QT20
11	QT27	QT18	QT26
12	QU16	QU12	QU24
13	QU17	QU11	QU22
14	QT12	QU3	QU1
15	QU23	QU6	QU3
16	QT10	QT7	QT2
17	QT20	QT1	QU12
18	QT17	QU20	QU11
19	QT13	QT24	QT7
20	QT26	QU21	QT12
21	QU19	QU4	QT8
22	QT11	QU10	QU4
23	QU1	QT20	QU2
24	QT24	QT8	QU16
25	QT18	QT21	QU18
26	QT15	QT32	QU14
27	QT28	QT13	QT4
28	QT30	QT19	QT21

Order of quadrupole upgrades			
Total no. of upgrades	QP for next upgrade		
	Add. BPMs	Add. BLWs	Add. BPMs + BLWs
29	QT23	QT31	QT25
30	QT21	QT22	QU13
31	QT22	QT25	QT24
32	QU8	QT27	QT3
33	QT29	QT14	QU23
34	QT16	QT15	QU20
35	QT32	QU1	QT18
36	QU2	QU2	QT13
37	QU3	QT23	QT15
38	QU21	QU14	QU21
39	QT2	QT30	QT17
40	QT31	QT17	QT32
41	QU11	QU22	QU10
42	QU22	QU9	QU8
43	QU24	QU16	QU9
44	QT3	QU5	QT19
45	QT19	QT28	QU6
46	QU13	QU18	QU5
47	QU7	QT9	QT23
48	QU5	QU23	QT22
49	QU10	QU8	QT31
50	QU6	QU13	QU17
51	QU14	QT10	QT30
52	QU15	QT4	QT11
53	QT4	QU17	QT14
54	QT25	QT12	QT16
55	QT6	QT3	QT9
56	QT5	QT2	QT28

Table 14: Order of quadrupoles to be occupied by additional BPMs and/or back-leg windings.

## List of Figures

3.1	Overview over the accelerator facility at Jülich . . . . .	4
3.2	Positioning of dipoles, quadrupoles and sextupoles at COSY . . . . .	6
3.3	Position of beam position monitors and corrector magnets at COSY . . . . .	7
4.1	Sketch of a dipole . . . . .	10
4.2	Sketch of a quadrupole . . . . .	12
4.3	Closed integration path through quadrupole . . . . .	13
4.4	Sketch of a sextupole . . . . .	14
4.5	Induced image current in beam pipe . . . . .	15
4.6	Velocity dependent field lines of a charged particle . . . . .	16
4.7	Sketch of a shoebox beam position monitor . . . . .	16
4.8	Functionality of a shoebox beam position monitor . . . . .	17
4.9	Co-moving coordinate system . . . . .	19
4.10	Transverse motion of particles with envelope . . . . .	22
4.11	Chromaticity effect and correction using sextupoles . . . . .	24
5.1	Optical functions of the MAD-X model . . . . .	29
5.2	Example of typical transverse closed orbits at COSY . . . . .	30
5.3	Maximum corrector strength . . . . .	31
5.4	Influence of horizontal and vertical <i>RMS</i> due to quadrupole displacements. . . . .	32
5.5	Comparison of measurable and true <i>RMS</i> values. . . . .	34
5.6	Influence of horizontal and vertical <i>RMS</i> due to quadrupole rotations. . . . .	36
5.7	Effect of shifting and rotating a quadrupole . . . . .	37
5.8	Influence of horizontal and vertical <i>RMS</i> due to dipole displacements. . . . .	38
5.9	Sketch of a rotated dipole around the longitudinal axis . . . . .	40
5.10	Influence of horizontal and vertical <i>RMS</i> due to dipole rotations. . . . .	42
5.11	True and measured influence of horizontal <i>RMS</i> due to BPM displacements. . . . .	45
5.12	True and measured influence of vertical <i>RMS</i> due to BPM displacements. . . . .	46
5.13	Comparison of the BPM displacement effect for perfectly positioned and displaced BPMs . . . . .	47
5.14	Influence of horizontal and vertical <i>RMS</i> due to constant BPM resolution of 0.1 mm. . . . .	49
5.15	Influence of horizontal <i>RMS</i> due to a running BPM resolution . . . . .	52
5.16	Influence of vertical <i>RMS</i> due to a running BPM resolution . . . . .	53
5.17	Example of histogram with BPM readings of all random samples at one BPM. . . . .	55
5.18	Influence of horizontal and vertical <i>RMS</i> due to dipole field instabilities. . . . .	56
5.19	Influence of horizontal and vertical <i>RMS</i> due to quadrupole field instabilities. . . . .	58
5.20	Sketch of sinusoidal power supply oscillation . . . . .	59
5.21	Influence of power supply oscillations of sextupoles on the closed orbit <i>RMS</i> . . . . .	61
5.22	Comparison of simulated with measured closed orbit in horizontal and vertical direction . . . . .	63
5.23	Reference mark positioning on dipoles and quadrupoles. . . . .	64

---

5.24	Best-fit-plane of the survey performed at COSY. . . . .	66
5.25	Survey: Determination of magnet misalignments . . . . .	67
5.26	Survey: closed orbit before and after orbit correction. . . . .	69
5.27	Survey: Distribution of dipole misalignments . . . . .	70
5.28	Survey: Distribution of quadrupoles misalignments . . . . .	71
5.29	Survey: comparison of Gaussian distributed misalignments and survey data results . . . . .	72
6.1	Results in horizontal and vertical direction of the upgrade of the correction setup with additional BPMs and BLWs. . . . .	75

---

## List of Tables

1	Quadrupole displacement, fit parameters . . . . .	33
2	Quadrupole rotation, fit parameters . . . . .	35
3	Dipole displacement, fit parameters . . . . .	39
4	Dipole rotation, fit parameters . . . . .	41
5	BPM displacement, fit parameters . . . . .	44
6	BPM with running resolution, fit parameters . . . . .	50
7	Dipole and quadrupole misalignments, fit parameters . . . . .	50
8	Field instabilities, fit parameters . . . . .	57
9	Relative error and maximum current of COSY magnets. . . . .	59
10	Influence of residual power supply oscillations of the COSY magnets in the closed orbit <i>RMS</i> . . . . .	60
11	Vertical deviation of COSY magnets from the best-fit-plane. . . . .	65
12	RMS values from survey data simulation . . . . .	67
13	Survey: distribution spread of magnet misalignments. . . . .	68
14	Order of quadrupoles to be occupied by additional BPMs and/or back-leg windings. . . . .	ii

---

## References

- [1] Wolski A. *Beam Dynamics In High Energy Particle Accelerators*. Imperial College Press, 1 edition, 2014.
- [2] Rosenthal M. *Experimental Benchmarking of Spin Tracking Algorithms for Electric Dipole Moment Searches at the Cooler Synchrotron COSY*. PhD thesis, RWTH Aachen University, 2016.
- [3] CERN. MAD-X Introduction. URL: <http://mad.web.cern.ch/mad/>, Sep. 2016.
- [4] Griffiths D. *Introduction to Elementary Particles*. WILEY-VCH, 2 edition, 2008.
- [5] Bennett et al C.L. First year Wilkinson Microwave Anisotropy Probe (WMAP) observations: Preliminary maps and basic results. *Astrophysical Journal*, 148(1), 2003.
- [6] Sakharov A. D. Violation of CP Invariance, C Asymmetry, and Baryon Asymmetry of the Universe. *Soviet Journal of Experimental and Theoretical Physics Letters*, 34(5), 1967.
- [7] Fukuyama T. Searching for New Physics beyond the Standard Model in Electric Dipole Moment. *International Journal of Modern Physics*, 27(16), 2012.
- [8] Pretz J. Measurement of Permanent Electric Dipole Moments of Charged Hadrons in Storage Rings. *Hyperfine Interactions*, 214(1-3), 2013.
- [9] C.A. Baker, D. D. Doyle, and P. Geltenbort. An Improved Experimental Limit on the Electric Dipole Moment of the Neutron. *Physical Review Letters*, 97(13), 2006.
- [10] Berger C. *Elementarteilchenphysik*. Springer, 2 edition, 2006.
- [11] Griffith W. C., Swallows M. D., and Loftus et al. T. H. Improved limit on the permanent electric dipole moment of  $^{199}\text{Hg}$ . *Physical Review Letters*, 102(10), 2009.
- [12] Lehrach A. Project Overview and Computational Needs to Measure Electric Dipole Moments at Storage Rings. In *Proceedings*. International Computational Accelerator Physics Conference, Rostock, 2012.
- [13] Lehrach A. *Strahl- und Spindynamik von Hadronenstrahlen in Mittelenergie-Ringbeschleunigern*. Forschungszentrum Jülich GmbH, 2008.
- [14] Alinovskiy N., Bedareva T., and Bekhtenev E. 2 MeV Electron Cooler for COSY and HESR - First Results. In *Proceedings*. 5th International Particle Accelerator Conference, Dresden, Germany, 2014.
- [15] Prasuhn D., Bechstedt U., and Dietrich J. Status of the Cooler Synchrotron COSY Jülich. In *Proceedings*. Particle Accelerator Conference, Chicago, 2001.

- [16] Stockhorst H., Bechstedt U., and Dietrich J. The Cooler Synchrotron COSY Facility. In *Proceedings. Particle Accelerator Conference*, Vancouver, 1997.
- [17] Wiedemann H. *Particle Accelerator Physics*. Springer, 3 edition, 2007.
- [18] Wille K. *Physik der Teilchenbeschleuniger und Synchrotronstrahlungsquellen*. Springer Fachmedien, 2 edition, 1996.
- [19] Conte M. *An Introduction To The Physics Of Particle Accelerators*. World Scientific, 2 edition, 2008.
- [20] Forck P., Kowina P., and Liakin D. CERN Accelerator School Beam Diagnostics, Chapter: Beam position monitors. In Brandt D., editor, *Proceedings*. Cern European Organization for Nuclear Research, 2009.
- [21] Hinterberger F. *Physik der Teilchenbeschleuniger und Ionenoptik*. Springer, 2 edition, 2008.
- [22] Zimmermann F. Measurement and Correction of Accelerator Optics. *Joint US-CERN-Japan-Russia Particle Accelerator School on Beam Measurement*, 1998.
- [23] Chung Y., Decker G., and Evans K. Closed Orbit Correction Using Singular Value Decomposition of the Response Matrix. In *Proceedings*. 15th IEEE Particle Accelerator Conference, 1993.
- [24] Zimoch D. *Implementierung eines Orbitkorrektursystems an der Synchrotronstrahlungsquelle DELTA*. PhD thesis, University Dortmund, 2002.
- [25] Retzlaff M. Private communication, Apr. 2016.
- [26] Vermessungsbüro Dipl.-Ing. H.J.Stollenwerk. Bahnstr. 8, 50126 Bergheim, Nordrhein-Westfalen.
- [27] Vermessungsbüro Dipl.-Ing. H.J.Stollenwerk. Private presentation, Aug. 2016.

## Acknowledgments

At this point I would like to thank everyone who supported me in the last year. Special thanks go to my supervisor Prof. Dr. Andreas Lehrach for the possibility to write this thesis at the Forschungszentrum Jülich and for the support in technical issues he was always willing to offer. I also would like to thank Prof. Dr. Anke Schmeink who agreed to co-supervise this thesis.

Furthermore I am grateful for all the fruitful conversations and the input I got from the members of the JEDI collaboration. The contributions in several meetings and the feedback to my results gave me a deeper inside in the whole topic of accelerator and spin physics. Especially I like to mention Dennis Eversmann, Nils Hempelmann, Jan Hetzel, Fabian Hinder, Marcel Rosenthal, Fabian Trinkel and Christian Weidemann who shared their experiences in scientific working and organizational issues with me.

Furthermore I would like to thank Frederic Poncza for supporting me during the whole time of my thesis and cheering me up after long days.

My final thanks go to my family for always believing in me and all the good advices they give to me.



# Eidesstattliche Versicherung

---

Name, Vorname

---

Matrikelnummer

Ich versichere hiermit an Eides Statt, dass ich die vorliegende Masterarbeit mit dem Titel

**Analyse von Abweichungen der geschlossenen Teilchenbahn für eine erste direkte Messung des Elektrischen Dipolmoments von Deuteronen im Kühlersynchrotron COSY**

selbständig und ohne zulässige fremde Hilfe erbracht habe. Ich habe keine anderen als die angegebenen Quellen und Hilfsmittel benutzt. Für den Fall, dass die Arbeit zusätzlich auf einem Datenträger eingereicht wird, erkläre ich, dass die schriftliche und die elektronische Form vollständig übereinstimmen. Die Arbeit hat in gleicher oder ähnlicher Form noch keiner Prüfungsbehörde vorgelegen.

---

Ort, Datum

---

Unterschrift